A nanoscale study of dissolution and growth processes in cement hydrates

by
Vanessa Rheinheimer

Supervised by Ignasi Casanova Hormaechea

Submitted to the School of Civil Engineering of Barcelona
in partial fulfillment of the requirements for the degree of
Doctor
by the Universitat Politècnica de Catalunya.

Barcelona, July 2012

If at first an idea does not sound impossible, then there is no hope for it.

Albert Einstein

To my dad and my sisters,

the reason of my life.

Acknowledgements

I would like to thank my thesis director Ignasi Casanova for giving me the opportunity to pursue this doctorate, for the advice and support throughout the duration of this thesis.

I am grateful to Prof. Paulo Monteiro for stimulating discussions and guidance as well as for the opportunity of developing part of this thesis with his group at University of California.

I thank the Department of Civil Engineering and the Institute of Energy Technologies for the technical and financial support for the tasks of this thesis.

I want to thank the Technical University of Catalonia for the financial support through the CUR of the DIUE of the Generalitat de Catalunya, and also the Spanish Ministry of Science and Innovation for partially founding by grant CTQ2009-12520.

I am deeply grateful for all the technical support of the scientists who helped me in the laboratories at CRnE and ALS: Trifon Trifonov, David Kilcoyne, Tolek Tyliszczak, and especially to Montserrat Domínguez for all the attention, support and

friendship. I also thank the technical support from Jose Calvo, Josep Bassas, Xavier Sisquella and Savador Galí.

I wish to thank the colleagues at UC, for so kindly spend time helping and teaching me during my time there, and sharing the night shifts at the laboratory: Daniel, Sung, Rosie and Pierre. I also thank all the colleagues from the materials group.

I thank the Nanocem network for believing and supporting this project as well as for the scientific discussions, mainly to Prof. Leon Black and Andre Nonat.

I want to thank the people who patiently helped me with the final corrections of this thesis.

I am lucky enough to, whenever I go, be surrounded by amazing and good people. For this reason I have several friends to thank here who made these years special. The people from my office, more than colleagues, good friends: Nuria, Monika, Edu, Elena, Cristian, Raul, Albert, Leonor, David, Claudia, and the ones from before: Estel, Andrea, Elaine, Diego, Sergio, people who made pleasant every day of work, and every time out of work: you are wonderful! My Catalonian family Aninha and Maiquel, with whom I had always found the taste of home; My amazing Grêmio family: Joice, Marta, Jean, Pati, Paulo, Manu, Andre, Gi, Jo, Re, Cha, Dani (s), Izaias, Beto, Tassia, Mauri, Pedro, Diego (that was the time of my life); My roomie, friend and counselor Izelman for all the special moments we shared; my Californian family: Carlos, Victor, Breda (I miss you so much!); My friends from home whom I feel close even being far away: Van, Pri, Camila, Gisa: you are lovely people.

I thank my friend and mentor Ana Paula, for opening me doors in all aspects of my life, for being always my guard angel and being my third sister.

I am especially grateful to my family: my father and my sisters, for all the unconditional love, support, trust and comprehension that made me strong to go through all this. You are the reason for everything. You are my life, my strength, and my light. I love you more than anything.

Abstract

This thesis aims at providing new knowledge on the, otherwise poorly known, molecular-scale mechanisms that operate during hydration of cement phases and dissolution of their hydrates. In order to pursue this objective, a novel approach has been followed, including the development of a new procedure to synthesize thin films of calcium silicates, real time characterization of grain growth and dissolution with liquid-cell atomic force microscopy, and monitoring of their chemical evolution by X-ray photoelectron spectroscopy of thin films hydrated in-situ, avoiding atmospheric contamination.

Nanometer-sized films of clinker phases have been prepared using electron-beam evaporation methods. After deposition on silicon substrates, film thicknesses and mineralogical composition were characterized by atomic force microscopy (AFM) or mechanical profilometry and grazing-angle X-ray diffraction (GAXRD), respectively. Chemical composition was determined by X-ray photoelectron spectroscopy (XPS). Results from the GAXRD and XPS analysis show that aluminates phases are not suitable to be evaporated by electron beam technique. However

quantitative analysis of calcium silicates samples shows that the Ca:Si ratio of the deposited film is the same as in the bulk starting material, confirming the suitability of the technique for the synthesis of these materials.

Calcium silicate thin films with different thicknesses were submitted to hydration in different ways. XPS results describe clear chemical changes when samples are exposed to water vapor by shifts on the silicon peak, broadening on the calcium peak and decreasing on the Ca:Si ratio, related to the silicon polymerization due to the C-S-H formation. In situ hydration in fluid cell followed by AFM in water and calcium hydroxide saturated solution allows observing the formation of C-S-H particles, that happens very fast in C_3S, which is dissolved later, and slower in C_2S. Finally, Scanning transmission X-ray microscopy (STXM) of samples hydrated in situ with water allows observing the formation of particles with different concentration of calcium and silicon, and different chemical state at some point.

The development of this technique of synthesis and the results obtained on the hydration allow improving the knowledge of early stage clinker phase hydration at the molecular level and to better understand the behavior of these materials, shedding some additional light on the complex problem of the hydration mechanisms of cementitious materials.

Keywords: Clinker phases; thin films; hydration; cement; XPS; AFM; GARXD; STXM.

Resum

Aquesta tesi té per objectiu proporcionar nous coneixements sobre els mecanismes, abans poc coneguts, que operen durant la hidratació de les fases de ciment i la dissolució dels seus hidrats a escala molecular. Per tal d'aconseguir aquest objectiu, un nou enfocament ha estat seguit amb l'elaboració d'un nou procediment per sintetitzar pel·lícules primes de silicats de calci, la seva caracterització en temps real del creixement del gra i de la dissolució amb les cel·les de líquid al microscopi de forces atòmiques i el seguiment de l'evolució de la seva composició química per espectroscòpia de fotoelectrons de raigs X de pel·lícules primes hidratades in-situ, evitant la seva contaminació atmosfèrica.

S'han preparat pel·lícules nanomètriques de les fases del clínquer utilitzant l'evaporació per feix d'electrons. Després de la deposició en substrats de silici, es van caracteritzar el gruix mitjançant la microscòpia de forces atòmiques (AFM) i la perfilometria mecànica i la composició mineralògica amb la difracció de raigs X d'angle rasant (GAXRD). La composició química es va determinar per espectroscòpia fotoelectrònica de raigs X (XPS). Els resultats del GAXRD i d'XPS mostren que els

aluminats no són adequats per a ser evaporats utilitzant l'evaporació assistida amb feix d'electrons. No obstant això, anàlisis quantitatives de les mostres de silicats de calci mostren que la relació Ca:Si de la pel·lícula dipositada és la mateixa que en el material de partida, el que confirma la idoneïtat de la tècnica per a la síntesi d'aquests materials.

Les pel·lícules primes de silicat càlcic de gruixos diferents van ser sotmeses a hidratació de diferents maneres. Els resultats d'XPS descriuen canvis químics clars quan les mostres estan exposades al vapor d'aigua com s'infereix dels canvis en el pic del silici, l'eixamplament del pic del calci i la disminució en la relació Ca:Si, que es relaciona amb la polimerització del silici degut ala formació de C-S-H. La hidratació in situ en aigua o solució saturada d'hidròxid de calci a la cel·la de fluid de l'AFM permet observar la formació de partícules de C-S-H. La hidratació ocorre molt ràpidament en el C_3S, que després es dissol, i és més lenta en el C_2S. Finalment, la microscòpia de transmissió i escaneig de raigs X (STXM) de les mostres hidratades in situ amb aigua permet observar la formació de partícules amb diferents concentracions de calci i silici i, en alguns casos, la variació de l'estat químic .

El desenvolupament d'aquesta tècnica de síntesi i els resultats obtinguts en la hidratació permeten millorar el coneixement de la hidratació de les fases del clínquer en estadis inicials a nivell molecular i entendre millor el comportament d'aquests materials, ajudant a aclarir el complex problema dels mecanismes d'hidratació dels materials del ciment..

Paraules clau: fases del clínquer, pel·lícules primes; hidratació, ciment, XPS, AFM; GARXD; STXM.

Contents

List of Figures

List of Tables

Nomenclature

C: Free lime - CaO

S: Silica - SiO_2

A: Alumina - Al_2O_3

F: Iron oxide III - Fe_2O_3

H: Water - H_2O

$\bar{C}$: Calcium carbonate - $CaCO_3$

N: Sodium oxide - Na_2O

K: Potassium oxide - K_2O

M: Magnesium oxide - MgO

C_3S: Tricalcium silicate - $3CaO.SiO_2$

C_2S: Diclacium silicate - Belite - $2CaO.SiO_2$

C_3A: Tricalcium aluminate - $3CaO.Al_2O_3$

C_4AF: Ferrite - Solid solution of $2CaO.Fe_2O_3$ and $2CaO.Al_2O_3$ - $4CaO.Al_2O_3.Fe_2O_3$

CH: Calcium Hydroxide - $Ca(OH)_2$

C-S-H: Calcium silicate hydrate gel - $CaO.SiO_2.H_2O$

XPS: X-ray photoelectron spectroscopy

STXM: Scanning transmission X-ray microscopy

AFM: Atomic force microscopy

LCAFM: Liquid cell atomic force microscopy

XRD: X-ray diffraction

GAXRD: Grazing angle X-ray diffraction

FIB: Focused ion beam

SEM: Scanning electron microscopy

XRF: X-ray fluorescence

NEXAFS: Near edge X-ray absorption fine structure

NMR: Nuclear magnetic resonance

1 Introduction

The construction industry is constantly growing and demanding more materials to support its progress. Portland cement is the most widely used type of cement, and it is composed of 95% clinker. Its production is highly energy consuming and greenhouse gases emitting. For these reasons there are great efforts to decrease these two factors in order to minimize the environmental impact of the cement manufacturing.

Furthermore the world's population is forecasted to achieve the astonishing number of 9 billion people by 2050. This means a huge need for infrastructure and urbanization and with this comes an enormous demand for cement: a consumption of 3859 million tonnes worldwide is expected for 2012, the highest in history and it is continuously increasing. Only China has almost doubled its consumption from 2004 to 2010, reaching an amount of 1851 million tonnes. The second-largest consumer is India, with 212 million tonnes in 2010, while the third, the United States, consumed 69 million tonnes, according to the 9th International Cement Review's Global Cement

Report. So far, the consumption in Europe is decreasing over the last years regarding the slump: from 260 in 2007 to 190 million tonnes in 2010. Worldwide the cement and concrete industry provide jobs to 1% of the population.

On the other hand, the international agreements for the greenhouse gas emission reductions put a lot of pressure on the industry by demanding the reduction of CO_2 emissions by 80% by 2050, while the production is expected to double. The cement manufacture produces approximately 2.4% of the global CO_2 emissions from industrial and energy sources. This means that the manufacturing process and material characteristics have to change significantly in the near future. As a consequence, performance will also be modified.

Even though concrete is the material chosen for constructing almost all types of structures, the industry and society assume that there is no need for minimum maintenance. Nevertheless the demand for repair and rehabilitation of concrete structures increases constantly due to this deficiency of maintenance.

Over the last years, improvements in concrete technology have been achieved, increasing the performance of structures. But these advances are based, in their majority, in trial-and-error tests more than in fundamental research. For this reason there had been a lack on the development of new and more efficient materials in the cement industry based on the bedrocks of cement technology.

However actually there are many efforts to improve and develop new technologies for the cement and chemical industries that can provide materials that are more durable, stronger, more cost efficient and with less environmental impact. With so much interest from industry and government in improving this material, the need of fundamental research is greater than ever in this field.

To facilitate this improvement it is necessary to understand the behavior of cementitious materials at nanometric and atomic level in order to be able to predictably change properties that affect the service life of concrete structures. That is, studying the material in a multiscale approach: going from the atomic level, understanding the cement hydration, the chemical formation of the products, the micro pores structure and the transport in the structure, to the mechanical behavior of the paste and the concrete and finally reaching the macro structure of reinforced concrete, as outlined in Figure 1.

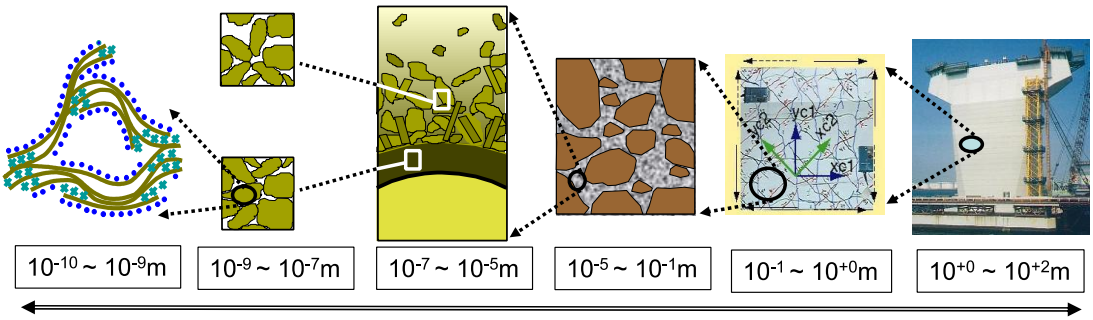

Figure 1 Multi scale approach for the cementitious materials[1].

Calcium silicates are the most important components in Portland cement as their reaction leads to calcium silicate hydrate (C-S-H). This product is the responsible for the strength of the cement paste. Much research is focused on this area, but the details of the formation of this component still remain elusive.

Nanoscale experiments in cementitious materials normally require special sample preparation that can damage the material or change its properties, or it can be impossible to run analysis due to certain morphological characteristics of the material. For example many techniques provide relevant information but require extremely thin samples in order to be transparent (e.g. transmission electron microscopy, soft X-ray microscopy, scanning transmission X-ray microscopy, etc.), while others require flat samples (e.g. atomic force microscopy, nanoindentation...).

This thesis proposes a new tool for the production of suitable samples for nanoscale studies of cementitious materials, hydration mechanisms, nanomechanical properties and interaction with other materials: thin films of clinker phases. This work aims to improve the knowledge of early stage clinker hydration at the molecular level and to put additional light to better understand the behavior of these materials.

Thin films have been widely used in the semiconductor, aerospace and optics industry, but thus far have not been applied to cementitious materials. The development of thin films of clinker phases opens an extensive range of possibilities for the study of cement properties and its phases at the nanoscale. Clinker hydration is a very complex process, involving several phases and secondary products formed and, subsequently, properties of concrete are governed by process at the molecular

[1] From T. Ishida, Multi-scale modeling of concrete performance – toward a lifespan simulation of reinforced concrete structure, 2010.

level with single crystal formation. Thus, the durability and behavior of concrete during its service life strongly depends on its nanostructure.

1.1 Objectives

The objectives of this thesis are:

- To produce thin films of clinker phases as an alternative for sample preparation for nanoscale studies;
- To observe and quantify the hydration of calcium silicates thin films under physico-chemically controlled conditions;
- To expand the understanding of the dissolution and precipitation mechanisms and kinetics of calcium silicates.

1.2 Outline of the thesis

This thesis is based on experimental work, including the characterization of the anhydrous clinker phases, the synthesis of thin films, their characterization and finally, the experiments to monitor the dissolution and hydration of the calcium silicate thin films.

Based on this, this document is structured as follow:

Chapter 2 presents the state of the art on the ordinary Portland cement composition, and hydration. The hydration of pure clinker phases is described with more detail in the calcium silicates, studied later. Special attention is given to the formation of C-S-H, as the main hydration product and the principal binding agent of cement-based materials.

Chapter 3 describes the main techniques used for the characterization of the materials. Furthermore, it presents the attempt of synthesizing thin films of all clinker phases by the use of an electron beam evaporation technique.

In Chapter 4 samples of tricalcium silicate (C_3S) thin films are submitted to dissolution process and the changes are tracked chemically, mineralogically and

morphologically by X-ray photoelectron spectroscopy (XPS), grazing angle X-ray diffraction (GAXRD) and atomic force microscopy (AFM).

Chapter 5 presents a study of the hydration of tricalcium and β-dicalcium silicate (C_2S) thin films. Chemical and morphological changes are followed when samples are hydrated in water vapor, liquid water and a saturated calcium hydroxide solution. XPS, scanning transmission X-ray microscopy (STXM) and AFM are used to characterize the products formed.

Finally Chapter 6 presents the main conclusions of this thesis and perspectives for the future work. More importantly, it evidences the expectations for the application of this approach in the study and development of cementitious materials as well as their interaction with other components.

2 Ordinary Portland cement: composition and hydration

This chapter presents the state of the art on ordinary Portland cement composition and hydration with focus in the calcium silicates, responsible for the main hydration products.

2.1 Composition of ordinary Portland cement

The Portland cement is an inorganic material result of burning and grounding of a raw material containing CaO, SiO_2, Al_2O_3 and small quantities of other materials. Its mixture with water results in a cement paste that sets and hardens due to the reaction, called hydration. The result is a strength material that is stable even under water. However it has to retain workability for enough time to be transported and placed. Additionally, it has to be strong, stable and durable.

The hardening of Portland cement happens mainly due to the hydration of calcium silicates, and secondarily by calcium aluminates.

The Portland cement clinker consists of at least two-thirds by mass of calcium silicates ($3CaO{\cdot}SiO_2$ and $2CaO{\cdot}SiO_2$) and the other one-third by mass of calcium aluminates ($3CaO{\cdot}Al_2O_3$ and $4CaO{\cdot}Al_2O_3{\cdot}Fe_2O_3$), plus some minor components [1].

Commercial Portland cement can often have different additions (pozzolans, fly ashes, silica fume etc) depending on the use it is designed for, and the cement standard classification is based on the amount of each of the compounds it contains.

2.2 Tricalcium Silicate

Tricalcium silicate has the chemical formula Ca_3SiO_5 and is the major phase of Portland cement, controlling the setting and hardening.

It can occur as seven different polymorphs, whose stability depends on the temperature of sintering or the impurities absorbed during the synthesis. There are three triclinic (T), three monoclinic (M) and one rhombohedral (R) forms, which are [2]:

$$T_1 \xleftrightarrow{620°C} T_2 \xleftrightarrow{920°C} T_3 \xleftrightarrow{980°C} M_1 \xleftrightarrow{990°C} M_2 \xleftrightarrow{1060°C} M_3 \xleftrightarrow{1070°C} R$$

The letters indicate the formal crystallographic symmetry and the numbers are variants of a particular symmetry. When cooled at equilibrium to room temperature, the pure compound is T_1.

The impurities are important as they define the type of polymorph and provide stabilization at room temperature. These doping ions can be of several sorts, such as Al^{3+}, Mg^{2+} and Fe^{3+}, K^+, Na^+ and SO_4^{2-}.

The tricalcium silicate found in clinker varies in composition and reactivity and is called Alite. It is an impure form, which contains other ions present in the original raw matrix, appearing normally as M_3 monoclinic form [3], even if triclinic and rhombohedral forms can also be found.

2.3 Dicalcium Silicate

Around 15 to 30% of normal Portland cement clinkers are composed by Belite, a dicalcium silicate with incorporation of some foreign ions. It is present in cement entirely or largely as the β-polymorph, or also α-polymorph. However just the first

form has cementing value under normal hardening conditions. The belite increases the concrete strength at later ages because it reacts more slowly with water than the other clinker phases. By one year, the strength values obtainable from pure alite and pure belite are about the same under comparable conditions [2, 4, 5].

Belite formation is highly influenced by the temperature. Some of the components change drastically with variations of temperature during the burning process of the clinker. It is stable and readily prepared from reactive CaO and SiO_2 when burned at 300°C, but at lower temperatures the γ-belite is formed; this form does not hydrate, and therefore it is avoided in cement manufacture. On the other hand belite can incorporate a larger amount of foreign ions than the alite [2, 4], including Mg^{2+}, Na^{+}, among others.

Four forms are known in belite: α, α´, β, and γ. As mentioned above, only the β form with a monoclinic unit cell exists in clinker [6].

2.4 Tricalcium Aluminate

The C_3A is a tricalcium aluminate ($Ca_3Al_2O_6$) modified by incorporation of foreign ions (Si^{4+}, Fe^{3+}, Na^{+} and K^{+}). The Na^{+} is the most common incorporation on C_3A by substitution of Ca^{2+} and as inclusion of a second ion in an empty space.

C_3A reacts rapidly with water and normally a set-controlling agent (normally gypsum) is added in order to slow down the process [2]. The amount of the calcium aluminate phase in Portland cement clinkers is around 5 to 10%, except in sulfate resistant cements where it is standardized to be less than 5%.

C_3A can form in cubic, orthorhombic or monoclinic symmetry, depending on the amount of ions and the temperature of synthesis. The orthorhombic and monoclinic solid solutions of C_3A can be transformed in tetragonal (or pseudo orthorhombic) polymorphs at temperatures above 450°C. On the other hand the Na-doped (orthorhombic) tricalcium aluminate shows lower reactivity [4]. An extensive research on this topic was developed by Kirchheim [7, 8].

The cubic lattice is the main crystallization form of C_3A in clinker, but the symmetry can change to orthorhombic and monoclinic point groups due to the incorporation of foreign ions (mainly alkalis and SiO_2), that can occur in cements with alkalis [4]. Moreover the cubic and orthorhombic forms of tricalcium aluminate

are less susceptible to sulfate attack [9]. Therefore large amounts of tricalcium aluminate in clinker reduce the resistance of the hardened paste against sulfates and other chemical attack [3, 9].

2.5 Calcium Aluminoferrite

Around 5 to 15% of the Portland cement clinkers are formed by a ferrite phase, which is tetracalcium aluminoferrite ($4CaO \cdot Al_2O_3 \cdot Fe_2O_3$) modified in composition by variation in Al/Fe ratio and incorporation of foreign ions. The reaction with water and the increasing of the strength occur in an average between those of alite and belite at later ages [2]. The ferrite phase is responsible for the gray color of the Portland cement by the presence of iron: without iron its color is white, as in white cement [10]. Its nomenclature is C_4AF and the potential components of this compound are C_2F, C_6AF_2, C_4AF, and C_6A_2F.

2.6 Hydration of pure clinker minerals

Many efforts have been done over the last decades for understanding the hydration of the cement itself and its phases. All these efforts are due to the fact that understanding the fundamentals of hydration mechanisms makes it possible to change properties that will affect the macroscopic behavior and service life of structures, besides reduction in costs and gases emissions.

It is well known that cement reacts with water forming a stiff mass that depends on the thermodynamics and material characteristics by a dissolution-precipitation process. It happens within the passage of the ions through solution mandatorily when the hydration products have a lower solubility than the anhydrous phases, taking into account that in multiphase systems some elements are more soluble than others and for this reason they dissolve preferentially, changing the system kinetics [11].

The changes on the cement microstructure during the first 24 hours as well as its thermodynamic behavior are well documented, but the very early ages are not well understood yet, mainly regarding the dormant period, where a slowdown in the rate of reactions is observed [12].

Important reviews on the mechanisms and modeling of cement hydration have been recently published summarizing the state of the art on the subject and giving significant contributions on the general overview of the topic [13, 14]. However, further research is needed in this area.

Hydration kinetics depends on many factors, such as dissolution and precipitation rates, area of interface between solid and solution, temperature, and concentrations, among others. It varies during the process as these factors change, mainly the initial concentration of the solution [3, 12, 15, 16].

It is, however, reasonable to study the clinker phases individually as the kinetics and reactions are complex when analyzing all the phases of cement simultaneously. At the same time many factors can disturb the process, changing the reactivity of the compounds.

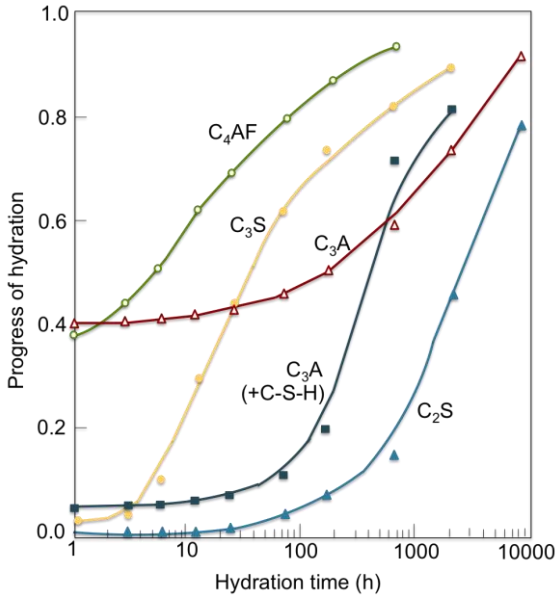

Figure 2 Typical hydration kinetics of pure clinker minerals for a paste hydrated at ambient temperature. C_3A is presented with (dark blue) and without (red) added gypsum [3]. Role of gypsum is discussed in Section 2.4.

Figure 2 represents the typical hydration kinetics of the different clinker phases. Hydration of C_3A and C_4AF occurs very fast, while in C_3S and C_2S reactions it happens slowly. The addition of gypsum slows down the rate of C_3A hydration.

2.6.1 Hydration of clinker silicates

C_3S hydration happens over a dissolution-precipitation process that may occur through the formation of etch pits where the C-S-H preferentially precipitates [12]; even so, its precipitation rate depends on the concentration of the components in solution. After the initial precipitation, new nucleation occurs rather than extensive growing on the already precipitated particles, and many particles tend to agglomerate. In fact, the system reaches the steady state when growth dominates nucleation. The whole process is rather complex and yields to calcium silicate hydrate and calcium hydroxide:

$$3CaO \cdot SiO_2 + (3 + m - n)H_2O \leftrightarrow nCaO \cdot SiO_2 \cdot mH_2O + (3 - n)Ca(OH)_2$$

In this case m is the water to silicate ratio (H_2O/SiO_2) that is around 4 in saturated pastes. The Ca/Si ratio for cement pastes is around 1.2 to 2.1 while in pure C_3S pastes this value is around 1.7 to 1.8; that means that the water/cement ratio necessary to complete the hydration of C_3S is around 0.42 [2].

The hydration of C_2S is very similar to that of C_3S but happens at a lower rate. The products formed are the same. At the beginning the hydration presents a maximum exothermic peak as in C_3S, but has only a weak second peak. The induction period is extended and the hydration rate is very slow. After it finishes the hydration rate starts to increase and reaches a maximum after several days or weeks, followed by a slowing down [3].

$$2(\mathrm{CaO})_2(SiO_2) + 5\mathrm{H_2O} \leftrightarrow (CaO)_3(SiO_2)_2.4(H_2O) + \mathrm{Ca}(OH)_2$$

Previous studies show that the dissolution of C_3S and precipitation of C-S-H start almost immediately after contact with water, in a range of seconds to minutes [12, 17, 18]. Additionally there are descriptions of the formation of an intermediate silicate hydrate phase before its conversion into C-S-H, when there is enough calcium in solution [19, 20].

Hydration of C_3S suffers a slow down when reaching the so-called induction or dormant period, followed by a rapid increasing on the rate (Figure 3). This

behavior follows the geochemical laws for complex iono-covalent minerals, as the C-S-H forms preferentially on a smooth or pitted surface by isolated clumps and it requires extra energy for the formation of the first pit. Thus, C_3S starts dissolving immediately after its contact with water, increasing the concentration of CaO and SiO_2 in solution, decreasing the degree of undersaturation and the rate of dissolution, when the induction period occurs, until it gets enough energy to start precipitating [11]. Remarkably, the precipitation of C-S-H starts at crystal defects [17]. Scrivener & Nonat [11] underline that the nucleation of C-S-H by hydration of pure C_3S with water cannot be followed easily, as it happens very fast due to high supersaturation.

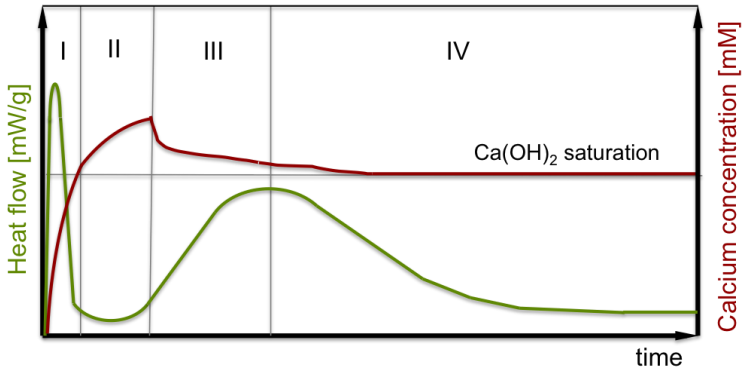

Figure 3 The different periods of the hydration of alite. Modified after [12].

In this context, period *I* is related to the initial dissolution phase. Here the rate of reaction is very high due to the dissolution of the anhydrous phase, and then slows down rapidly running to period *II*. This is known as the induction period. After that, in period *III*, the rate of reaction increases again reaching a maximum with the massive precipitation of the hydrates; during period *IV*, it slows down gradually due to the formation of products and consumption of the reactants.

On the other hand studies show that pure C_3S has different behavior when compared to impure Alite regarding grain growth, density of reactive sites on the surface and density of hydrate products, affecting the hydration kinetics [15]. The consumption of materials depends on the grain size, thus small particles and high surface areas have a major effect on the induction period as it provides more products to dissolve in a shorter period of time.

Precipitation of portlandite ($Ca(OH)_2$) during C_3S hydration plays an important role on the kinetics, as it is more soluble than C-S-H and preferentially forms when the lime concentration is above the critical supersaturation. Its precipitation decreases the calcium hydroxide concentration, increasing the supersaturation and, subsequently, the rate of hydration. Hence, precipitation of portlandite increases the rate of reaction [11].

Bellmann et al [19] conclude from Nuclear magnetic resonance (NMR) data that dimeric silicates are formed just after the end of the dormant period, being an important mechanism for the nucleation and growth kinetics transition. Moreover the sensitivity of the technique leads to believe that it can be formed from the initial ages, as described above.

At high temperature the C-S-H is stable as the crystallization is favorable, while in room temperature it slows down leading to nanocrystalline phases [21].

Regarding the hydration mechanism, C_3S firstly dissolves congruently after protonation of SiO^{4-}_4 ions to give a supersaturated solution with respect to C-S-H [2]:

$$Ca_3SiO_{5sh} + 4H_2O \rightarrow 3Ca^{2+} + 5OH^- + H_2SiO_4^{2-}$$

The precipitation of C-S-H follows the reaction [2]:

$$xCa^{2+} + 2(x-1)OH^- + H_2SiO_4^{2-} \rightarrow (CaO)_x - SiO_2 - (H_2O)_{x+y-1}$$

This can happen by homogeneous nucleation in the bulk of the supersaturated solution or by heterogeneous nucleation on a substrate's surface, such as C_3S grains [22].

Several theories have been proposed over the last years to explain this slow down on the rate of reactions, such as the presence of a protective membrane [23, 24] or a semi-permeable membrane [25]. The formation of a double layer is also proposed [26], as well as the role of crystallographic defects [27]. Finally the nucleation of CH [26] and C-S-H [28] are defended as causes of the induction period. Most recently the dissolution theory in the field of geochemistry is proposed [17].

2.6.1.1 Calcium Silicate Hydrate phase

The Calcium Silicate Hydrate (C-S-H) is the main product formed by the hydration of the calcium silicates and the responsible for the strength of the cement paste. For this reason this product is the focus of this research and is described in more detail here. It is mostly amorphous and the dashes indicate a disordered structure.

The C-S-H particle density was found by Gauffinet et al [22] to be in the order of 2500 kg/m^3.

At the molecular level, C-S-H has a structure similar to the tobermorite ($Ca_5Si_6O_{16}(OH)_2 \cdot 8H_2O$) and jennite ($Ca_9(Si_6O_{18})OH_6 \cdot 8H_2O$), rare minerals found in the nature. Most of the models predicting the C-S-H nanostructure involve elements of jennite-like or even tobermorite-jennite structures [29].

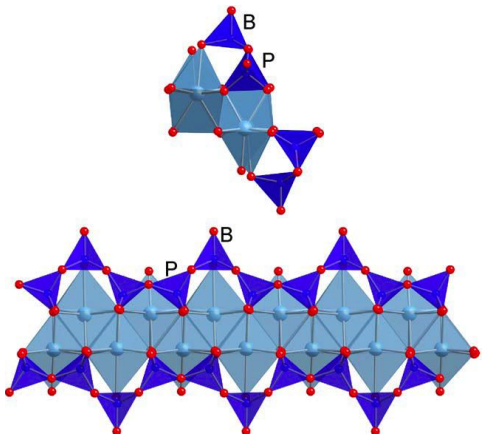

Figure 4 Dreierkette chains from 1.4 nm tobermorite (infinite chain length) projected along [010] (top) and [210]. In the kinked pattern of the chains the P silicate tetrahedra share O–O edges with the central Ca–O layer, while the B do not [32].

Both of these phases have a layered structure based on a calcium sheet flanked on each side by linear silicate chains called “dreierketten” or wollastonite-like chains. That means the chains repeat at an interval of three tetrahedra, where two adjacent are coordinated to the calcium ions of the layer (P, paired) while the third, the bridging tetrahedron (B), bridges two successive dimers [30] (Figure 4). Moreover the presence of foreign ions may cause changes on the C-S-H structure, mainly the Al^{3+} [29].

Both 1.4 nm tobermorite and jennite can vary in composition, degree of polymerization and extent of crystallinity while maintaining the essential features of the composite layer structure [31]. The 1.4 nm refers to the thickness of the elemental layers [29].

The interlayer spaces of 1.4 nm tobermorite contain water molecules and additional Ca cations that balance the negative charge of the composite layer. In 1.4 nm tobermorite the Ca/Si ratio is 0.83 [31].

On the other hand Jennite has a Ca/Si ratio of around 1.5, higher than in tobermorite [2]. The main difference is that in jennite alternate chains are replaced by rows of OH groups (Figure 5).

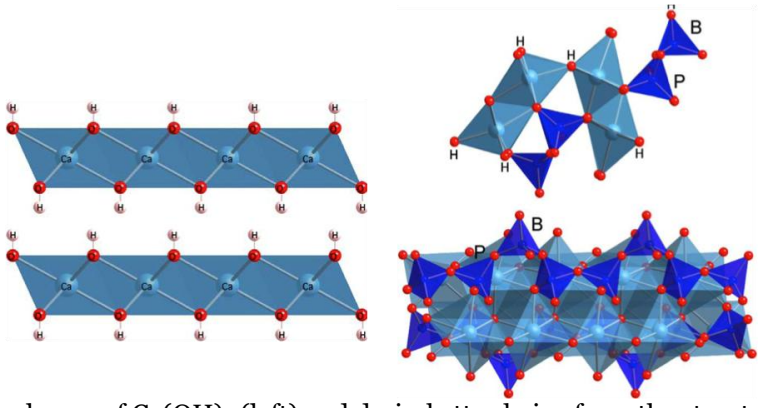

Figure 5 The layers of $Ca(OH)_2$ (left) and dreierkette chains from the structure of jennite (infinite length) projected along [010] (right top, where H are the hydroxyl groups) and [100] (right bottom). 'P' are paired and 'B' are bridging tetrahedra [32].

However in C-S-H most of the bridging tetrahedra are missing, mainly during the early ages when the average chain length is around 2, and gradually increases due to the incorporation of bridging tetrahedra. Even so in hardened cement or C_3S paste the Ca/Si ratio is typically about 1.75, ranging from 1.2 to 2.1 [33]. However Taylor [2] underlines that Ca/Si ratio varies over time as the structure changes from dimer ($[Si_2O_7H]^{5-}$) to larger species as pentamer ($[Si_5O_{16}H]^{11-}$) or even infinite chains (Figure 6); during the first minutes of reaction a material with lower Ca/Si ratio is formed by either a mixture of tobermorite-like and jennite-like structures or any of them separately. Finally, the dimeric structures are removed from the structure and larger chains are formed, decreasing the Ca/Si ratio with time. The relation between the ratio and the chain length was presented by him and is illustrated in Figure 7 [2].

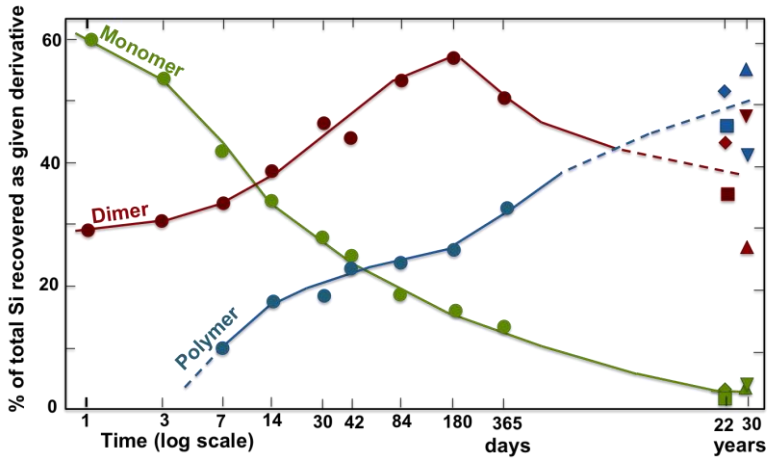

Figure 6 Percentages of the total silicon in C_3S or alite pastes recovered as monomer (green symbols), dimer (red symbols) and polymer (blue symbols). Differently shaped symbols denote different C_3S or alite specimens [2].

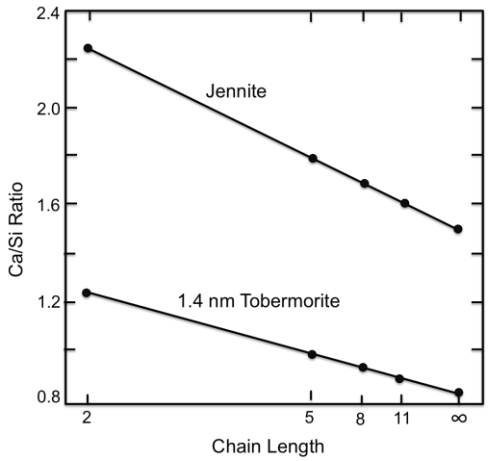

Figure 7 Calculated Ca/Si ratio *versus* chain length for jennite and 1.4-nm tobermorite modified by the omission of bridging tetrahedra [2].

In hardened cements it is possible to distinguish between two different morphologies formed on C-S-H, with the same chemical composition but different structure [34]. One, formed in the original boundaries of the original particles, is called inner product (Ip) and has globular morphology, with around 3 to 8 nm in diameter. The other one is called outer product (Op) and its morphology strongly depends on the chemical composition: in high Ca/(Si+Al) ratio it presents fibrillar morphology while in low Ca/(Si+Al) ratio it presents a foil-like or sheet-like morphology. It has fibrils formed by the agglomeration of long and thin particles with 3 nm by some tens of nanometers (Figure 8 and Figure 9) [34]. However the

structures can also be called high and low density product, as it is not always possible to identify if the product was formed inside or outside the grain boundaries.

The foil-like morphology is responsible for increasing the durability, as it is more efficient at filling spaces and decreasing the amount of interconnected capillary pores. It happens mainly in pastes with slag and pozollanic additions where the fibrillar morphology is gradually replaced by the foil-like as the hydration goes [33].

The inner product C-S-H generally presents a higher Ca/Si ratio than the outer product C-S-H. In Portland cement-slag systems the Ca/(Si+Al) ratio varies between 0.83 and 2.25 in Taylor's model, and between 0.67 and 2.5 in Richardson and Grove's model [29, 33, 35].

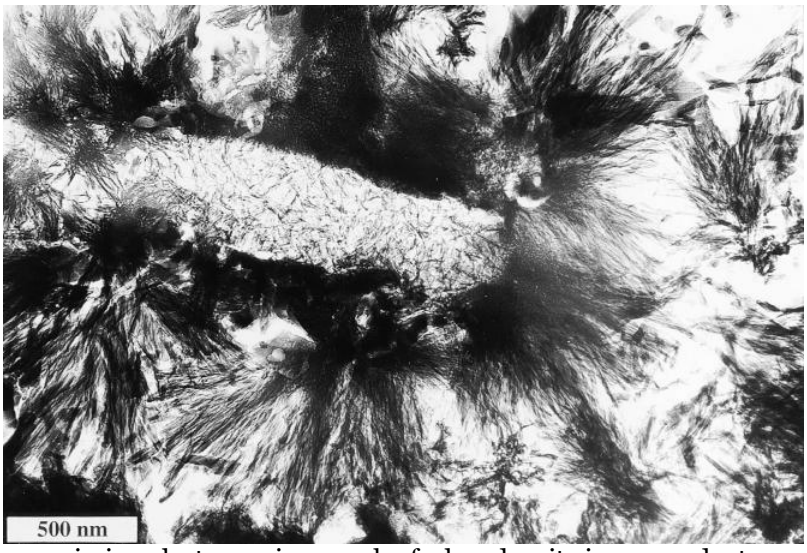

Figure 8 Transmission electron micrograph of a low density inner product surrounded by a border of dense C-S-H and fibrillar outer product C-S-H in a mature Portland cement paste [33].

Constantinides et al [36] suggested that the bimodal distribution of the elastic moduli at the micron level, measured by nanoindentation, could be attributed to the existence of these two different structures. However it is still controversial as some experimental artifacts may yield to the observed bimodal distribution.

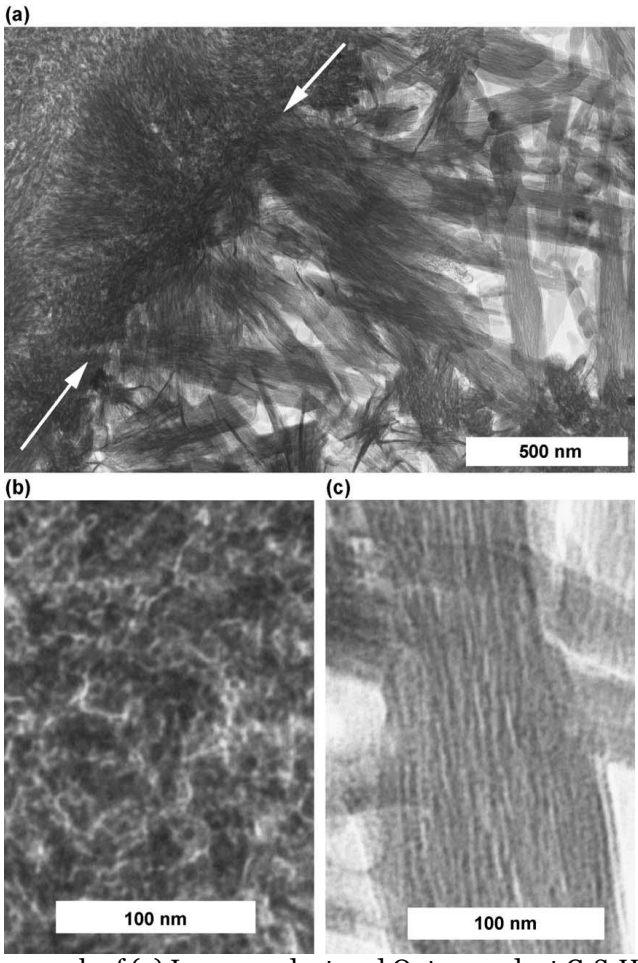

Figure 9 TEM micrograph of (a) Inner product and Outer product C-S-H in a C_3S paste (w/c = 0.4 @ 20°C for 8 years). White arrows indicate the Ip(top)–Op(bottom) boundary. (b) Magnification of an Ip region. (c) Magnification of a fibril Op [32].

Garrault et al [37] observed with Atomic force microscope that after 4 hours of hydration the C_3S surface is covered by small elements with size typically 60x30x5 nm with faces normally parallel to the surface, identified as being C-S-H. They used sintered pellets of tricalcium silicate polished with alumina powder and absolute alcohol to obtain a flat surface, attaining a final roughness of about 10 nm in 25 μm^2. A wet cell with lime-saturated solution was used to hydrate the tricalcium silicate, and they reported difficulties to scan the surface before 10 minutes of hydration (Figure 10). Within 7 hours of hydration the elements are arranged side-by-side and aligned. Afterwards the porosity is filled up, the reaction becomes controlled by diffusion and the morphology is less dense and more porous [37]

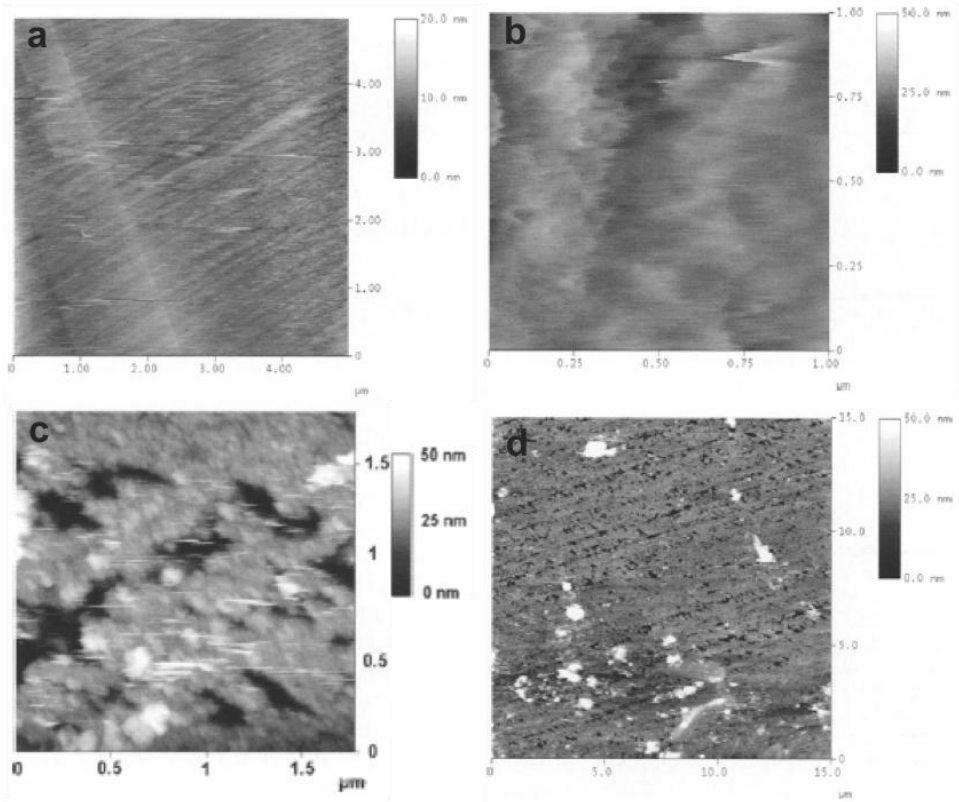

Figure 10 AFM observation of alite surface: (a) Initial condition in air. (b) After 10 minutes of hydration. (c) After 4 hours of hydration. (d) After 7 hours of hydration [37].

It is accepted that the minimum dimension of 5 nm for the nano crystals of C-S-H corresponds to 4 Ca-O layers, while the other dimensions are bigger and vary according to the growth environment. These nano crystals are packed in a compact manner with 4-6 nm pores in the inner product, while in the outer product, additionally to these, largest pores are noticed: 12 nm by N_2 absorption experiments [15] and 15-20 nm by NMR [38].

The capability of the C-S-H particle to bond with other hydration products strongly influences the strength of the Portland cement paste. Even appearing as crystals at micron-scale, the calcium hydroxide particles are admixed with C-S-H presenting an excellent bonding behavior [33]. In short, the strength depends much more on the adhesion between elements than on the inherent properties of each element [22].

Observation of C-S-H many times is laborious as most of the image techniques are performed under vacuum, so samples have to be dry prior to the analysis. Specimen preparation may be harsh or damaging and additionally drying or heating cause permanent changes on the C-S-H structure, changing the arrangement

of nanoparticles in cement [10]. At early ages the C-S-H, despite of being in low quantity on the cement paste, is not stable under vacuum and electron beam irradiation [22].

More severe microstructural changes occurs at higher drying rates in C-S-H at relative humidity greater than 85%, as the differential shrinkage is caused by the gradient of the capillary pressure instead of its magnitude. For this reason stronger irreversible changes occurs during rapid drying, mainly at early ages. On the other hand, older samples forms preferentially a fibrillar product particularly in more open regions, and the effect of drying is not the same as in younger samples. That happens mainly in the sample's surface, as the interior is less susceptible to drying effects [10].

2.6.1.2 Calcium Hydroxide phase

Calcium hydroxide (CH or portlandite) has a chemical formula $Ca(OH)_2$ and presents a layered structure. This is a product of the hydration of C_3S and C_2S and in highly diluted suspensions it stays completely dissolved in the liquid phase, but in other cases it precipitates as crystals with up to several tens of micrometers in diameter distributed in the hardened paste [3].

Portlandite is the second most abundant product in hydrated Portland cement pastes, after C-S-H. It can be easily identified in the paste with optical microscope because of the relatively large crystalline aggregates. The portlandite structure consists in calcium ion layers octahedrally coordinated and oxygen layers tetrahedrally coordinated with oxygen [3].

2.6.2 Hydration of clinker aluminates

The product of the hydration of C_3A is the AFt phase (Alumina, Ferric oxide, tri-sulfate), a group of calcium sulfoaluminate hydrates. The ettringite is the most important. Its general formula is $Ca_6Al_2(SO_4)_3(OH)_{12} \cdot 26H_2O$.

The AFt content decreases with the hydration of the cement paste, and it can be completely absent in mature pastes [3].

The tricalcium aluminate reacts with water and the calcium sulfate (from gypsum) present during the Portland cement hydration in different ways. In the first case the initial product is a gel-like material that appears around the grain surface,

provoking a slowdown in the reactions by the formation of a barrier around the grain. Some crystals of C_2AH_8 and C_4AH_{19} are formed from this gel as hexagonal phases and precipitate from the liquid phase. Those are transformed later in cubic C_3AH_6, when the barrier is disrupted and the hydration goes in a fairly high speed. The rate of reaction slows down with the presence of calcium hydroxide and only C_4AH_{19} is formed as a primary product, which with the progress of the reaction is again transformed in C_3AH_6 [3].

On the other hand, the presence of calcium sulfate slows down the reaction, reason why it is used in Portland cements, avoiding the instantaneous setting of the paste. That happens probably because the grains are covered with a layer of alumina-gel, blocking the contact with the liquid for some time, but there are several different theories to explain that. After a fast initial reaction with high release of heat, the sulfate dissolves and ettringite is formed. The dormant period starts and its length can vary depending on the amount of calcium sulfate in the original paste. The ettringite formed initially reacts with additional C_3A forming hexagonal monosulfoaluminate in form of a solid solution or as separated crystals, causing a second heat peak. A nearly complete hydration of C_3A is attained within several months [3].

Hydration of C_4AF leads to the formation of AFm phase (Alumina, Ferric oxide, mono-sulfate), a group of calcium aluminate hydrates where the most important anions in Portland cement are hydroxyl, sulfate and carbonate. Its general formula is $[Ca_2(Al,Fe)(OH)_6] \cdot X \cdot nH_2O$, where X is SO_4^{2-} and many other anions in different quantities.

The C_4AF reaction slows down in presence of portlandite or gypsum (strongly), due to the formation of an AFt layer around the C_4AF grain surface. In the absence of gypsum the initial product is an AFm ($C_2(A,F)H_8$ and/or $C_4(A,F)H_x$), while in the presence of lime just the $C_4(A,F)H_x$ is formed. With gypsum and lime (or just gypsum) an AFt phase $C_6(A,F)\bar{S}_8H_{32}$ is formed after an iron-rich, alumina gel or C_2AH_8.

2.7 Hydration of ordinary Portland cement

In Portland cement the kinetics of the reaction is determined by several factors such as the phase composition, incorporation of foreign ions, clinker

manufacturing, characteristics of the calcium sulfate, cement particle size, water/cement ratio, curing conditions, temperature, the presence of chemical admixtures, among others [3]. Figure 11 points up the development of the hydrated phases during the process in a Portland cement paste.

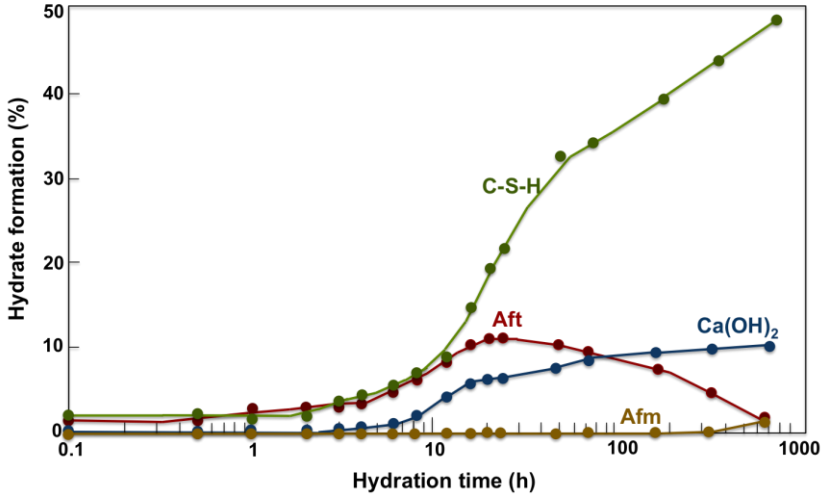

Figure 11 Formation of products in hydration kinetics of an ordinary Portland cement at ambient temperature [3].

The reactions occur in different velocities by dissolving the cement grain and forming the hydrated phases. The C-S-H phase is formed from the C_3S and C_2S, as explained before. The calcium hydroxide is also a product of the hydration of C_3S and C_2S and starts to form after the induction period finishes. The formation of the $C_2(A,F)$ form of AFt also depends on the hydration of the calcium silicates while the formation of AFm phases depends both on the hydration of C_3A and $C_2(A,F)$ and the form of the sulfate present, as with normal sulfate contents all the calcium sulfate is consumed and the formation of AFt finishes after 24 hours of mixing, reacting with additional C_3A and $C_2(A,F)$ to form the AFm phase.

The hydration process is exothermic, i.e. releases heat during the process. This heating of the system will accelerate the reactions, and the total heat generated during the process shows the evolution of the cement hydration. C_3A is the most reactive phase, influencing directly the workability of the paste and consuming a high amount of water during the hydration [7].

After the contact with water, ions start to be dissolved, including the calcium sulfate, until the saturation. Following that the anhydrous phases C_3S, C_3A e C_4AF

start to dissolve forming small ettringite needles around the cement grain. A C-S-H gel forms, provoking an exothermic peak (stage *I* in Figure 12).

$$C_3A + 3CaSO_4 \cdot 2H_2O + 26H_2O \rightarrow 3CaO \cdot Al_2O_3 \cdot 3CaSO_4 \cdot 32H_2O$$

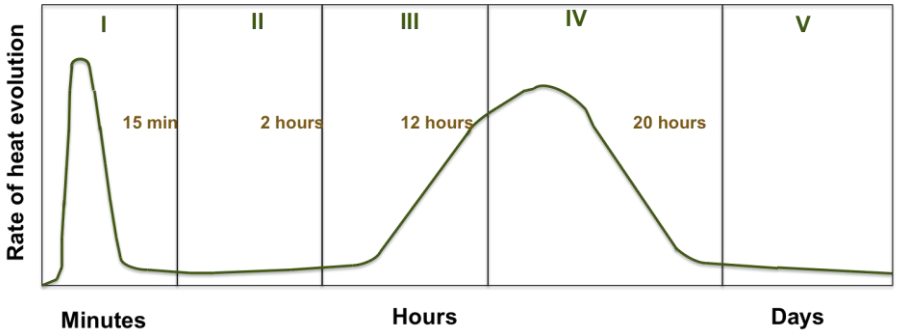

Figure 12 Hydration stages [19].

After this fast period a slowdown on the C_3A formation occurs, starting the dormant period (stage *II*), which depends on the quantity of sulfates in the clinker. Finishing the added sulfate by the abstention of limestone, monosulfate starts to be formed from the ettringite and C_3A available [15].

$$2C_3A + CaO \cdot Al_2O_3 \cdot 3CaSO_4 \cdot 32H_2O + 4H_2O \rightarrow 3CaO \cdot Al_2O_3 \cdot CaSO_4 \cdot 12H_2O$$

At the end of the dormant period C_3S and C_2S react to form C-S-H phases and portlandite, with C_3S forming more portlandite, according to the following equations. The heat release increases again (stage *III*). The final setting time occurs during this period and the hardening of the cementitious system starts [15].

$$2C_3S + 6H_2O \rightarrow 3CaO \cdot 2SiO_2 \cdot 3H_2O \cdot 3Ca(OH)_2$$

$$2C_2S + 4H_2O \rightarrow 3CaO \cdot 2SiO_2 \cdot 3H_2O \cdot Ca(OH)_2$$

The ettringite is converted in calcium trisulfoaluminate hydrated by the reaction with ions Al^{3+}, starting the stage *IV*. The ions remaining form a protection around the grain with the Ca^{2+}, starting the stage *V*. Figure 13 shows images of Portland cement during the hydration progress with the formation of ettringite needles (indicated by the arrows), which can be observed after 55 minutes of hydration.

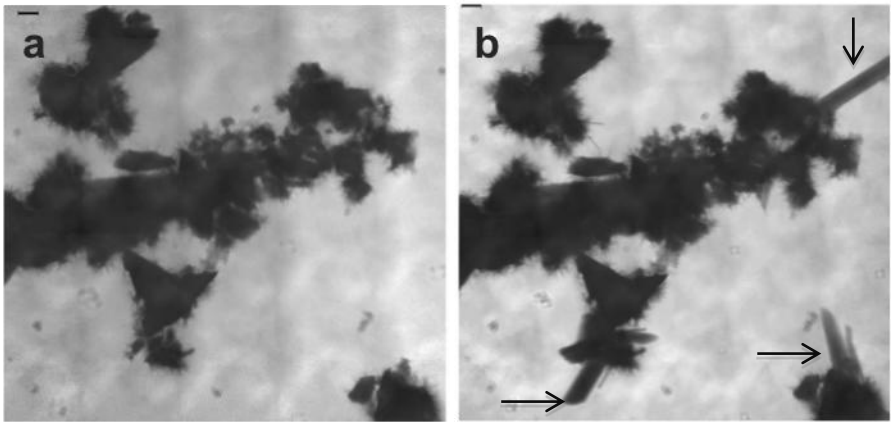

Figure 13 Soft X-Ray image of Portland cement in solution saturated with $Ca(OH)_2$ and $CaSO_4.2H_2O$. (a) 15 min (b) 55 min. Scalebar = 1 μm [39].

2.8 References

[1] P. J. Jackson. Portland cement: classification and manufacture. In P. C. Hewlett, Lea's Chemistry of cement and concrete. 2001. Oxfort, USA: Butterworth-Heinemann. 25-88.

[2] H. F. Taylor. Cement Chemistry. 2nd ed. 1990.London: Academic Press.

[3] I. Odler. Setting and Hardening of Portland Cement. In P. C. Hewlett, Lea's Chemistry of Cement and Concrete 1057p. 1998. Oxford: Butterworth-Heinemann.

[4] H. Pöllman. Composition of Cement Phases. In J. Bensted, & P. Barnes, Structure and Performance of Cements. 2nd ed. 2002. London: Spon Press.

[5] M. Regourd. Crystal chemistry of Portland cement phases. In Structures and Performance of Cements, Editor P. Barnes, 150. 1983. Applied Science Publishers LTD.

[6] V. S. Ramachandran, R. M. Paroli, J. Beaudoin, A. Delgado. Handbook of thermal analysis of construction materials. N. R. Canada, Ed. 2002. New York: Noyes Publications.

[7] A. P. Kirchheim. Cubic and orthorhombic tricalcium aluminate: analysis of in situ hydration and products. PhD thesis, 265. 2008. Porto Alegre, Brazil: Universidade Federal do Rio Grande do Sul.

[8] A. P. Kirchheim, V. Fernàndez-Altable, P.J.M. Monteiro, D.C.C. Dal Molin, and I. Casanova. Analysis of cubic and orthorhombic C_3A hydration in presence of gypsum and lime. Journal of Materials Science 44 (2009) 2038-2045.

[9] S. Popovics Concrete Materials - Properties, Specifications and Testing. 2nd ed. 1992. New Jersey: Noyes Publications.

[10] P. Fonseca, H. Jennings. The effect of drying on early-age morphology of C-S-H as observed in environmental SEM. Cement and Concrete Research 40 (2010) 1673-1680.

[11] K. L. Scrivener, A. Nonat, Hydration of cementitious materials, present and future. Cement and Concrete Research 41 (2011) 651-665.

[12] P. Juilland, E. Gallucci, R. Flatt, K. Scrivener. Dissolution theory applied to the induction period in alite hydration. Cement and Concrete Research 40 (2010) 831-844.

[13] J. W. Bullard, H. M. Jennings, R. A. Livingston, A. Nonat, G. W. Scherer, J. S. Schwitzer, et al. Mechanisms of cement hydration. Cement and Concrete Research 41 (2011) 1208-1223.

[14] J. J. Thomas, J. J. Biernacki, J. W. Bullard, S. Bishnoi, J. Dolado, G. W. Scherer et al. Modeling and simulation of cement hydration kinetics and microstructure development. Cement and Concrete Research 41 (2011) 1257-1278.

[15] M. M. Costoya Fernandez. Effect of particle size on the hydration kinetics and microstructural development of tricalcium silicate. École Polytechnique Fédérale de Lausanne, Lausanne, Switzerland. 2008.

[16] S. Garrault-Gauffinet, A. Nonat. Experimental investigation of calcium silicate hydrate (C-S-H) nucleation. Journal of crystal growth 200 (1999) 565-574.

[17] P. Juilland. Early Hydration of Cementitious Systems. PhD Thesis, École Polytechnique Fédérale de Lausanne, Lausanne, Switzerland. 2009.

[18] S. Garrault, A. Nonat. Hydrated layer formation on tricalcium and dicalcium silicate surfaces: experimental study and numerical simulations. Langmuir 17 (2001) 8131-8138.

[19] F. Bellman, D. Damidot, B. Möser, J. Skibsted. Improved evidence for the existence of an intermediate phase during hydration of tricalcium silicate. Cement and Concrete Research 40 (2010) 875-884.

[20] X. Cong, R. Kirkpatrick. ^{17}O and ^{29}Si MAS NMR study of β-C_2S hydration and the structure of calcium silicate hydrates. Cement and Concrete Research 23 (1993) 1065-1077.

[21] P. Blanc, X. Bourbon, A. Lassin, E. Gaucher. Chemical model for cement-based materials: Temperature dependence of thermodynamic functions for nanocrystalline and crystalline C-S-H phases. Cement and Concrete Research 40 (2010) 851-866.

[22] S. Gauffinet, E. Finot, A. Nonat. Experimental study and simulation of C-S-H nucleation and growth. 2nd International Rilem Symposium on hydration and setting (1997) 199-214. Rilem Publications SARL.

[23] H. Jennings, P. Pratt. An experimental argument for the existence of a protective membrane surrounding Portland cement during induction period. Cement and Concrete Research 9 (1979) 501-506.

[24] E. Gartner, H. Jennings. Thermodinamics of calcium silicate hydrates and their solutions. Journal of the American Ceramic Society 70 (1987) 743-749.

[25] D. Double, A. Hellawell, S. Perry. The hydration of Portland cement. Proceedings of the Royal Society A 359 (1979) 435-451.

[26] M. Tadros, J, Skalny, R. Kalyoncu. Early hydration of tricalcium silicate. Journal of the American Ceramic Society 59 (1976) 344-347.

[27] I. Odler, J. Schúppstuhl. Early hydration of tricalcium silicate III. Control of the induction period. Cement and Concrete Research 11 (1981) 765-774.

[28] S. Garrault, A. Nonat. Experimental investigation of calcium silicate hydrate (C-S-H) nucleation. Journal of crystal growth 200 (1999) 565-574.

[29] H. Taylor. Proposed structure for Calcium Silicate Hydrate Gel. Journal of the American Ceramic Society 69 (1986) 464-467.

[30] A. Nonat. The structure and stoichiometry of C-S-H. Cement and Concrete Research 34 (2004) 1521-1528.

[31] J. J. Chen, J. J. Thomas, H. F. Taylor, H. M. Jennings. Solubility and Structure of calcium silicate hydrate. Cement and Concrete Research 34 (2004) 1499-1519.

[32] I. Richardson. Tobermorite/jennite- and tobermorite/calcium hydroxide-based models for the structure of C-S-H: applicability to hardened pastes of tricalcium silicate, β-dicalcium silicate, Portland cement, and blends of Portland cement with blast-furnace slag, metakaolin, or silica fume. Cement and Concrete Research 34 (2004) 1733–1777.

[33] I. Richardson. The nature of C-S-H in hardened cements. Cement and Concrete Research 29 (1999) 1131-1147.

[34] I. Richardson. The calcium silicate hydrates. Cement and Concrete Research 38 (2007) 137-158.

[35] I. Richardson, G. Groves. Models for the composition and structure of calcium silicate hydrate (C-S-H) gel in hardened tricalcium silicate pastes. Cement and Concrete Research 22 (1992) 1001-1010.

[36] G. Constantinides, F. Ulm, K. Van Vliet. On the use of nanoindentation for cementitious materials. Materials and Structures 36 (2003) 191-196.

[37] S. Garrault, E. Finot, E. Lesniewska, A. Nonat. Study of C-S-H growth on C_3S surface during its early hydration. Materials and Structures 38 (2005) 435-442.

[38] J. Korb, L. Monteilhet, P. McDonald, J. Mitchell. Microstructure and texture of hydrated cement-based materials: A proton field cycling relaxometry approach. Cement and Concrete Research 37 (2007) 295-302.

[39] M. C. Juenger, V. H. Lamour, P. J. M. Monteiro, E. M. Gartner, G. P. Denbeaux. Direct observation of cement hydration by soft X-ray transmission microscopy. Journal of Materials Science Letters 22 (2003) 1335-1337.

3 Synthesis and characterization of thin films of clinker phases

Several studies have been developed over the last years to understand cement hydration in small scale as it allows improvements on durability, strength, costs and environmental impact reducing.

These studies are performed using diverse techniques that give different information and, by grouping them, many conclusions can be derived. On the other hand, the success of many techniques depends largely on the quality of the samples used. For example, the atomic force microscope (AFM) and nanoindentation studies request very flat surfaces to give high-resolution data. Detailed information on these techniques can be found in the literature [1-5].

Previous research on cementitious materials using the AFM technique prepared the specimens, for example, by polishing sintered pellets of tricalcium silicate with alumina powder and absolute alcohol, obtaining a final roughness of 10 nm in 25 μm^2 [1] or cutting discs of Portland cement clinker or cement paste with a diamond saw, polishing it with sandpapers [2, 3, 4]. In order to analyze powder samples, Lomboy et al [5] mixed it with epoxy and polished it after curing. The problem with these techniques is that they may cause cracks and striations due to the mechanical action on the sample, decreasing the quality of the results (Figure 14).

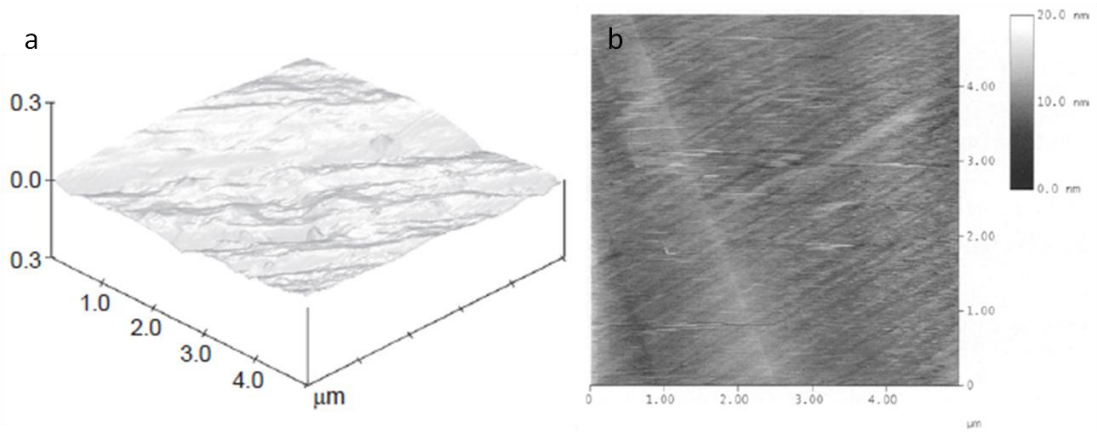

Figure 14 Cement (a) and alite (b) surface observed with AFM in air after polishing [1, 5 respectively]. Striations can be due to the polishing process.

Other techniques such as X-ray photoelectron spectroscopy (XPS, detailed in [6, 7]) do not require any particular sample preparation or cleavage surfaces: grains, powders and fibers may be analyzed in the same way [6]. However it is necessary to take into account that these kinds of samples harm the system and additional time is necessary to reach the vacuum level required to run the test. On the other hand, even if special sample preparation is not mandatory for usual measures, the use of flat uniform surfaces permits to follow the depth of surface reactions with the XPS. This provides information on chemical changes due to the hydration of clinker phases on the surface and the products formed can be tracked.

Furthermore some techniques require the samples to be thin enough to be transparent. It is known that cement, or even pure phases particles are not sufficiently small and specific sample preparation is needed. This is the case of samples for Scanning transmission X-ray microscopy (STXM) [8, 9] or Full-field soft X-ray transmission microscope (XM-1) [10], where normally powder specimens are used in solution after centrifugation to select small particles, and transmission electron microscopy (TEM) [11, 12], where grinding, extraction and ion milling are normally used.

The effort to produce clinker phase thin films by electron beam evaporation technique is presented here aiming to synthesize suitable samples for nanoscale studies of cement hydration. Evaporations of each phase were repeated several times adjusting the parameters so it is possible to certify the reproducibility of the process.

Each synthesized sample was characterized by XPS and Grazing angle X-ray diffraction (GAXRD) in order to verify their chemical and mineralogical composition when compared to the bulk material.

Additionally, this chapter presents the details of each technique used in this thesis for the production and characterization of thin films of clinker phases, as well as for the data acquisition on the dissolution and hydration of the calcium silicate thin films.

3.1 Materials

Tricalcium silicate (C_3S), ß-dicalcium silicate (C_2S), tricalcium aluminate (C_3A) and ferrite (C_4AF) were provided by Mineral Research Processing. The phases were synthesized by melting, sol-gel processing and grounded to 3600 cm^2/g with a free lime content below 0.5%. The material was kept in a desiccator to minimize hydration during storage. The X-Ray diffraction (XRD) patterns for each of the bulk pure phase are presented later when compared with the thin film spectra.

X-ray fluorescence analyses (XRF) for each clinker phase are presented in Table 1.

Table 1 XRF of the synthesized clinker phases.

Phase	Weight %			
	C_3S	C_2S	C_3A	C_4AF
CaO	72.32	63.06	61.44	45.88
SiO_2	27.54	36.59	-	-
MgO	-	0.337	0.366	0.257
Al_2O_3	-	-	36.21	20.63
Fe2O3	-	-	-	32.84
MnO	-	-	-	0.107

3.2 Methods

For the development of this research several tools were used to produce, characterize and hydrate thin films of clinker phases. The main techniques used in each phase are summarized below and described in this section.

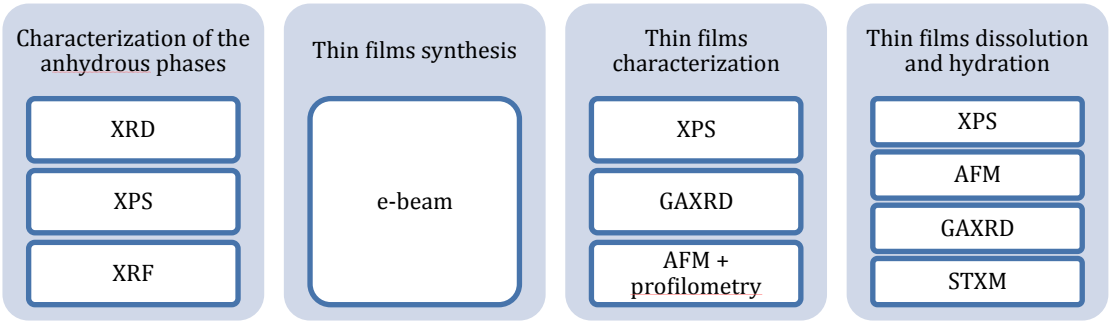

Figure 15 Summary of the experimental work and techniques used.

3.2.1 Powder X-ray diffraction

X-ray diffraction (XRD) is one of the most used techniques for microstructural characterization of materials and is widely used for cementitious materials. It consists basically in bombarding the sample with a monochromatic beam of X-rays, while their diffraction by the crystalline structure is recorded.

Here the bulk materials were analyzed with a Bruker D83 Advanced diffractometer operating at an accelerating voltage of 40 keV on a Cu Kα anode, irradiation intensity of 40 mA, and 40 scans in steps of 0.02 deg/s.

3.2.2 Grazing angle X-ray diffraction

Due to the small diffracting volumes which result in low intensities compared to the substrate and background, thin films are very difficult to analyze and to have their mineralogical phases identified. Grazing angle X-ray diffraction (GAXRD) allows increasing the intensity from the film by increasing the path length of the incident X-ray beam through it (Figure 16), so that conventional phase identification analysis can be run.

A Bragg-Brentano Siemens D-500 X-ray diffractometer was used for grazing angle experiments operating at an accelerating voltage of 45 kV on a Cu Kα anode, irradiation intensity of 40 mA, with steps of 0.05 deg/s. Because of the thickness of the samples the incident angle used was w=0.4º. Measures were done without monocromator in order to increase the signal in diffraction angles between 10º and 70º.

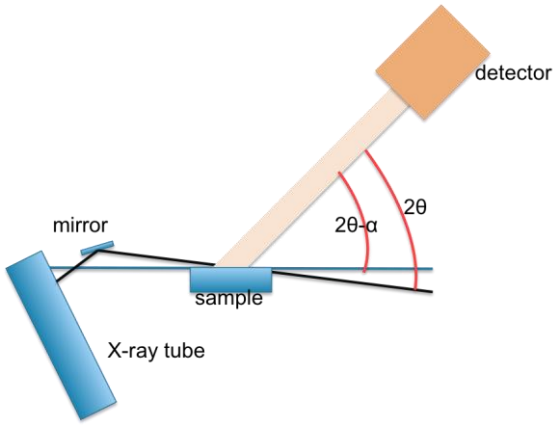

Figure 16 Scheme of the Grazing angle X-ray diffraction set up.

3.2.3 Electron beam evaporator

Thin films were prepared in different evaporations at different conditions using an electron beam evaporator. For that a current is sent through a tungsten filament outside the deposition zone in order to avoid any contamination. The filament is heated until the thermionic emission of electrons starts. Magnets are located inside the chamber focusing and directing the electrons toward the bulk material, which is inside a crucible constantly cooled.

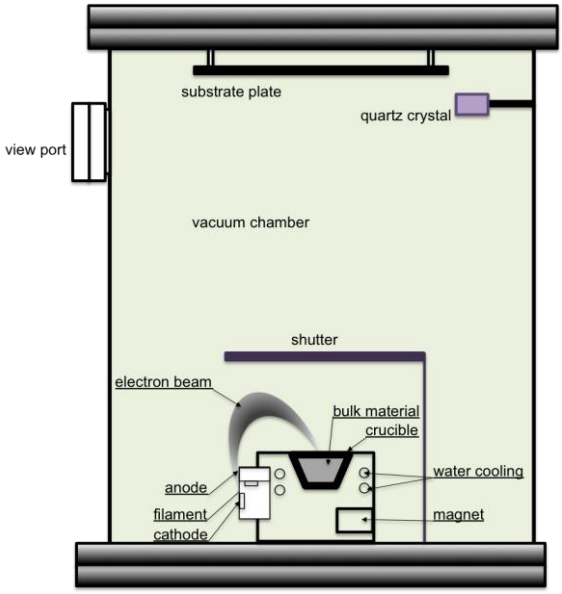

Figure 17 Scheme of an electron beam evaporator.

When the electron beam hits the sample surface, the kinetic energy is transformed into heat, releasing high energy. At this point the sample boils and evaporates, condensing on the substrate and all the surfaces inside the vacuum chamber. The electron beam evaporation system is illustrated in Figure 17.

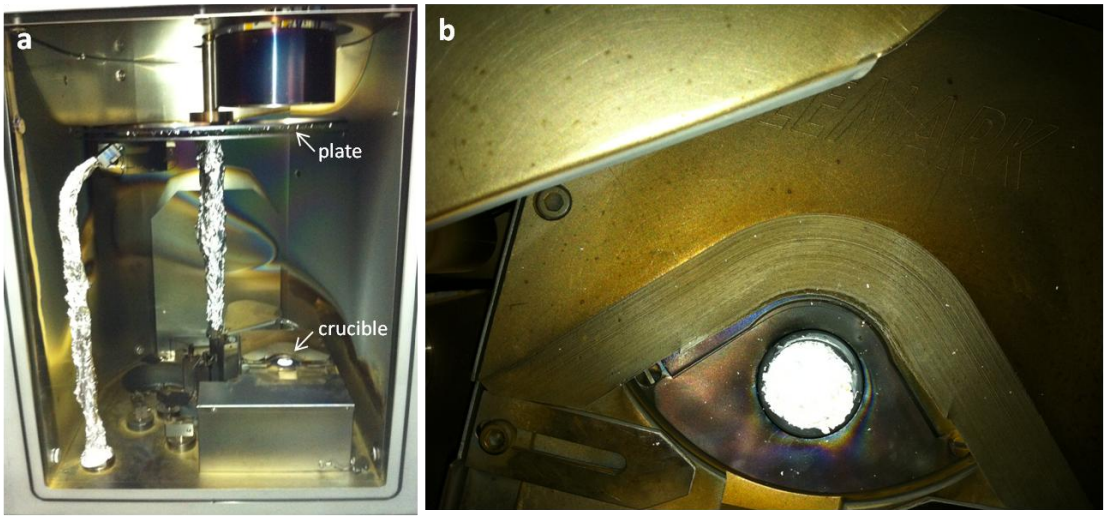

Figure 18 Electron beam evaporator: (a) inside the vacuum chamber and (b) detail of the crucible.

Thicknesses of the films are a function of irradiation time and can be estimated with an in situ quartz deposition balance. This kind of equipment can

detect up to 10^{-16} kg by measuring changes in frequency of a resonator, that changes with any change in the film deposited on the acoustic resonator's surface [13].

The bulk powder phases were cleaned with isopropyl alcohol, placed in a crucible (Figure 18b) and mounted in a vacuum chamber Univex 450B Oerlikon Leybold (Figure 18a) at Instituto de Microelectrónica de Barcelona (IMB) in a clear room to avoid any contamination. A power supply controller Telemark was used with a beam generating system and beam deflection unit with electromagnetic deflection for the x and y-axis in the electron beam evaporator.

Silicon wafers with orientation 100 were used as deposition substrate after cleaned with isopropyl alcohol and acetone. They were dried, placed in a plate at 30 cm above the crucible and held by metallic clips (Figure 19).

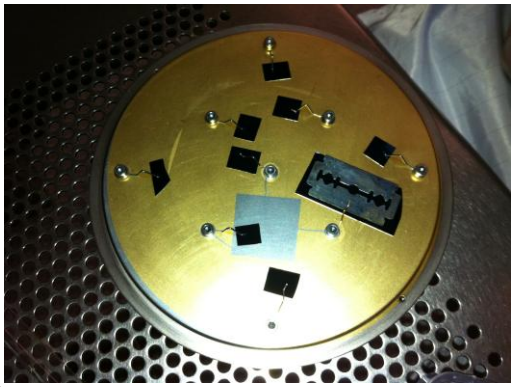

Figure 19 Silicon wafers held by metallic clips.

3.2.4 X-ray photoelectron spectroscopy

The X-ray photoelectron spectroscopy allows measuring the chemical composition of a material's surface by irradiating it with a beam of X-rays and measuring the kinetic energy and the number of electrons that escape from the surface, providing spectra for all the elements. It requires ultra high vacuum conditions (Figure 20).

The surfaces characterized are typically around 10 nm deep. Elemental analyses are possible as each element yields photoelectrons of a specific binding energy. On the other hand, small changes in the chemical bonding environment cause changes in the photoelectron energy, providing chemical information [7].

In detail, it uses X-rays to eject the electrons of the element from their inner-shells orbitals. The kinetic energy (E_k) of the photoelectrons can be related to its binding energy (E_b) originally in the solid:

$$E_k = h\nu - E_b - \phi_s \qquad \textbf{Equation 3.1}$$

Where $h\nu$ is the energy of the photon, E_b is the binding energy of the atomic orbital from which the electron originates, and ϕ_s is the spectrometer work function.

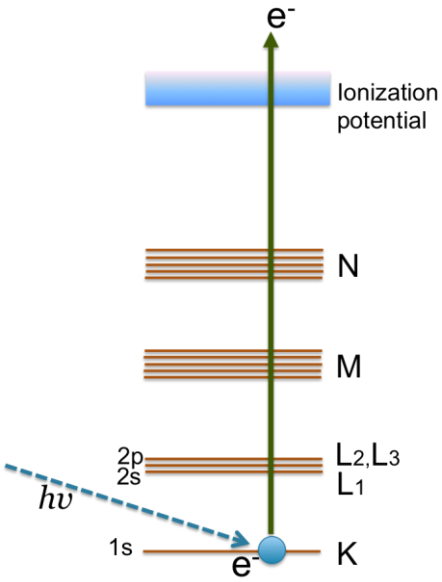

Figure 20 Scheme of the principles of X-ray photoelectron spectroscopy (XPS).

In XPS the depth of investigation into the oxides and silicates is between 50 and 100 Å. The intensity peak measurements are easily reproduced and normally have a quality of more than 10%, providing the determination of the ratio of concentrations in a homogeneous material. It is important the fact that the samples do not require any particular preparation and cleavage surfaces: grains, powders and fibers may be analyzed in the same way [6].

The area analyzed by the XPS is a function of the aperture of the detector and the energy resolution depends on this factor: the use of large apertures leads to higher signal collected. A circular analysis area used is normally around 5 mm in diameter.

The chemical composition of the thin films was verified using a SPECS X-ray photoelectron spectroscopy system equipped with an Al anode XR50 source operating at 150 W and a Phoibos MCD-9 detector in high vacuum in the Center for Research in Nanoengineering (CRnE, UPC) (Figure 21a). Spectra were recorded with pass energy of 25 eV at 0.1 eV steps at a pressure below 10^{-9} mbar.

Figure 21 (a) XPS at CRnE; (b) thin film on the sample holder; (c) inside the analysis chamber.

For the hydration experiments in this equipment a reaction chamber in the same vacuum line as the XPS was used, thus avoiding any atmospheric contamination due to the manipulation of the sample (Figure 22). A vaporizer with milli-Q water was used to insert water vapor in saturated state using argon as a carrier with a flux of 20 mL/min. Prior to hydration the system was always purged for 5 minutes to avoid any contamination.

Figure 22 (a) reaction chamber closed. (b) External view of the reaction chamber. (c) Vaporizer. (d) Detail of the sample inside the reaction chamber.

3.2.5 Focused Ion Beam/Scanning electron microscope system (FIB/SEM)

A Focused Ion Beam/Scanning electron microscope system (FIB/SEM) (Zeiss Neon 40) was used for observation and selective milling of samples. The equipment is a Galium FIB with 1 pA-50 nA, 2-30 kV and 7 nm resolution, and the SEM (Shottky FE) with a 4 pA-20 nA, 0.1-30 kV, and 1.1 nm resolution depending on the sample. A gas injection system was used for selective milling and deposition of platinum to avoid ion beam defocusing.

3.2.6 Scanning transmission X-ray microscope

Scanning transmission x-ray microscopy (STXM) combines spectroscopy and microscopy, imaging with spectral sensitivity and recording spectra from very small spots at once. In this way it provides, with high spatial resolution, quantitative information on the specimen's local elemental and chemical composition and magnetization.

It can be done by measuring the differential absorption of X-rays in an image contrast data, which depends on the chemical composition of the sample, or by scanning the sample in the x–y direction, the plane perpendicular to the X-ray beam (image stack) or x direction, the horizontal direction (line scan), of selected areas of interest in the sample at determined energy increments (0.1 eV) over the energy range of interest. The energy of interest depends on the element to be analyzed: 280–305 eV for carbon, 342–360 eV for calcium and 1825–1890 eV for silicon [8].

When the incident photon energy exceeds the binding energy needed to remove completely (ionize) an electron from an orbital shell, the X-ray absorption edge is reached. In the case of C 1s, with ionization edge of 280–300 eV, for example, photons with energy just below that can promote core electrons into a variety of bound states that correspond to unoccupied or partially occupied molecular orbitals. Consequently different near edge absorption bands happens and local chemical bonding environment changes are noticed around that atom. The STXM provides with the stack image, NEXAFS (near edge X-Ray Absorption Fine Structure) spectrum for a specific element on each pixel of the image [9].

In the STXM the mono-energetic X-rays from a monochromator beamline on a synchrotron source is focused by a Fresnel zone plate.

The Fresnel zone plate is a set of Fresnel zones, radially symmetric rings that alternate between opaque and transparent. When heating the zone plate, light will diffract around the opaque zones, interfering in the desired focus and creating the image there. In the STXM the focal point is around 50 nm in diameter over a 3-10 μm waist.

The X-ray transmitted through a thin section of the sample when scanned is monitored, forming the image. Holding the beam in a single point in the sample while the photon energy is scanned allow measuring the micro-spectra.

The STXM is mounted in a vacuum chamber, where samples can be analyzed in air, helium, nitrogen or carbon at atmospheric pressure, or even sandwiched between two X-ray transparent silicon nitride windows. In this way samples can be studied in water.

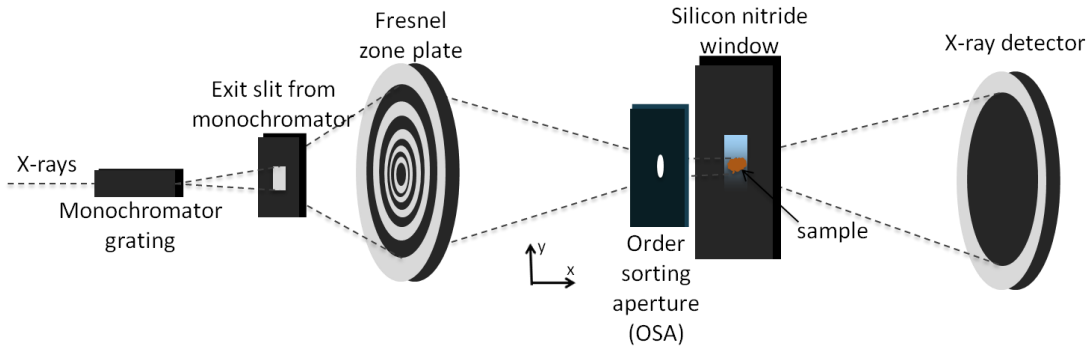

Figure 23 Scheme of the STXM.

The transmitted X-ray signal is measured by single photon counting. The dwell time (or counting periods) is normally around 0.2 - 0.5 ms per pixel for imaging, and one pixel can be as small as 25-30 nm. A 300x300 pixel image takes about 30 seconds to be acquired.

Energy is calibrated with the C 3p Rydberg peak of gaseous CO_2 for the C K-edge, quartz for Si K-edge, and calcite for Ca $L_{II,III}$ edges [8].

This signal is converted to optical density (OD) for quantitative analysis, which is sensitive for sample thickness, density and composition, according to:

$$OD = \ln\left(\frac{I_0}{I}\right) \qquad \textbf{Equation 3.2}$$

Where:

Io is the incident x-ray flux, that is, the background;

I is the transmitted flux through the sample;

The OD is directly related to the sample properties by:

$$OD = \mu(E) \cdot \rho \cdot t$$ **Equation 3.3**

Where:

$\mu(E)$ is the mass absorption coefficient at X-ray energy E. It is derived from measurements of the NEXAFS spectra of the pure material.

ρ is the density of the sample;

t is the sample thickness.

By measuring a set of pixels and converting them, with the incident flux the X-ray, the optical density image at single photon energy is obtained. On the other hand, by changing the photon energy it is possible to take a stack (image sequence) with chemical and topographical information.

The STXM results in this thesis were collected at at the Laurence Berkeley National Laboratory (LBNL) in Berkeley, United States, in cooperation with the group of Prof. Monteiro from the Department of Civil and Environmental Engineering of University of California, Berkeley.

The ALS lines 5.3.2.1 and 5.3.2.2 at the Advanced Light Source (ALS) were used with the synchrotron storage ring operating at 1.9 GeV and 200–400 mA stored current. These lines use 30 nm zone plate for environmental and chemical studies.

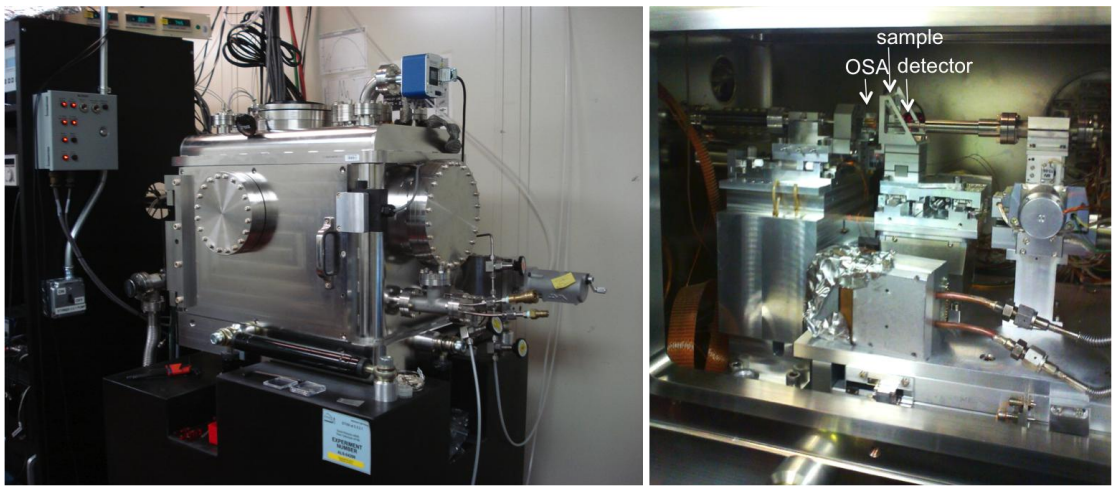

Figure 24 STXM at ALS beamline 5.3.2.1, external and internal view.

The STXM beam station 5.3.2.2 goes to the energy range 250–800 eV, while the beam station 5.3.2.1 is capable of 25–30 nm spatial resolution over the energy range 350–2500 eV for imaging and NEXAFS spectrum.

3.2.7 Atomic force microscope

The atomic force microscope (AFM) is a tool for topography and force measurements with high-resolution surface structure observation at normal conditions as no vacuum is required. It can provide important information to understand the properties of cementitious materials, allowing real time imaging during reaction. It can be used as a tool to evaluate the hydration process of the clinker phases at early ages, determining changes in morphology with variations of deposition parameters.

AFM consists in a microscale cantilever with a sharp probe at its end that is used to scan the specimen surface. When the tip is brought into proximity of a sample surface, forces between the tip and the sample lead to a deflection of the cantilever. It can be used in tapping or contact mode, depending on the type of sample and on the kind of information needed. However the success of the technique depends largely on the quality of sample so flat surfaces are necessary.

In this research a Veeco MultiMode IIIa atomic force microscope (Figure 25a) was used to measure the topography of the samples surface and identify changes in roughness and surface area variations in both tapping and contact mode, even in liquid. The equipment allows a scan size up to 12 μm in the X-Y plain, and a Z range up to 5 μm, while samples up to 15 mm in diameter having a maximum thickness of 6 mm can be analyzed.

It requires very flat surfaces, which have been achieved using the electron beam evaporation mentioned above. In order to scan the samples surface in real time during the hydration in fluid, the sample is enclosed and probed in a fluid environment by using a liquid cell at environment conditions (Figure 25c-e). Liquid was inserted into the cell by a peristaltic pump at a constant flux of 6.4 μm/min (Figure 25b).

Images were captured continuously, each of them taken approximately 9 minutes to be finished for 5, 2 or 1 μm square images.

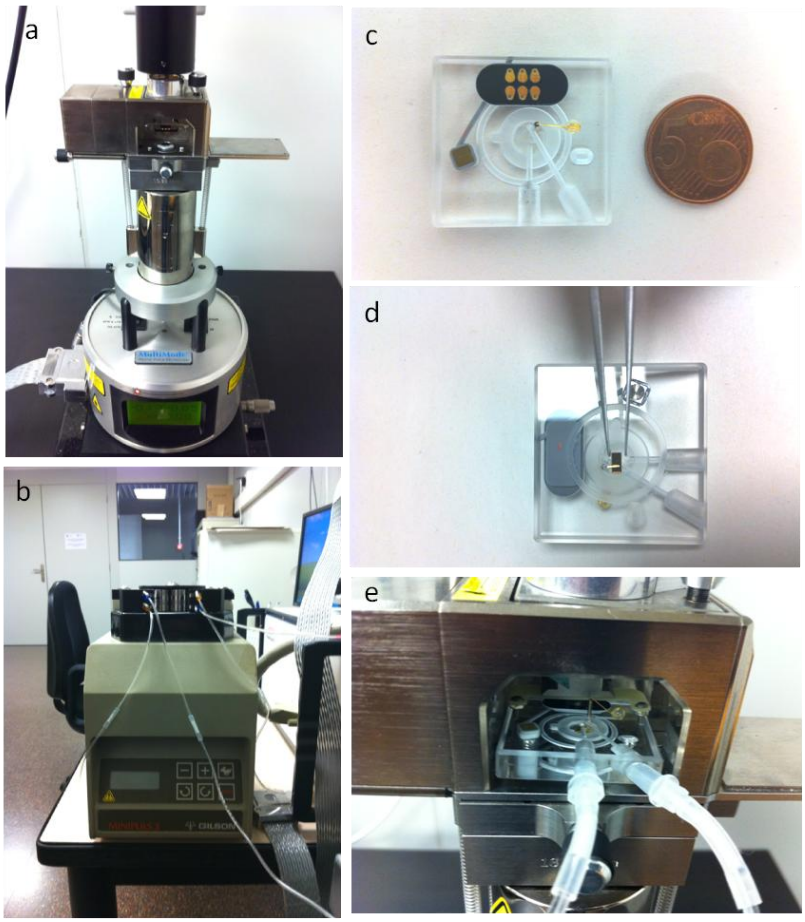

Figure 25 (a) General view of the Multimode AFM. (b) Peristaltic pump. (c) Fluid cell. (d) Tip being loaded in the fluid cell. (e) Fluid cell mounted in the AFM.

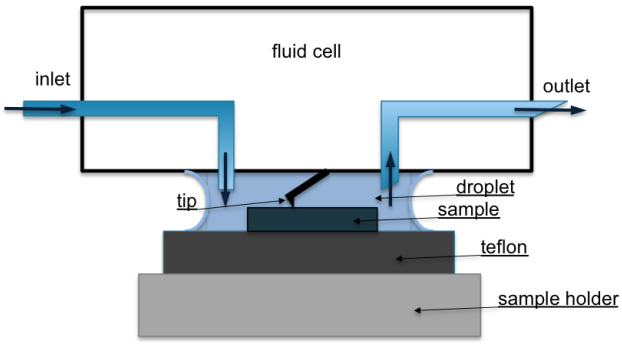

Figure 26 Scheme of the liquid cell.

3.3 Experimental

In the electron beam evaporation chamber, at a pressure of around $3.0x10^{-6}$ mbar, the e-beam started to bombard the sample spirally to avoid punctual consumption of the material and reaching the crucible, until it starts to evaporate according to changes on the quartz deposition controller and pressure decreasing. At this point the gases evacuate but not reach the silicon wafers, as the shutter was kept closed.

When the pressure stabilizes a continuous flux of 4 sccm of a mix of 50% oxygen and 50% argon was inserted in the chamber to compensate for a possible loss of oxygen. Vacuum decreases and the power was increased slowly to keep the temperature uniform in the entire powder sample, as they are not conductive.

When the pressure inside the chamber stabilizes the shuttle is open for the deposition of the evaporated material onto the silicon wafers. As soon as the required thickness was achieved (according to the quartz crystal controller) the process was stopped, the system cooled down and returned to the atmospheric pressure.

The temperature in the silicon wafers was monitored and shows to be constant room temperature during all the process; however it is not possible to confirm the temperature achieved in the bulk sample during the evaporation.

Samples were stored at nitrogen environment and desiccator to minimize their carbonation and hydration. The parameters used for each evaporation are presented in Table 2.

Table 2 Parameters of each evaporation.

Sample	Crucible	Pressure (mbar)	Power (%)	I (Amp)	Voltage (Kv)	Vel_o (Å/s)
C_3S	Graphite	$3.6\text{-}3.7x10^{-4}$	3-6	0.016-0.030	7.37-7.40	0.4-1.2
C_2S	Graphite	$3.6\text{-}3.8x10^{-4}$	6-10	0.022-0.050	7.30-7.42	1.1-2.5
C_3A	Graphite	$3.6x10^{-4}$	8-9	0.030-0.037	7.28-7.33	1-2.4
C_4AF	Boron nitride	$3.8\text{-}4.2x10^{-4}$	6-11	0.018-0.056	7.26-7.32	0.1-4

Each sample behaves differently when bombarded with the electron beam: in both C_3S and C_2S the powder sublimate and do not liquefy. The e-beam spot needs to be moved several times during the evaporation to avoid the formation of holes and the beam to reach the crucible even when using spiral beam mode.

In the evaporation of C_3A the powder seems to liquefy and medium-high intensities cause bursts. The e-beam spot needs to be moved several times during the evaporation mainly to incorporate the material from the borders avoiding the bursts. The same happens with the C_4AF but the bursts are stronger. It does not evaporate when the graphite crucible was used, and it forms a ball of liquefied material that bursts violently. For this reason different crucibles were tested. It was shown that with a boron nitride crucible it behaves better, allowing evaporation at low intensities even at low rates. The appearance of each sample after the evaporation is shown in Figure 27.

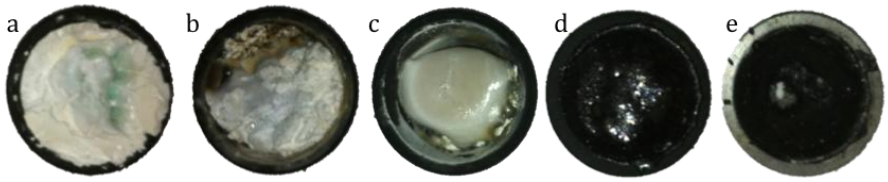

Figure 27 Appearance of each sample after the evaporation. (a) C_3S in graphite crucible. (b) C_2S in graphite crucible. (c) C_3A in graphite crucible. (d) C_4AF in graphite crucible. (e) C_4AF in boron nitride crucible.

Thicknesses of the evaporated samples were measured using a mechanical profilometer Veeco Dektak 150 by measuring the step between the areas with and without material deposited on the silicon wafer (Figure 28). The thickness of each sample are described in Table 3.

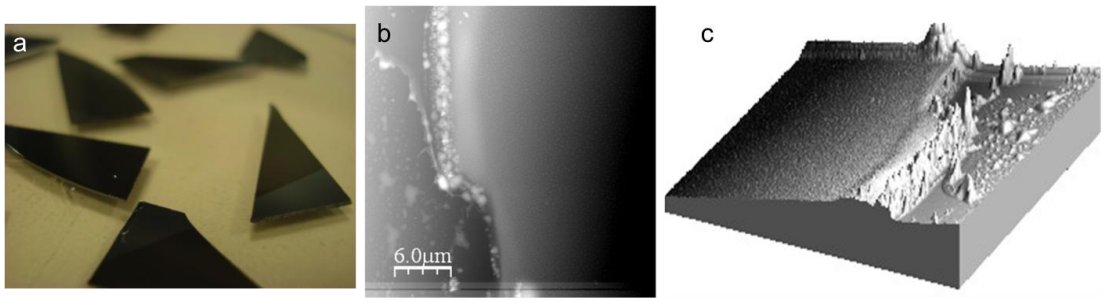

Figure 28 Step between the deposited C_3S thin film and the silicon wafer (a) and its image taken by atomic force microscopy (b, c).

The thicknesses measured are not far from the estimations of the quartz crystal controller during the evaporations as it is a matter of adjusting correctly the parameters on the equipment for the correct estimation.

Table 3 Thicknesses of the thin films.

Sample	Estimated thickness (nm)	Measured thickness (nm)
C_3S	270	280
C_2S	200	200
C_3A	180	200
C_4AF	50	60

For the XPS analysis the bulk material was pressed into pellets and samples were fixed onto holders with a copper tape. A general scan was repeated three times. Additionally, specific scans with high resolution were performed for elements of interest, such as calcium, silicon, carbon, oxygen, iron, aluminum and some other elements that could be identified in the general scan. Data were extracted from the spectra via peak fitting using CasaXPS™ software. A Shirley background was assumed in all cases. Spectra were corrected for charging effects using the adventitious carbon peak at 284.8 eV. The details of the spectral lines recorded are described below (Table 4). Passing energy is equal to 5 eV and number of scans is equal to 3 for all patterns.

Table 4 Details of spectral lines recorded.

Region	Start energy (eV)	End energy (eV)	Dwell time (ms)
Wide	0	1200	0.25
C 1s	275	295	1
O 1s	525	540	0.5
Ca 2p	339	359	1
Si 2p	94	114	1
Si 2s	143	163	1
Al 2s	108	128	1
Al 2p	65	85	1
Fe 2p	700	740	1
Mn 2p	40	60	1

3.4 Results

3.4.1 C_3S

The similarity between the XRD patterns of the bulk material and the thin film (Figure 29) leads to believe that the evaporated material maintains the bulk mineralogical composition. Even with the lower signal concerning to the thickness of the film and the noise observed, the presence of the most intense peaks of C_3S (2θ=32.07º for 100%, 34.29º for 90% and 32.32º for 70% intensity) are noticed as a broad peak in the pattern. Bulk material also presents less intense diffraction peaks of portlandite at 2θ=28.60º, 34.10º and 47.10º showing that it is partially hydrated.

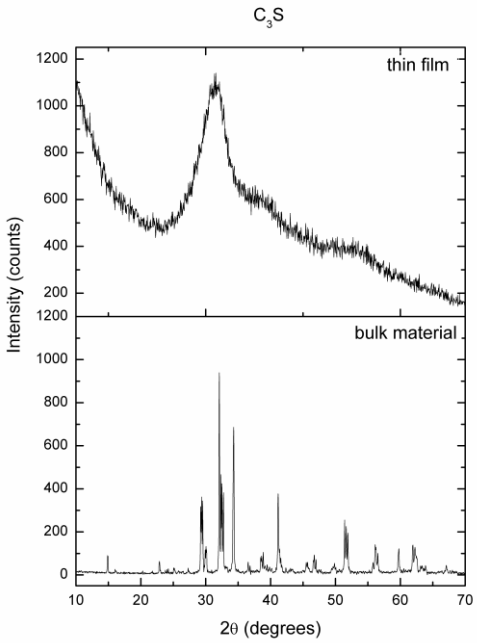

Figure 29 C_3S powder and thin film analysis with XRD and GAXRD, respectively.

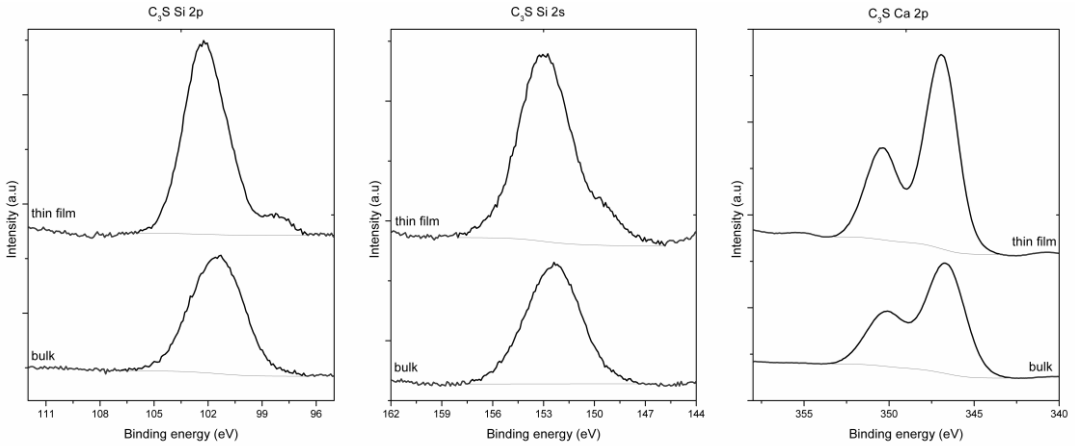

Figure 30 XPS spectra of the C_3S powder material and thin film, from left to right: Si 2p, Si 2s and Ca 2p peaks.

On the other hand the comparison between XPS patterns from the bulk material and the thin film shows that the elements present the same elemental state and no changes are noticed, except for the presence of a peak related to metallic silicon on the thin film (around 98 eV), which is associated to the substrate and appears due to the porosity of the layer despite of its thickness (Figure 30).

Besides that the Ca/Si ratio was measured by quantification methods using peak fitting. The ratio was found to be around 3, confirming that the stoichiometry of the thin film is the same as the powder material.

3.4.2 β-C_2S

As observed in C_3S, C_2S presents a strong match between the bulk material and the thin film XRD patterns (Figure 31). The same lower signal and high noise are observed but the presence of the most intense peaks of C_2S (31.98º for 100%, 32.37º for 90% and 40.54º for 55% intensity) are coincident with the broad peak in the thin film spectrum proving that the evaporated material keeps the bulk mineralogical composition. Even the amorphous peak at low degrees is observed in both spectra.

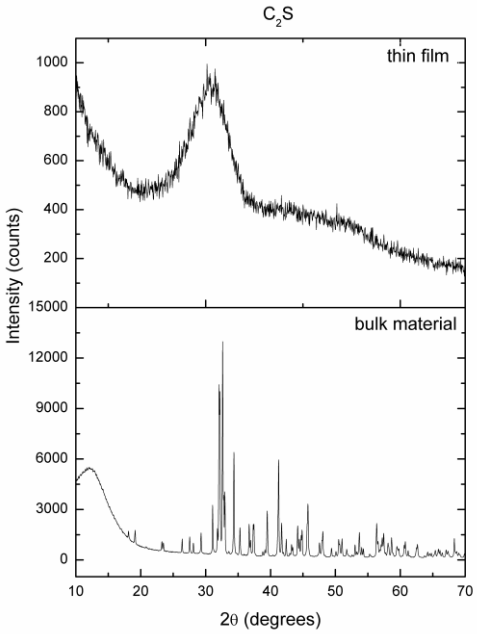

Figure 31 C_2S powder and thin film analysis with XRD and GAXRD, respectively.

Equally, the evaporated C_2S is comparable to the bulk material when observing the chemical composition, with the peaks located at the same binding energies on XPS spectra (Figure 32). The metallic silicon peak from the substrate is less evident, describing a less porous layer; however a peak deconvolution confirms its presence. The deconvolution also confirms the stoichiometry of the evaporated film, which keeps a Ca/Si ratio of around 2.

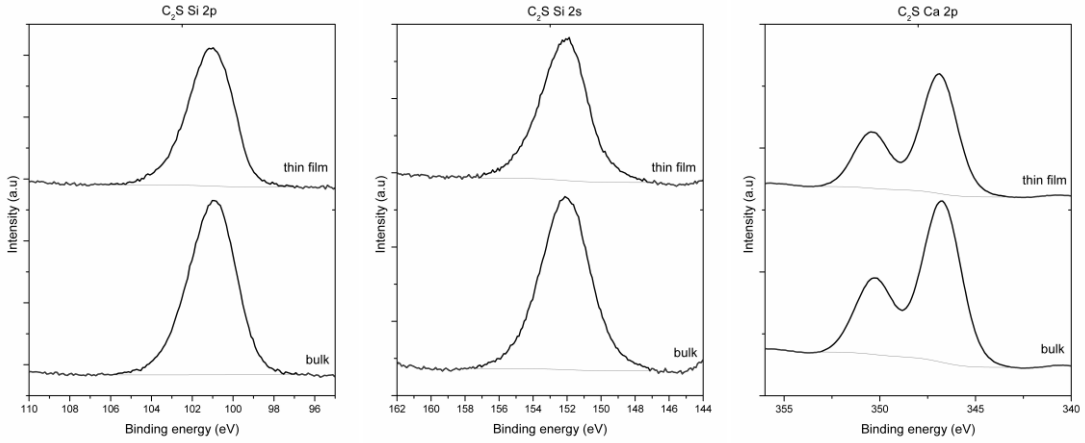

Figure 32 XPS spectra of the powder C_2S and thin film, from left to right: Si 2p, Si 2s and Ca 2p peaks.

3.4.3 C_3A

When compared to the previous samples the C_3A thin film presents more clear peaks, less noise and more intensity on the GAXRD spectrum. This is due to the bigger sample used for the test that provides bigger area for analysis. However the peaks are not coincident with the bulk material (most intense at 33.17º for 100%, 47.63º for 30% and 59.27º for 24% intensity), indicating changes on the mineralogical composition (Figure 33).

This assumption is confirmed when analyzing the XPS spectra which show that the calcium is deposited in the same chemical state as in the bulk material but the aluminum peak does not appear in the thin film spectra meaning that it does not recondense on the substrate (Figure 34). This may be due to differential evaporations on the elements forming the C_3A. That is, the thin film is not composed of C_3A but of any other material.

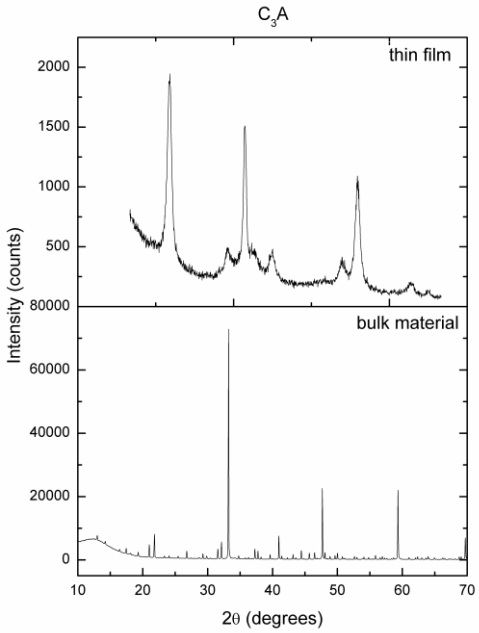

Figure 33 C_3A powder and thin film analysis with XRD and GAXRD, respectively.

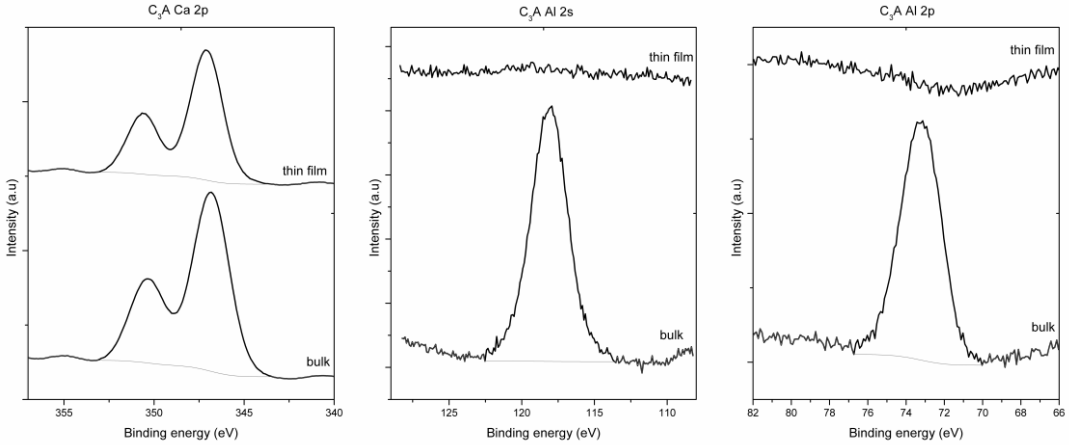

Figure 34 XPS spectra of the powder C_3A and thin film, from left to right: Ca 2p, Al 2s and Al 2p peaks.

3.4.4 C_4AF

The behavior of C_4AF evaporated material similar to the C_3A. In this case the GAXRD spectrum is not conclusive as the most intense peaks of C_4AF are coincident in both bulk material and thin film (33.51º and 35.45º for 100%, 65.86º for 70% and 59.05º for 65% intensity) (Figure 35).

However when analyzing the XPS spectra, even with the iron peaks being very similar to the bulk material concerning to the peak position, the calcium peaks are shifted to higher binding energies.

This behavior indicates that the evaporated calcium has a different chemical coordination state than the bulk material. This is expected, as the aluminum is not detected on the surface of the thin film, meaning that it did not evaporate from the bulk material or not recondensed on the surface, letting calcium to connect with another element in a different manner (Figure 36).

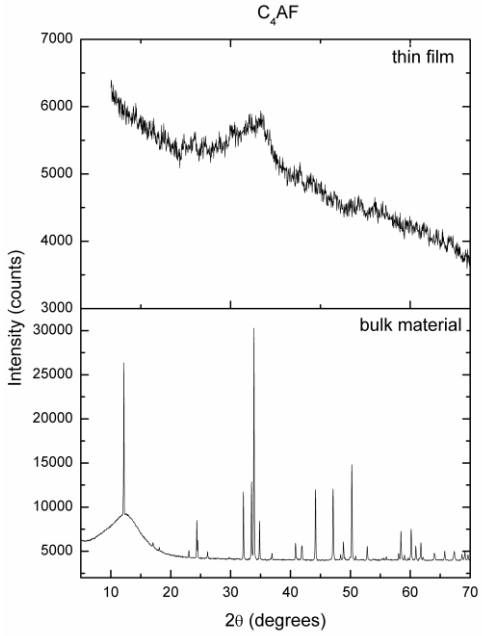

Figure 35 C_4AF powder and thin film analysis with XRD and GAXRD, respectively.

For this reason both C_3A and C_4AF samples are discarded and are no longer applied in the further investigation on this thesis.

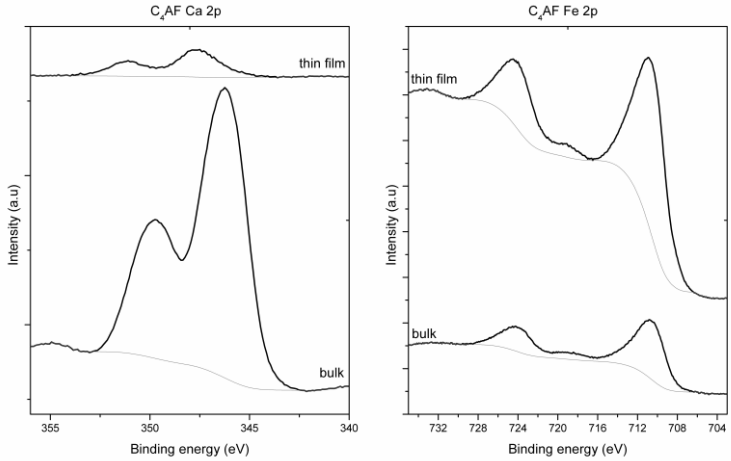

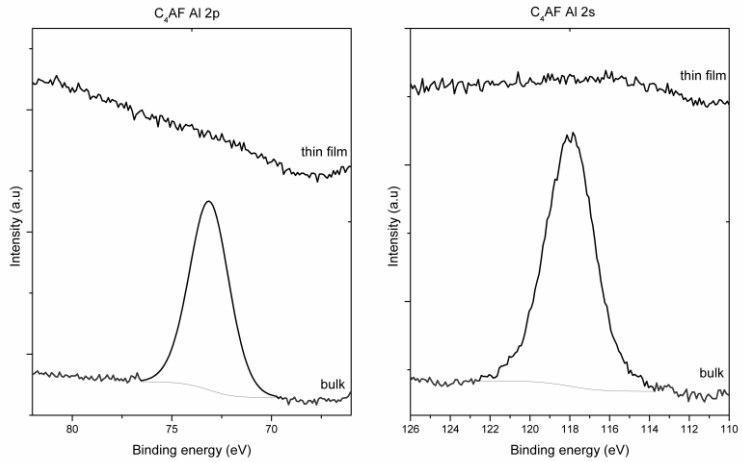

Figure 36 XPS spectra of the powder C_4AF and thin film. Upper line: Ca 2p (left) and Fe 2p (right) peaks. Lower line: Al 2p (left) and Al 2s (right) peaks.

3.5 Additional syntheses

Based on the successful synthesis of C_3S and C_2S, evaporations were repeated several times in order to produce specimens with different thickness for different applications. The same conditions were used for all the steps.

Additionally to the silicon wafers, silicon nitride windows were used as substrate for synthesizing samples for experiments on the Scanning transmission X-ray microscope. The different thickness of the samples on each substrate are summarized below and detailed in each experiment in the following chapters.

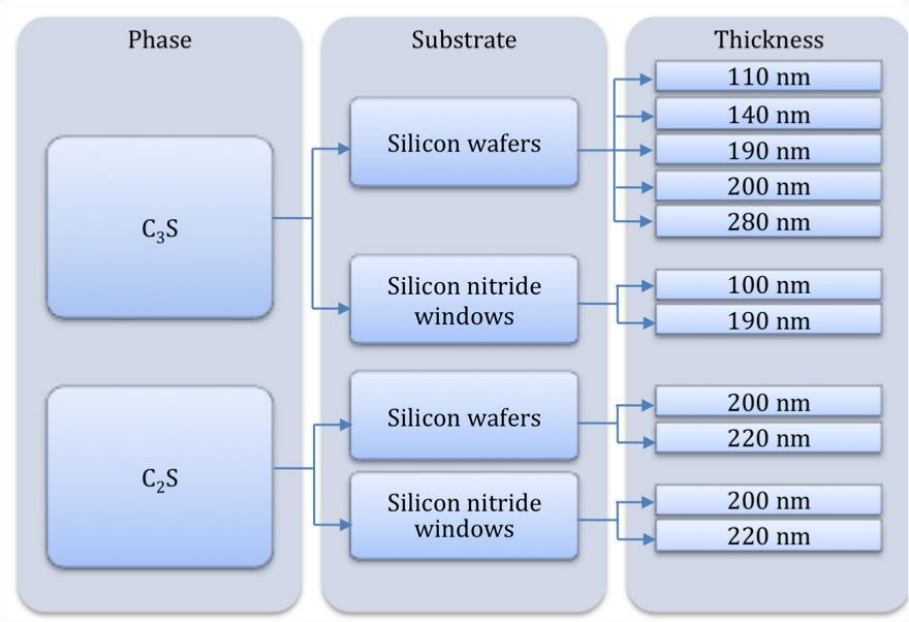

Figure 37 Summary of thin films used in this research.

3.6 Summary

Electron beam evaporation can be considered as a suitable technique for producing thin films of tricalcium and β-dicalcium silicate as when used in different conditions it provides reproducible samples that keep the same chemical and mineralogical composition from the bulk material, as confirmed by GAXRD and XPS studies.

On the other hand aluminum seems not to evaporate (or not recondense on the surface) as the other components of the clinker phases. This is clear when analyzing the XPS spectra of the thin films where no peaks on the binding energies related to aluminum are identified. This may be due to differential evaporation of the Aluminum related to the other phases. The high temperature achieved during the process (which cannot be measured) is a reasonable factor in the behavior of the material. That is believed that other evaporation techniques which do not implies high temperatures can be suitable for the synthesis of thin films of phases containing Aluminum.

GAXRD is suitable and very useful tool for the studies of thin films and presents better results when using bigger detector apertures, possible with larger samples, when the signal from the sample is more intense.

Regarding the XPS analysis all the C_3S and β-C_2S samples present coincident peak positions, peak distances and peak widths when compared to the bulk material, as well as keep the Ca/Si ratio very close to the original material, proving that they have the same chemical composition.

3.7 References

[1] S. Garrault, E. Finot, E. Lesniewska, A. Nonat. Study of C-S-H growth on C_3S surface during its early hydration. Materials and Structures 38 (2005) 435-442.

[2] L. D. Mitchell, M. Prica, J. D. Birchall. Aspects of Portland cement hydration studied using atomic force microscopy. Journal of Materials Science 31 (1996) 4207-4212.

[3] S. Gaufinet, E. Finot, A. Nonat. Experimental study and simulation of C-S-H nucleation and growth. Materials and Structures 38 (1997) 435-442.

[4] P. Mondal, S. P. Shah, L. Marks. A reliable technique to determine the local mechanical properties at the nanoscale of cementitious materials. Cement and Concrete Research 37 (2007) 1440-1444.

[5] G. Lomboy, S. Sundararajan, K. Wang, S. Subramaniam. A test method for determining adhesion forces and Hamaker constants of cementitious materials using atomic force microscopy. Cement and Concrete Research 41 (2011) 1157-1166.

[6] M. Regourd, J. Thomassin, P. Baillif, J. Touray. Study of early hydration of Ca_3SiO_5 by X-ray photoelectron spectrometry. Cement and Concrete Research 10 (1980) 223-230.

[7] L. Black, A. Stumm, K. Garbev, P. Stemmermann, K.R. Hallam, G.C. Allen, X-Ray photoelectron spectroscopy of the cement clinker phases tricalcium silicate and β-dicalcium silicate, Cement and Concrete Research 33 (2003) 1561-1565.

[8] J. Ha, S. Chae, K. W. Chou, T. Tyliszczak, P. J. M. Monteiro. Effect of polymers on the nanostructure and on the carbonation of calcium silicate hydrates: a scanning transmission X-ray microscopy study. Journal of materials science 47 (2012) 976-989.

[9] J. Ha, S. Chae, K. W. Chou, T. Tyliszczak, P. J. M. Monteiro. Scanning transmission X-ray microscopic study of carbonated calcium silicate hydrate. Transportation Research Record 2142 (2010) 83-88.

[10] M. C. Juenger, V. H. Lamour, P. J. M. Monteiro, E. M. Gartner, G. P. Denbeaux. Direct observation of cement hydration by soft X-ray transmission microscopy. Journal of Materials Science Letters 22 (2003) 1335-1337.

[11] I. Richardson. The nature of C-S-H in hardened cements. Cement and Concrete Research 29 (1999) 1131-1147.

[12] I. Richardson. The calcium silicate hydrates. Cement and Concrete Research 38 (2007) 137-158.

[13] V. M. Mecea. From Quartz Crystal Microbalance to Fundamental Principles of Mass Measurements. Analytical Letters 38 (2005) 753–767.

4 Aging and dissolution of C_3S thin films

C_3S hydration happens over a dissolution-precipitation process, as discussed in Chapter 1, by the formation of etch pits and precipitation of C-S-H [1].

XPS has been used in many researches for characterizing different silicate structures related to cement, mainly following changes in elemental composition during hydration or distinguishing different minerals. Okada et al [2] present detailed information on the photoelectron spectra of several silicate minerals relating this to the extent of silicate tetrahedral polymerization. Black et al [3] reported the effects of hydration and carbonation on the spectra for alite and belite in order to avoid erroneous results.

This chapter presents a study of aging effects on C_3S thin films as well as their dissolution. Specimens were hydrated at different times and the changes on their chemical and mineralogical composition followed by XPS and grazing angle X-ray diffraction, while the surface morphological changes were followed by atomic force microscopy.

4.1 Experimental

In order to verify the effect of aging on the samples, even when kept in a desiccator, C_3S thin films with 140 nm thickness were analyzed twice on the XPS, firstly right after sample preparation (fresh) and, secondly, after storage in desiccator for six months (aged). Complementarily, the samples were analyzed at different ages using the GAXRD.

For the dissolution experiments the thin films were inserted in a milli-Q water bath at different time intervals (10, 20, 40, 50 and 60 minutes), and after transferred to an isopropyl alcohol bath for two minutes in order to stop the hydration process. Then, they were dried at 50°C for 4 hours and stored in a desiccator.

For the XPS analyses, a general scan was repeated three times and specific scans with high resolution were performed for carbon, oxygen, calcium and silicon. Data were extracted from the spectra via peak fitting using CasaXPS™ software. The Shirley background was assumed in all cases. Spectra were corrected for charging effects using the adventitious carbon peak[2] located at 284.8 eV, except when mentioned. The details of the spectral lines recorded are described below. Passing energy is 5 eV.

Table 5 Details of spectral lines recorded.

Region	Start energy (eV)	End energy (eV)	Dwell time (ms)
Wide	0	1100	0.25
C 1s	274	294	1
O 1s	522	542	0.5
Ca 2p	339	359	1
Si 2p	94	114	1
Si 2s	144	164	1

Finally an atomic force microscope (AFM) was used to measure the topography of the samples in order to identify changes in roughness and surface area variations. It requires very flat surfaces (typically with a maximum roughness of a few hundred nanometers), which have been achieved using the electron beam

[2] Adventitious carbon peak appears in all air exposed samples and for this reason is normally used as a charging reference to correct shifted energies obtained into meaningful binding energies.

evaporation mentioned above. AFM was settled in contact mode using a tip DNP-S10 with k=0.58 N/m.

4.2 Results

4.2.1 Aging effects on C_3S thin films

Comparison between fresh and aged samples shows signals of silicon polymerization due to the formation of C-S-H, related to the shift on the silicon peak to higher intensities (Table 6 and Figure 38). In addition a broadening on the carbon peak is noticed and also related to the C-S-H formation.

Table 6 Binding energies and peak widths (FWHM) for fresh and aged C_3S sample.

	Fresh		Aged	
	BE	FWHM	BE	FWHM
Ca 2p $_{3/2}$	347.4	2.0	347.5	2.0
Ca 2p $_{1/2}$	351.0	2.0	351.1	2.0
	352.7	3.9	353.3	2.9
Si 2p $_{3/2}$	101.1	2.2	102.5	2.1
Si 2p $_{1/2}$	-	-	99.9	2.3
Si 2s	153.0	2.9	153.8	2.1
	149.7	2.6	152.8	4.8
O 1s	531.8	2.7	532.0	2.7
	529.2	1.3	-	-
δ Ca 2p - Si 2p	245.5		245.0	

The GAXRD results show that the most intense peaks of calcite appear to be increasing with time at 29.4° and 39.4°, reflecting sample's hydration and carbonation, as in fresh samples very low signal related to these peaks are observed. On the other hand, a broad peak at around 31° shows the presence of a glassy material that can be C_3S (Figure 39).

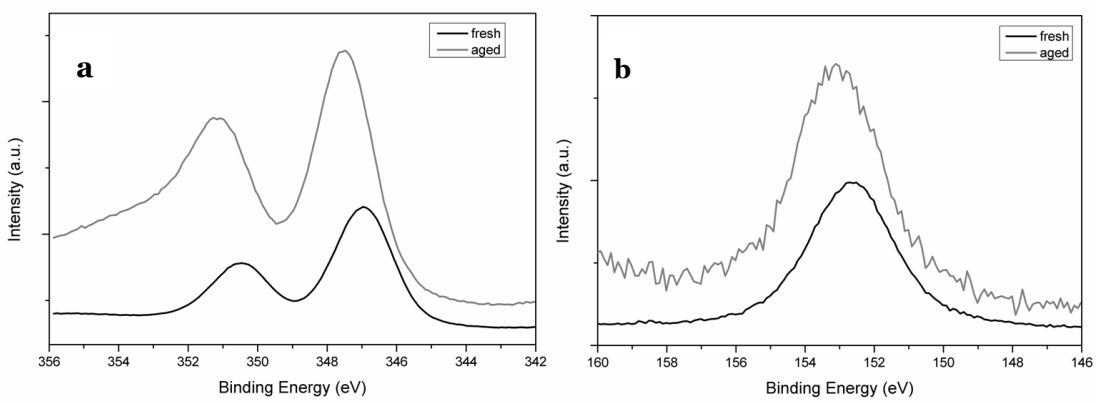

Figure 38 Comparison between fresh and aged C_3S samples: Ca 2p (a) and Si 2s (b).

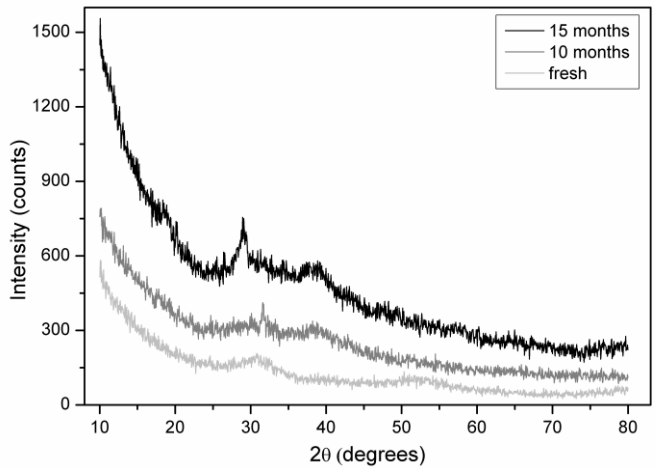

Figure 39 Comparison of GAXRD spectra for samples at different ages.

4.2.2 Dissolution of C_3S thin films

The Si 2p peak shows that during the process the C_3S has been partially dissolved, as the intensity of the metallic silicon peak at 99.15 eV, related to the substrate, increases. For this reason this peak was used for calibrating these patterns (Figure 40). Results for each step are presented in Table 7.

Besides the increasing on the metallic silicon peak the samples exposure to water resulted in a shift on the silicon peak to higher binding energies, associated to the polymerization of the isolated silicate tetrahedral (Figure 41). The same behavior was described previously by other authors [3, 4]. That is, at the same time the sample is being hydrated and C-S-H is forming, it is being dissolved and the thickness of the layer is decreasing.

Table 7 Binding energies and peak widths (FWHM) of the samples submitted to ex situ hydration.

Time (min)		Ca 2p 3/2	Ca 2p ½		Si 2p 1/2	Si 2p 3/2	Si 2s		O 1s	δ Ca 2p - Si 2p	δ Si 2p 1/2 - Si 2p 3/2
0	BE	346.7	350.2	352.2	101.6	99.2	152.8	150.0	531.2	245.1	2.4
	FWHM	2.0	2.0	3.2	2.0	1.7	2.8	2.1	2.7		
10	BE	346.7	350.2	352.0	101.7	99.2	152.7	149.7	531.0	245.1	2.5
	FWHM	1.9	2.0	3.6	2.1	1.4	2.7	1.7	2.9		
20	BE	346.6	350.1	351.9	101.8	99.1	152.7	150.0	530.7	244.8	2.7
	FWHM	1.9	2.0	3.6	2.1	1.4	2.8	1.9	2.9		
40	BE	346.6	350.1	352.1	101.6	99.1	152.7	150.1	531.0	245.0	2.6
	FWHM	2.0	2.1	4.1	2.5	1.3	3.3	1.8	3.1		
50	BE	346.8	350.3	352.3	102.0	99.1	153.0	150.2	530.8	244.8	2.9
	FWHM	2.1	2.1	4.0	2.3	1.3	3.0	1.7	3.1		
60	BE	346.9	350.4	352.3	102.3	99.1	153.2	150.4	531.0	244.6	3.1
	FWHM	2.2	2.2	3.8	2.2	1.4	3.0	1.8	3.1		

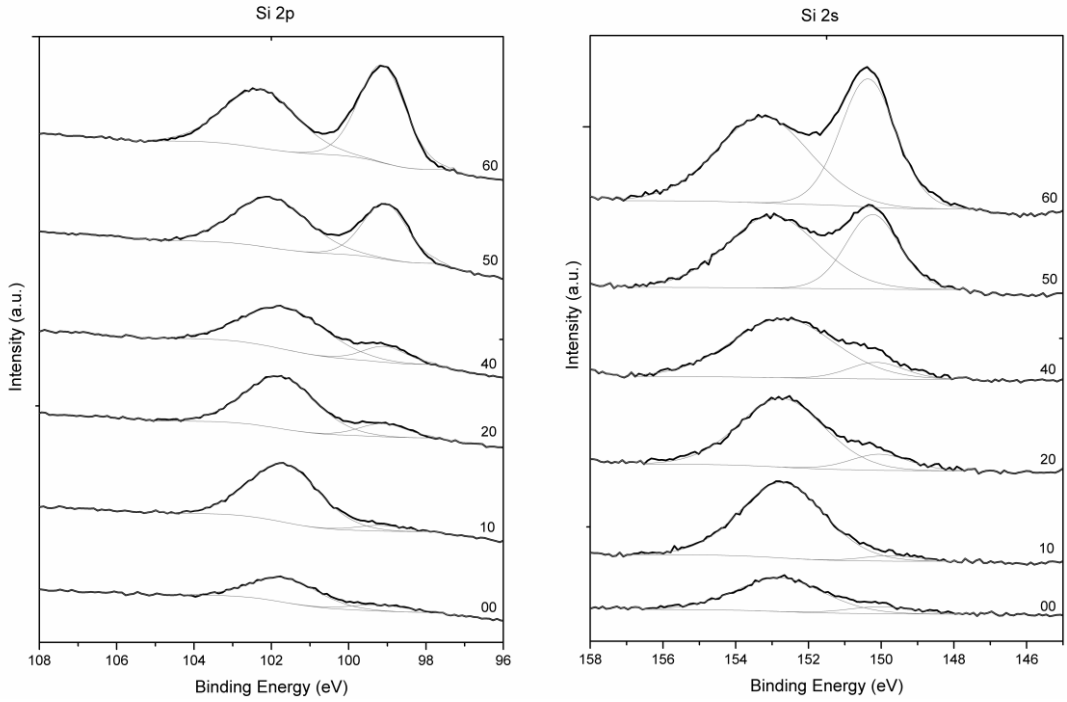

Figure 40 Si spectra of dissolved samples at different times.

The Si 2s peaks present the same behavior as the Si 2p, increasing the intensity of the 150 eV peak, associated to the metallic silicon of the substrate, while the 153 eV peak, related to the silicates, shifts to higher binding energies representing the polymerization of the silicon atoms, interrelated to the formation of hydrated products.

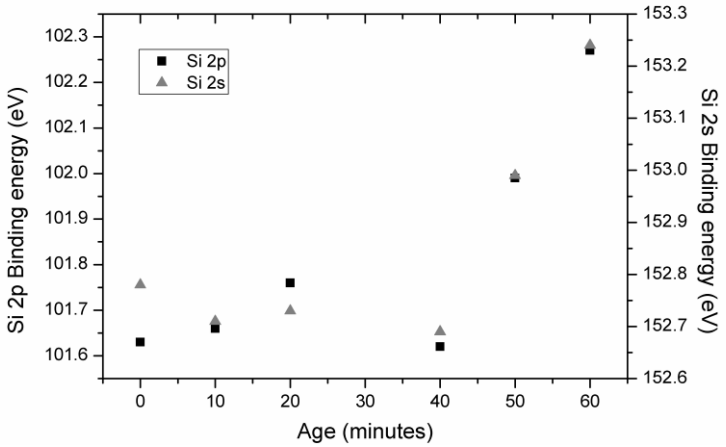

Figure 41 Si peak position over time.

In addition a broadening on the silicon peak during the hydration is observed, and both changes can be related to the disordering on the silicate structure due to the formation of C-S-H.

Even with no significant changes on the Ca 2p binding energies an enlargement on the Ca $2p_{1/2}$ peak is noticed during the hydration, mainly at its secondary peak at around 352.2 eV. This may be due to the C-S-H formation as the calcium silicates have slight higher energies than the calcium carbonates (Figure 42).

The separation between the two peaks $\delta_{Ca\ 2p\ -\ Si\ 2p}$ decreases over time in the same way as reported by Black et al [4], describing the C-S-H formation. This parameter provides information about hydration as the silicate polymerization causes a decrease on these peaks distance, avoiding errors due to charge correction [5, 6].

In order to quantitatively assess the chemical changes during hydration, a deconvolution of the Ca $2p_{1/2}$ and Ca $2p_{3/2}$ peaks has been carried out in behalf of separate the contributions from carbonates and silicates. Calcium silicates are known to have Ca 2p binding energies slightly higher than those of calcium carbonates and for this reason the peaks with higher binding energies are used here for calculations. The silicon peak related to the substrate is ignored, considering just the peak related to the silicates. Accordingly, when applying these corrections the Ca/Si ratio drops from about 1.06 to 0.58 as hydration progress (Figure 43). Although contributions from portandite and/or unhydrated C_3S cannot be rejected, such low Ca/Si values evidence the presence of C-S-H.

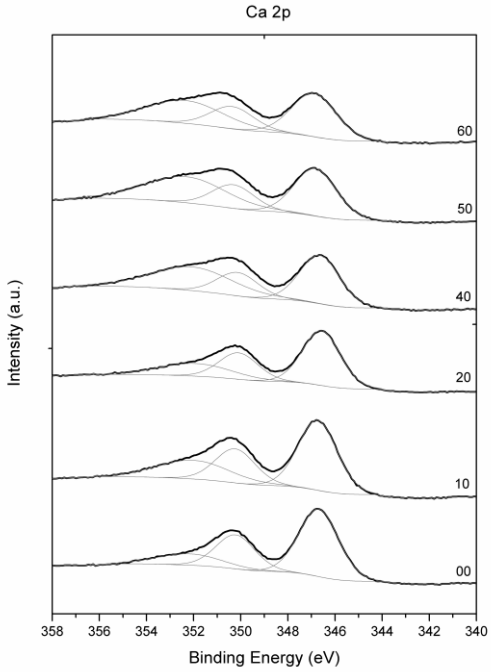

Figure 42 Ca 2p spectra of samples in dissolution at different times.

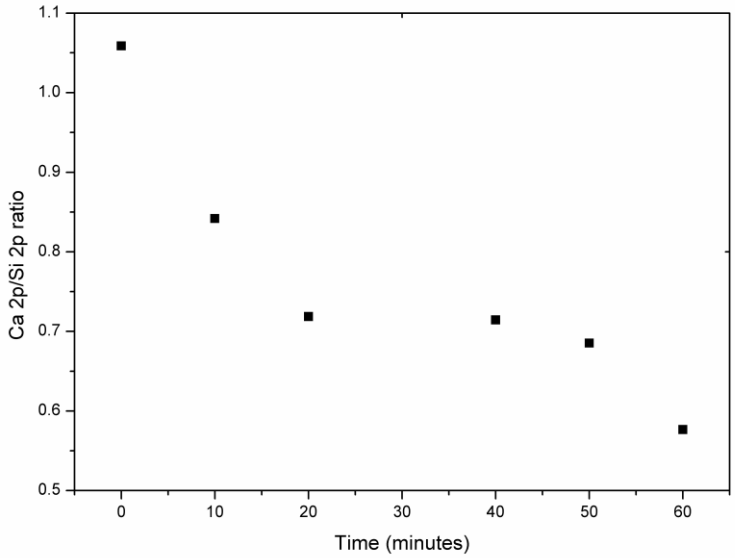

Figure 43 Ca/Si ratio development during the hydration time.

Furthermore on the C-S-H phases there is a strong influence of the Ca/Si ratio on the Si 2p binding energy: the higher ratio leads to lower energies [2, 3, 7]. Even the first researches using XPS for cementitious materials related that the Ca 2p/Si 2p ratio must be lower in hydrated samples than in anhydrous C_3S. However considering the Si 2p binding energy and peak shape the hydrated particles show significant

changes in a very short time with the hydration, describing variations on the Si 2p binding energy from five seconds on [5].

Regourd et al [5] relate the formation of a primary hydrate with Ca/Si ratio <<3 on the first minute of hydration as the C_3S grain surface is not in equilibrium and is a site of continuous exchange.

The GAXRD analysis of the same samples (Figure 44) shows an initial presence of calcite around 39.47º and a broadening on the region around 28-30º, where the portlandite, calcite and C-S-H peaks can be found, as the most intense peaks of the last two appear at these reflections. However the most intense peak of portlandite does not appear in the patterns, evidencing that it is not present on the samples. During the hydration a broad peak at 18.65º is formed that can be related to C-S-H. The same component appears at around 31º but its increasing is covered by the noise and the other close peak. Intense peaks of calcite are also increasing with hydration at 29.4º and 39.03º. It is clear that hydration process happens through the formation of C-S-H and calcite during the progression. Labels are related to the time in contact to water, in minutes.

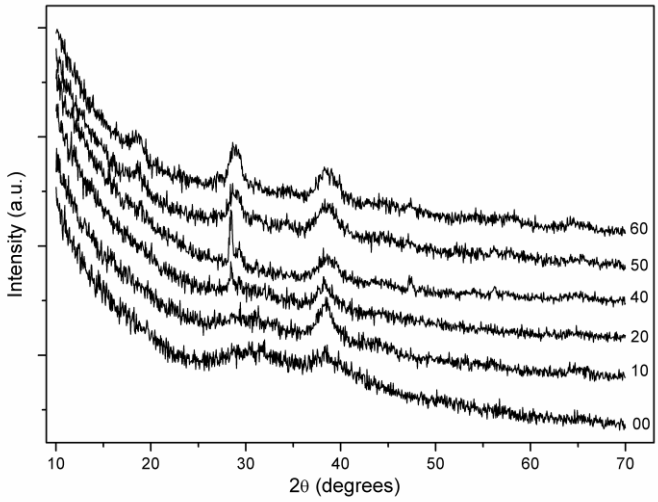

Figure 44 XRD patterns for the samples subjected to dissolution.

Finally an AFM was used in contact mode to follow the changes in the surface's topography. The images of the C_3S thin films after successive hydration show the initial flat surface with the presence of a few particles with 100-200nm, which appear to be calcite crystals formed due to the pre-hydration of the samples by the contact with the atmosphere. With time of hydration these particles are dissolved

and the formation of aggregated nanoparticles of C-S-H with about 60 x 30 nm^2 and 5 nm thick is identified, starting from 10 minutes of hydration and appear to increase with time. At 60 minutes of hydration the surface is completely covered and just a few porous are observed (dark parts), which can be related to dissolved parts of the sample. The same particles are observed by Nonat [8] in a hydrated cement paste in contact with a calcite single crystal and by Garrault et al [9] in an alite surface after 4 hours of hydration with lime saturated solution.

Comparison among the AFM images and the data from XPS and GAXRD agree in the sense that initially not so much C-S-H is formed, both in the images and on the silicon polymerization by the shifts on Si peaks and by the formation of the broad C-S-H peak in the mineralogical analysis.

Table 8 presents the roughness averages for each image. It is clear that the big particles found at the initial ages due to the pre-hydration crystals interfere in the roughness data. Besides that image at 20 minutes of hydration seems to present some artifacts that can be due to several factors and for this reason the roughness can be masked. With time of exposure, at later ages, the roughness slowly increases as a signal of the formation of hydration products and dissolution of C_3S, increasing porosity.

Table 8 Roughness of sample.

Age (minutes)	Roughness average
0	2.65
10	2.61
20	2.37
40	1.69
50	2.00
60	2.18

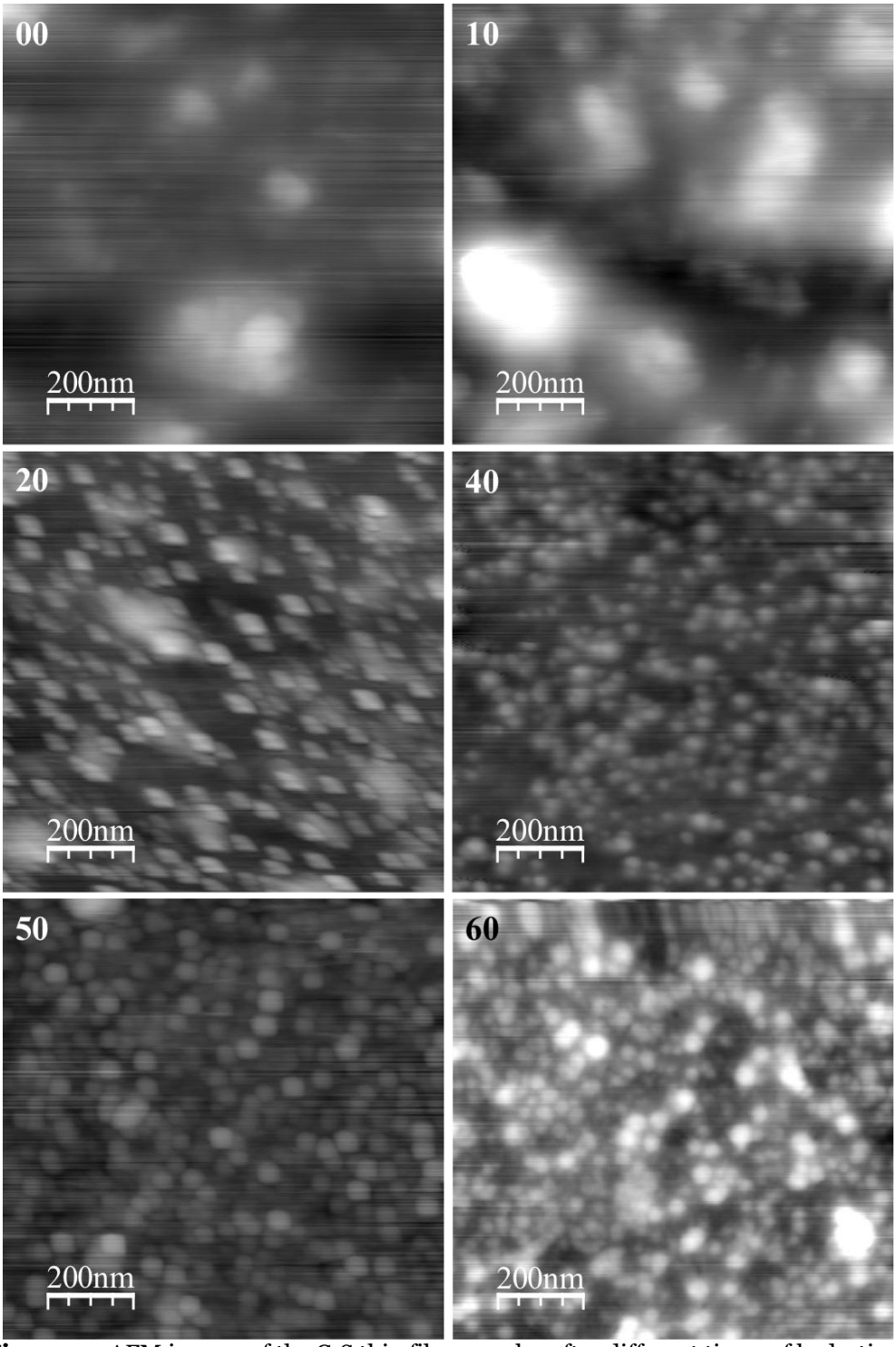

Figure 45 AFM images of the C_3S thin film samples after different times of hydration. Relative height is 25 nm.

4.3 Summary

Samples seem to react fast when in contact to the atmosphere by initial signals of carbonation and hydration on the first results.

XPS investigations show clear signs of dissolution by the increasing on the intensity of the metallic silicon peak over time. Moreover the peak related to silicates shift to higher binding energies and the distance between calcium and silicon peaks decrease as a result of the polymerization and disordering in the silicon structure due to the formation of C-S-H.

Observed broadening on the Ca 2p ½ peak at higher binding energies is associated to the C-S-H formation in addition to the calcium carbonates present.

Running the same samples with the GAXRD confirm the observations by XPS through an increase on the calcite and/or C-S-H broad peaks at around 28-30º. Calcite is present from the initial stages and during the hydration results show clear signals of C-S-H and calcite formation.

AFM observations show changes on the surface due to the formation of aggregated nanoparticles of C-S-H with about 60 x 30 nm^2 and 5 nm thick that appear to increase in time.

4.4 References

[1] P. Juilland, E. Gallucci, R. Flatt, K. Scrivener Dissolution theory applied to the induction period in alite hydration. Cement and Concrete Research 2010 (40) 831-844.

[2] K. Okada, Y. Kameshima, A. Yasumori. Chemical Shifts of Silicon X-ray Photoelectron Spectra by Polymerization Structures of Silicates. Journal of the American Ceramic Society 1998 (81) 1970-1972.

[3] L. Black, A. Stumm, K. Garbev, P. Stemmermann, K. R. Hallam, G. C. Allen X-ray photoelectron spectroscopy of the cement clinker phases tricalcium silicate and β-dicalcium silicate. Cement and Concrete Research 2003 (33) 1561-1565.

[4] L. Black, K. Garbev, P. Stemmermann, K. Hallam, G. C. Allen Characterization of crystalline C-S-H phases by X-Ray photoelectron spectroscopy (XPS). Cement and Concrete Research 2003 (33) 899-911.

[5] M. Regourd, J. Thomassin, P. Baillif, J. Touray. Study of early hydration of Ca_3SiO_5 by X-ray photoelectron spectrometry. Cement and Concrete Research 1980 (10) 223-230.

[6] L. Black, K. Garbev, G. Beuchle, P. Stemmermann, D. Schild. X-ray photoelectron spectroscopic investigation of nanocrystalline calcium silicate hydrates synthesized by reactive milling. Cement and Concrete Research 2006 (36) 1023-1031.

[7] H. Seyama, M. Soma. Bonding-state characterization of the constituent elements of silicate minerals by X-ray photoelectron spectroscopy. J. Chem. Soc., Faraday Trans. 1985 (81) 485-495.

[8] A. Nonat. The structure and stoichiometry of C-S-H. Cement and Concrete Research 2004 (34) 1521-1528.

[9] S. Garrault, E. Finot, E. Lesniewska, A. Nonat. Study of C-S-H growth on C_3S surface during its early hydration. Materials and Structures 2005 (38) 435-442.

5 Hydration of calcium silicate thin films

This chapter presents the analysis of the hydration of calcium silicate thin films. The process was followed chemically through XPS for samples hydrated with water vapor and through STXM for samples hydrated with liquid water, and morphologically through AFM for samples hydrated with a continuous water and/or a saturated lime solution flux.

5.1 Chemical changes during the hydration of Tricalcium silicate thin films

C_3S is the major clinker phase in Portland cement, and hence a very important component to fully understand and predict the development of strength and durability of concrete, the details of the hydration mechanisms of tricalcium silicate have remained elusive for decades.

The surface chemistry of early hydration of tricalcium silicate with X-ray photoelectron spectroscopy (XPS) investigations evidences that the Ca 2p/Si 2p ratio must be lower in hydrated samples than in anhydrous C_3S. The silicon binding energy and peak shape of the hydrated particles show significant changes shortly after the onset of hydration [1].

Previous investigations have proposed that growth of hydrates takes place in different spots by addition of silicate tetrahedra and development of silicate sheets incorporating calcium and hydroxyl in the interlayers [2], and that the formation of independent C-S-H nanoparticles stimulates the nucleation of new ones on their surfaces [3]. Also, atomistic simulations and modeling approaches have been developed to better understand the process [4-9], suggesting on one hand that the C-S-H density is not uniform and it decreases with distance from the alite grain surface and, on the other, that dimeric silicates are formed just after the end of the dormant period.

This section presents the results of the chemical evolution upon hydration of C_3S thin films produced by electron beam evaporation of powdered raw material. In-situ hydration of the thin films and continuous monitoring of their chemical and microstructural evolution by XPS and STXM, and focused ion beam (FIB) sectioning and imaging shed some additional light on the complex problem of the hydration mechanisms of cementitious materials.

5.1.1 Experimental

Thin films of C_3S were produced by electron beam bombardment as described previously. For the XPS studies presented here, films of about 110 nm in thickness were deposited over silicon wafers and kept in an inert N_2 atmosphere in order to minimize atmospheric pre-hydration and carbonation prior to the beginning of the hydration experiments.

Samples of the thin films were fixed in a holder with an adhesive-backed copper tape and their chemical composition was verified with the XPS system at UPC's Center for Research in Nanoengineering, explained in detail previously. Spectra were recorded with pass energy of 25 eV at 0.1 eV/step, and pressure below 10^{-9} mbar. A flood gun (0.36 eV, 0.24 mA) was used to avoid sample charging. The angle between the sample and the emission gun was settled at 15º and their distance to 30 mm. For each pattern, general scans were repeated three times and specific high-resolution scans were carried out for Ca, Si, C and O (Table 9).

After running the initial pattern, dry thin film samples were transferred individually to a reaction chamber in the same vacuum line as the XPS, thus avoiding any atmospheric contamination (Figure 22). A vaporizer with mili-pore water was

used to insert water vapor in saturated state using argon as a carrier with a flux of 20 mL/min. Prior to hydration the system was purged for 5 minutes.

Table 9 XPS analytical conditions and chemical compositions of starting material and thin films.

	XPS conditions			Composition	
Region	Start energy (eV)	End energy (eV)	Dwell time (ms)	Starting material (at.%)	Thin film (at.%)
Wide	0	1200	0.1	-	-
C 1s	275	295	0.5	22.2	20.7
O 1s	525	540	1	54.6	55.4
Ca 2p	339	359	1	18.1	17.8
Si 2s	143	163	1	5.1	6.1
Si 2p	94	114	1		
Total	-	-	-	100	100

Table 10 Experiment conditions for each stage of hydration of thin films.

Time (min)	Accumulated time (min)	Temperature (ºC)	P (H_2O) (mbar)
2	2	28.8	39.59
5	7	27.9	37.58
5	12	28.0	37.79
5	17	28.4	38.68
10	27	26.6	34.82
15	42	26.9	35.44
20	62	26.6	34.82
60	122	26.7	35.03
60	182	27.4	36.49

Spectra were treated with CasaXPS™ software. A Shirley background was assumed in all cases. Spectra were corrected for charging effects using the adventitious carbon peak at 284.8 eV.

A FIB/SEM was used for observation and selective milling of samples, both unreacted and exposed to water vapor for 182 minutes.

STXM samples were prepared by evaporating the calcium silicates over the silicon nitride windows, as explained in Chapter 3. After the evaporation samples were kept in vacuum to minimize pre-hydration and carbonation. At the time of the test specimens were fixed in the sample holder with a double-faced tape, and analyzed in dry condition.

All sample preparation was done under environmental conditions. Specimens are loaded in the experimental chamber and quickly vacuumed. Each time the energy of interest changed the sample was re-focused and image contrast measurements performed. Once elemental locations were identified, line scans and image stack were run on the areas of interest to obtain the NEXAFS spectrum. Beam damage was checked by measuring the NEXAFS spectra before and after the long image stack.

The normalization and the background subtraction for the spectra were made by dividing each sample spectrum by the spectrum of an identical free-membrane as, because of the sample preparation, there are no sample-free locations in the same membrane. The elemental maps are taken by subtracting the images from above and below the absorption energy level.

Data was analyzed with Axis 2000 software: it allows aligning image stacks and extracting NEXAFS spectra from image stack and lining scan measurements.

For the hydration experiments a drop of 0.1 μl of Milli-Q water was placed on the silicon nitride membrane window and a second membrane was placed over. The membranes were bonded with epoxy in order to avoid evaporation and leaking.

Results are strongly dependent on the thickness of the sample. For this reason a comparison among samples with different thickness (25, 100 and 190 nm) was run in order to choose the appropriate for each element (Ca, Si, C).

STXM at ALS beamline 5.3.2.2 was used to characterize calcium and carbon edges for all the samples, using an empty silicon nitride window as background (I_o). Results show that thicker samples are not the best option for analyzing these elements in C_3s thin films as the Ca spectrum show signs of saturation (Figure 46). In this case the thinner sample, with 25 nm, is the most appropriated as it provides enough signal for the analysis without saturation, while samples with 100 and 190 nm present very similar saturated intensity, above the optical density value of 2. Based on that the 25 nm samples were chosen to follow the hydration based at the calcium edge on this instrument.

That happens because the sample thickness affects directly the optical density. That is, for thicker and denser samples the material absorbs all the radiation and not enough transmission is detected, preventing the analysis.

On the other hand STXM at beamline 5.3.2.1 was used to characterize the samples silicon edge. In this case, the 100 and 190 nm samples were used. As the 25

nm sample appear to be too thin with low signal to noise ratio (Figure 46). For this reason the thicker samples were used here.

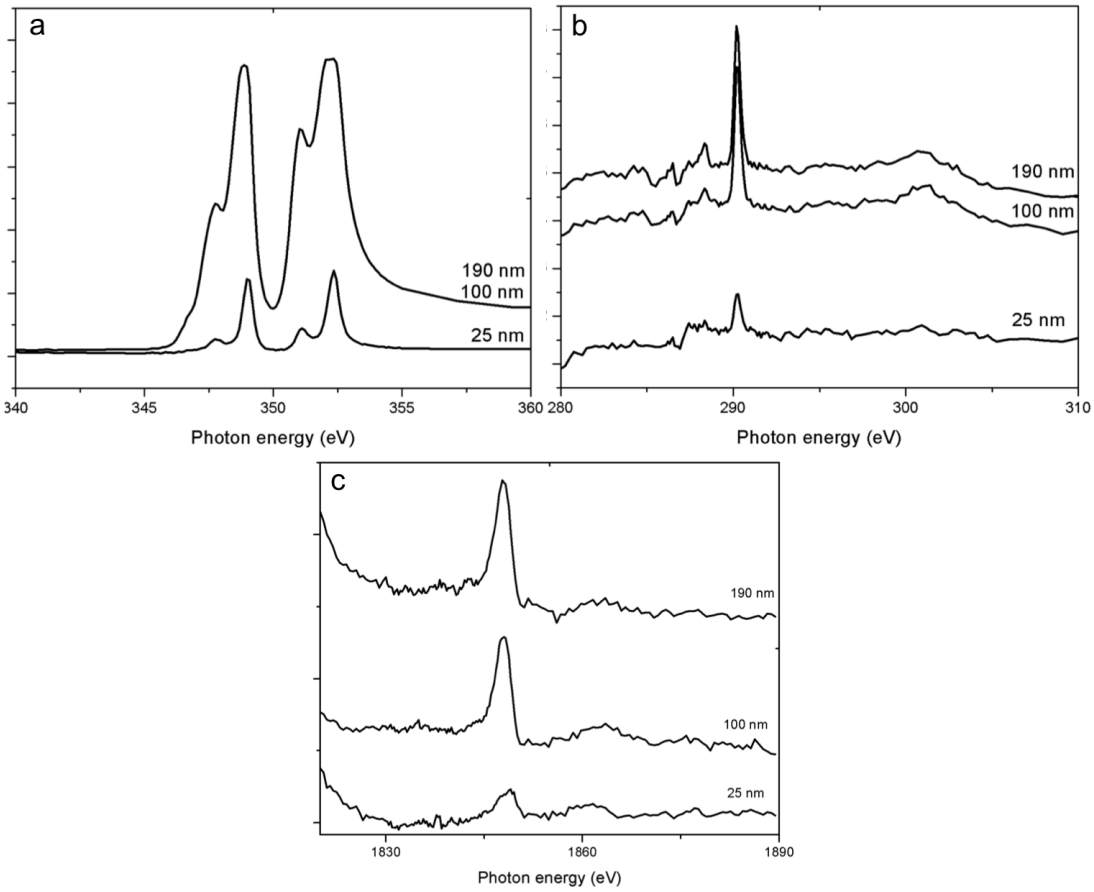

Figure 46 Comparison of C_3S samples with different thickness. (a) Ca $L_{2,3}$-edge. (b) C K-edge. (c) Si K-edge.

5.1.2 Results and discussion

5.1.2.1 XPS analysis

After 3 hours of exposure to water vapor, the characteristic energies of Si peaks present a drift to higher energies in both Si 2p (101.9 to 102.6 eV) and Si 2s (152.9 to 153.4 eV) peaks. These are positioned at lower energies than those previously reported (100.57 eV for Si 2p in fresh C_3S, [10]). The Si peaks display a shift to higher energies and slight broadening (e.g. average FWHM of 3.3 *vs.* 2.5 eV in the 152.9-153.4 and 101.9-102.6 eV ranges, respectively; Figure 47 and Table 11),

indicating the progressive disordering of the silicate structure related to C-S-H formation.

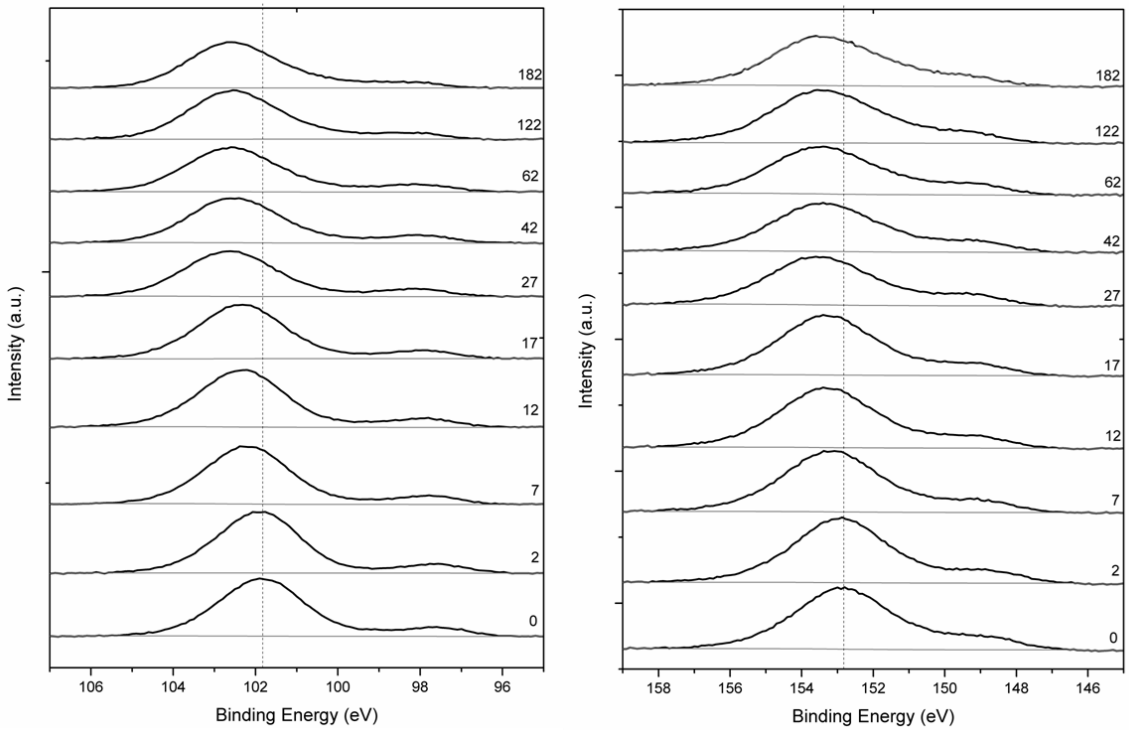

Figure 47 XPS spectra of the C_3S thin film showing the evolution of the Si 2p (left) and 2s (right) peaks during exposure to water vapor. Labels on the right indicate time of hydration in minutes.

Table 11 Evolution of binding energies and peak width (FWHM) of Si and Ca and Ca-Si peak distance during vapor hydration of C_3S.

Time (min)	Peak positon (eV)			Ca-Si distance
	Si 2p	Si 2s	Ca 2p $_{3/2}$	$\delta_{Ca\ 2p\text{-}Si\ 2p}$
0	101.9 (2.5)	152.9 (3.2)	347.1 (2.7)	245.2
2	101.9 (2.4)	152.9 (3.2)	347.2 (2.7)	245.3
7	102.2 (2.4)	153.2 (3.3)	347.3 (2.6)	245.1
12	102.4 (2.5)	153.3 (3.3)	347.4 (2.6)	245.0
17	102.4 (2.5)	153.3 (3.3)	347.3 (2.6)	244.9
27	102.6 (2.6)	153.5 (3.3)	347.6 (2.5)	245.0
42	102.5 (2.5)	153.4 (3.3)	347.4 (2.5)	244.9
62	102.6 (2.5)	153.5 (3.3)	347.5 (2.5)	244.9
122	102.6 (2.5)	153.4 (3.5)	347.2 (2.5)	244.6
182	102.6 (2.5)	153.4 (3.3)	347.2 (2.5)	244.6

The Ca binding energies show a somehow more erratic behavior, but no progressive shift has been observed, as in the case of Si, when hydration goes on (Figure 48). The Ca $2p_{3/2}$ peak is centered at 347.1 eV (Table 11) for fresh C_3S, a value slightly lower than the one previously reported by Black et al [10] (346.55 eV).

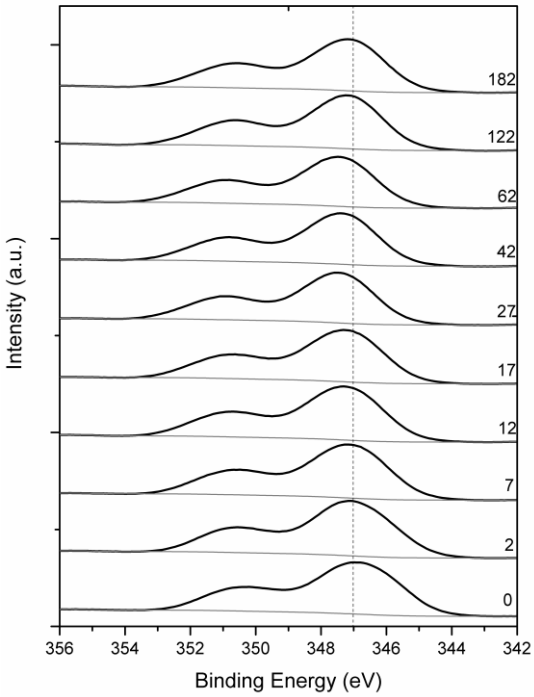

Figure 48 Calcium spectra (lower and higher energy peaks correspond, respectively, to Ca $2p_{3/2}$ and Ca $2p_{1/2}$ lines) of the C_3S thin film showing the variation of the peaks during the exposure to water vapor.

Measuring the energy separation between Ca $2p_{3/2}$ and Si 2p peaks ($\delta_{Ca2p\text{-}Si2p}$) provides information about hydration. This approach avoids errors due to charge correction [1, 11]. The calculated Ca-Si distances and their evolution with time of hydration are plotted in Figure 49. The initial values of $\delta_{Ca2p\text{-}Si2p}$ found in this work (245.3 eV) are somewhat lower than those reported by Regourd et al [1] (245.7 eV), Long et al [12] (245.95 eV) and Black et al [13] (245.99 eV). As discussed above, progressive hydration of C_3S results in a shift of the Si 2p and Si 2s peaks to higher binding energies, therefore reducing the value of the distance between the peaks of calcium and silicon. This is due to the polymerization of the isolated silicate tetrahedra upon formation of C-S-H, and/or carbonation [14], although formation of calcium carbonate is not likely to occur under the experimental conditions of this work.

Despite the slight differences in the values of the Ca $2p_{3/2}$ peaks, the reduction of the Ca-Si distance after 3 hours of hydration of C_3S found in this work ($\delta_{Ca\ 2p\ 3/2\ -\ Si\ 2p}$ = 0.6) is identical to that found by Regourd et al [1] after 4 hours. This strongly suggests that the kinetics of early C-S-H formation is not significantly altered when vapor (this work), instead of liquid water, is used.

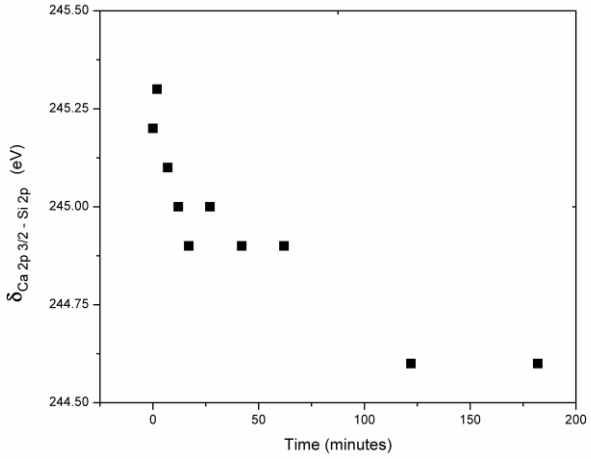

Figure 49 Evolution of the Ca-Si distance during hydration of C_3S thin films.

The formation of C-S-H on the surface of the C_3S thin film during in-situ hydration has also been monitored by a quantitative assessment of the evolution of the molar Ca/Si ratio of the newly formed hydrates. XPS analyses (Table 12) show that the bulk Ca/Si ratio remains constant, evidencing the expected isochemical conditions of the experiment. Fast partial hydration and carbonation of the upper few nanometers of the sample (forming, respectively, portlandite and calcium carbonate) during manipulation under atmospheric conditions may explain the excess Ca content, (Ca/Si of about 3.5 *vs.* 3.0 of stoichiometric tricalcium silicate).

Table 12 Corrected areas and bulk Ca/Si ratios.

Age (min)	Corrected area			Ca2p/Si2p	Ca2p/Si2s
	Si 2p	Si 2s	Ca 2p		
0	9442.6	9059.3	32293.1	3.4	3.6
2	9749.3	9398.7	33291.2	3.4	3.5
7	9428.8	9122.1	32109.5	3.4	3.5
12	9422.6	8912.4	31949.4	3.4	3.6
17	9162.9	8738.6	30736.3	3.4	3.5
27	8163.1	7911.7	30736.3	3.8	3.9
42	8014.2	7978.8	29219.6	3.6	3.7
62	8000.4	7810.0	28623.0	3.6	3.7
122	8809.1	8780.0	30593.5	3.5	3.5
182	8302.2	8138.6	30271.7	3.6	3.7

In order to study the chemical changes during hydration, a deconvolution of the Ca $2p_{1/2}$ and Ca $2p_{3/2}$ peaks has been carried out in order to separate the

contributions from carbonates and silicates. That is, when the experimental peaks cannot be adjusted using only one function, that means they are composed by several peaks that, summed, compose the experimental data peak. This is common in chemical analysis with XPS as the elements chemically combined in different ways present slight different peak position.

In this case calcium silicates are known to have Ca 2p binding energies slightly higher than those of calcium carbonates (Figure 50a). Accordingly, when the higher energy components of the Ca 2p peaks are used to correct for the carbonate content, the silicate (hydrate) Ca/Si ratio drops from about 3.5 (uncorrected) to values that decrease from about 1.6 to 0.5, as hydration progresses (Figure 50b). Although small contributions from portandite and/or unhydrated C_3S cannot be excluded, such low Ca/Si values clearly evidence the presence of C-S-H.

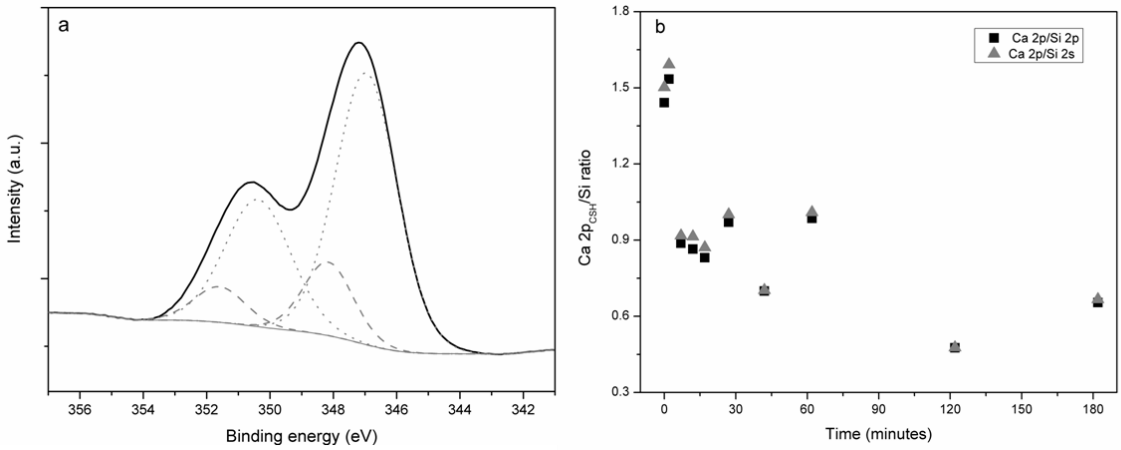

Figure 50 (a) Deconvolution of the Ca 2p peaks that evidences the carbonate (dotted) and silicate (dashed) contributions; (b): Evolution of the Ca/Si ratio of the C-S-H as a function of hydration time.

The progressive change of the Ca/Si of the C-S-H indicates structural changes of the silicate hydrates. In fact, the decrease of molar Ca/Si ratio of C-S-H was interpreted to correspond to a progressive polymerization and subsequent increase of chain length, as progressive polymerization of silicate tetrahedra is compositionally equivalent to an increase of SiO_2 content [14, 15]. This is consistent with recent views [16] that, after an initial rapid reaction with water, the silicate hydrates undergo a slow dissolution process and subsequent hydration yields to longer chain structures. Results from this work strongly suggest that the first precipitate, probably formed by

pre-hydration of C_3S under atmospheric conditions, is a jennite-like material, with a Ca/Si ratio of about 1.5, and evolves to a tobermorite-like material at the end of the 3-hour experiment.

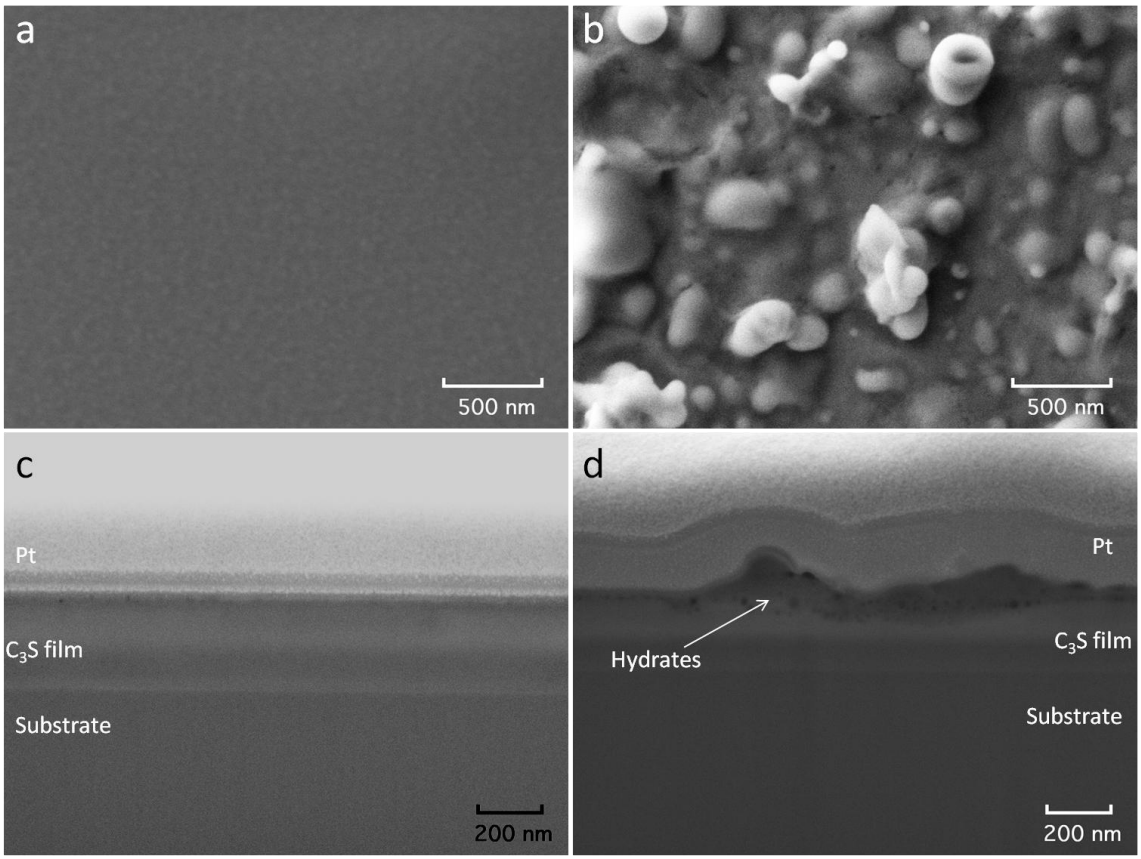

Figure 51 Scanning electron microscope images of the surface of the C_3S thin films at: (a) unhydrated initial conditions. (b) after 182 minutes of hydration. Lower images show: (c) a cross section of the unhydrated sample; (d) and after exposure to water, produced by selective milling with a gallium focused ion-beam. Image shows the presence of small hollow bubbles and increasing on the roughness, probably resulting from the formation of C-S-H. Figures show the distinction among the different layers (silicon wafer substrate, C_3S thin film and platinum cover).

Finally, a combined FIB/SEM (secondary electrons) study has been used to monitor the microstructural changes of the samples. At the beginning of the hydration, the surfaces of the thin films were essentially flat at the nanometric scale, and no significant surface features can be distinguished (Figure 51a). Roughness due to formation of hydrates increased progressively and at the end of the experiment, small clumps of C-S-H of a few hundreds of nanometers covered all the area exposed to water (Figure 51b). In order to obtain a cross section view of the sample, and avoid local charging and subsequent defocussing of the FIB, a thin layer of platinum of a

few tens of nanometers was deposited on the thin film prior to selective milling. Before exposure to water, C_3S appears as a uniform, flat layer (Figure 51c); after 182 minutes of hydration a layer of hydrates, rough and porous, related to the formation of C-S-H is clearly observed (Figure 51d).

5.1.2.2 STXM analysis

The Ca $L_{2,3}$-edge analysis of the C_3S 25 nm film show signs of hydration by the formation of calcium clusters around the sample, although calcium seem to be all around because of the nature of the sample. Figure 52 is the image contrast of one of these formations approximately after 50 minutes of hydration at the energy of 390 eV. Line scan was taken through the cross section on the x-y plane following the arrow, showing variations on the chemical composition inside and outside the particle. The peak related to the C-S-H formation at 346.8 eV is higher inside the particle, confirming the high content of calcium.

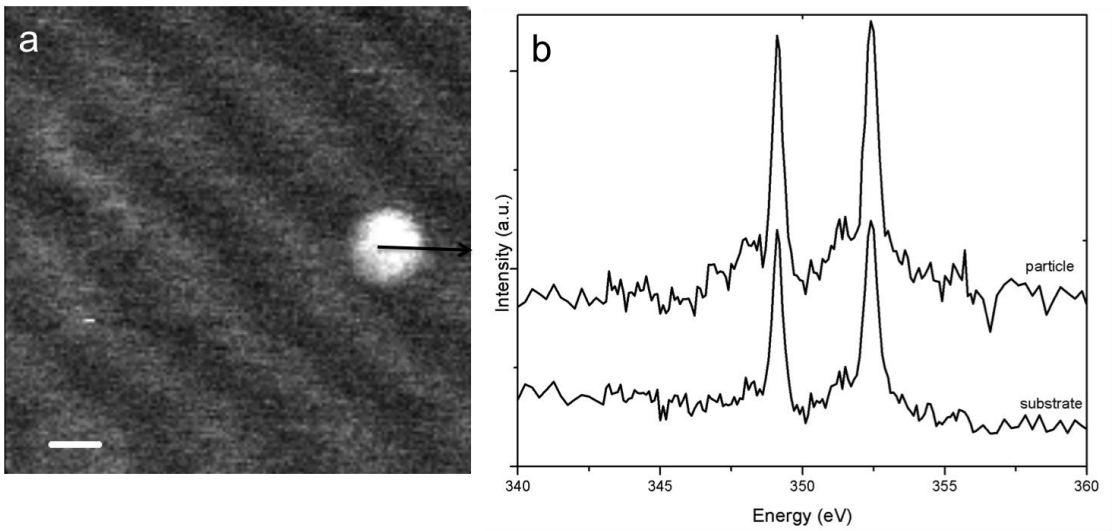

Figure 52 (a) Image taken at the calcium $L_{2,3}$-edge of the C_3S sample. Scale bar=5 μm. (b) NEXAFS spectra of the line scan indicated in *a*.

Figure 53 shows a particle after 254 minutes of hydration. An image stack around the squared region allows scanning all the area, pixel by pixel, for a determined range of energies. In this way each pixel has spectral information of the composition of the sample at that point. Here five different regions provide different spectra depending on the area in the particle.

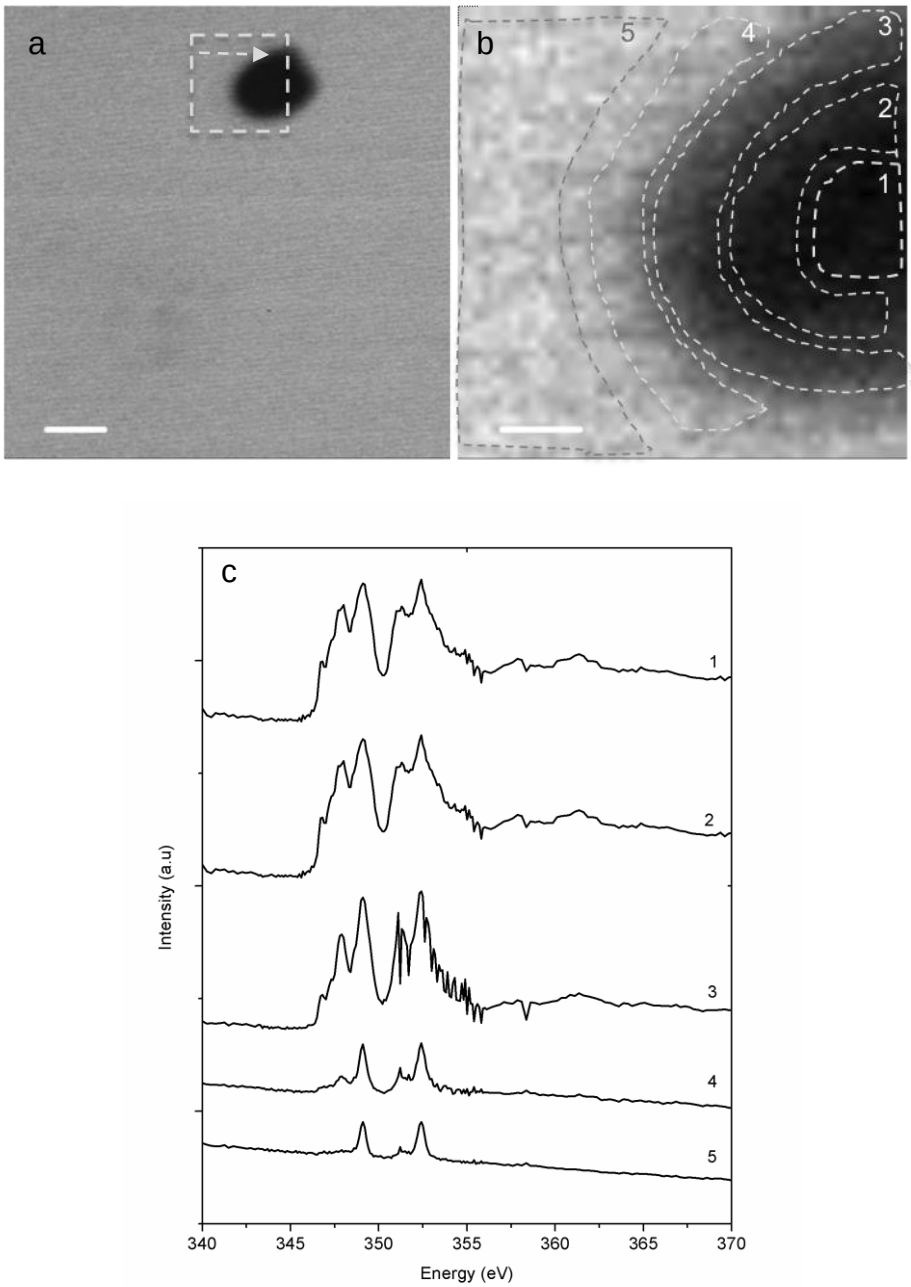

Figure 53 Calcium $L_{2,3}$-edge of a particle after 254 minutes of hydration (a) Image scan of the region at the calcium edge, with the formation of particles with higher concentration of Calcium. Dashed square indicates the area where the image stack was taken. Scale bar=1 um. (b) Image stack around calcium edge with the areas analyzed. Scale bar=200 nm. (c) NEXAFS spectra of the locations indicated in *b*.

There are clear differences in the concentration of calcium inside, at the border and outside the particle. The higher intensities close to the center of the particle report higher concentration of calcium while spectra 1 and 2 present a clear peak around 346.8 eV, related to the formation of C-S-H, however they seem to be

saturated. When approaching the border of the grain this peak decreases, and does not appear outside the grain (spectrum 5). This indicates that, even with the presence of calcium all around the sample, the C-S-H only forms in some parts.

Additionally line scans taken at the same place, through the cross section of the arrow in Figure 53a, at the ages of 208 and 459 minutes show differences in intensity, that is related to the amount of calcium in the region, as well as a slight difference in the peak related to the C-S-H outside, in the border and inside the particle (Figure 54).

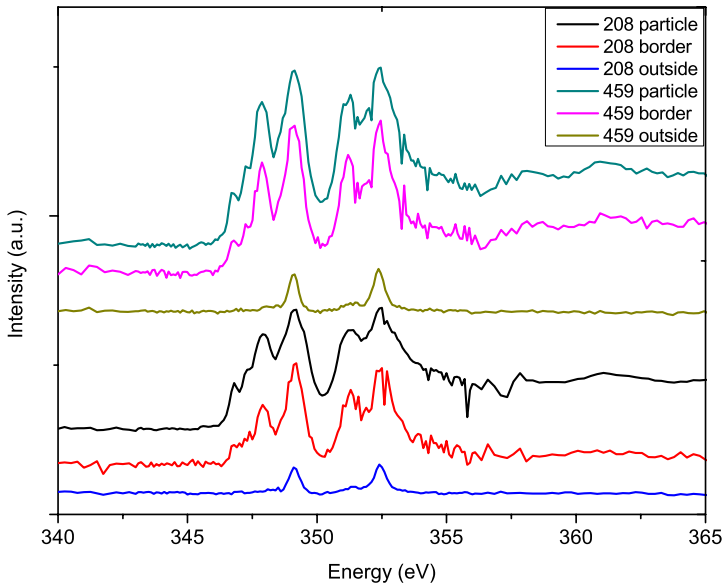

Figure 54 Calcium $L_{2,3}$-edge NEXAFS spectra of line scans in a particle after 208 and 459 minutes of hydration.

During the hydration process, images at 343 eV (the Ca pre-edge) and at the Calcium peak, 349.5 eV, were taken. Only at the energies where the material absorbs (resonates) the most it is able to observe some features (spots or particles), spectroscopically selected. The denser (thicker) these features are, the brighter they appear, and their spectra tend to saturation. The difference between the two images shows the areas where there is a high concentration of calcium, which is where the image is brighter. Considering that all the substrate is covered by calcium from the C_3S, the brighter areas are the places where the C-S-H precipitates.

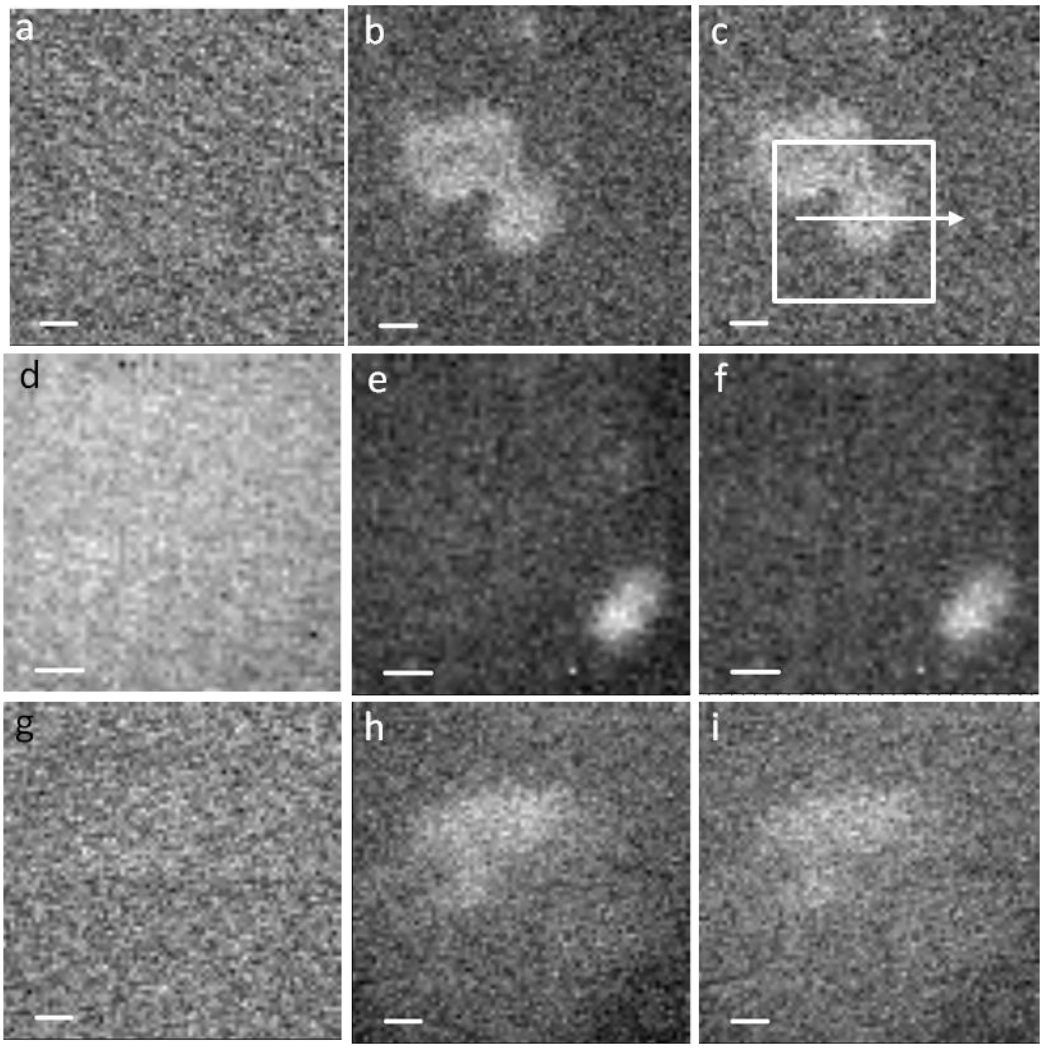

Figure 55 STXM images of C_3S thin film hydrated in situ taken below Ca $L_{2,3}$-edge (*a*, d, g at 343 eV) and above Ca $L_{2,3}$-edge (*b*, e, h at 349.1 eV), and Ca map on third column (substraction of images on the first column from images on the second column: c, f, i). (a, b, c): after 527 minutes. (d, e, f): after 598 minutes. (g, h, i): after 748 minutes. Scale bar=200nm.

However even with these differences noted on the image contrast maps, there is no difference in the calcium NEXAFS spectra in these particles when line scan is performed (for example in the arrow in Figure 66c), indicating no heterogeneity in the 25-nm spatial resolution.

On the other hand image stack performed in the area of the square marked in Figure 55c shows very small difference on the calcium edge. Spectra were taken from each area shown in Figure 56 after 327 minutes of hydration, where a slight difference mainly on intensity can be observed, proving that differences in the

amount of calcium in each region exist. Note that image stack takes around 40 minutes to be completed.

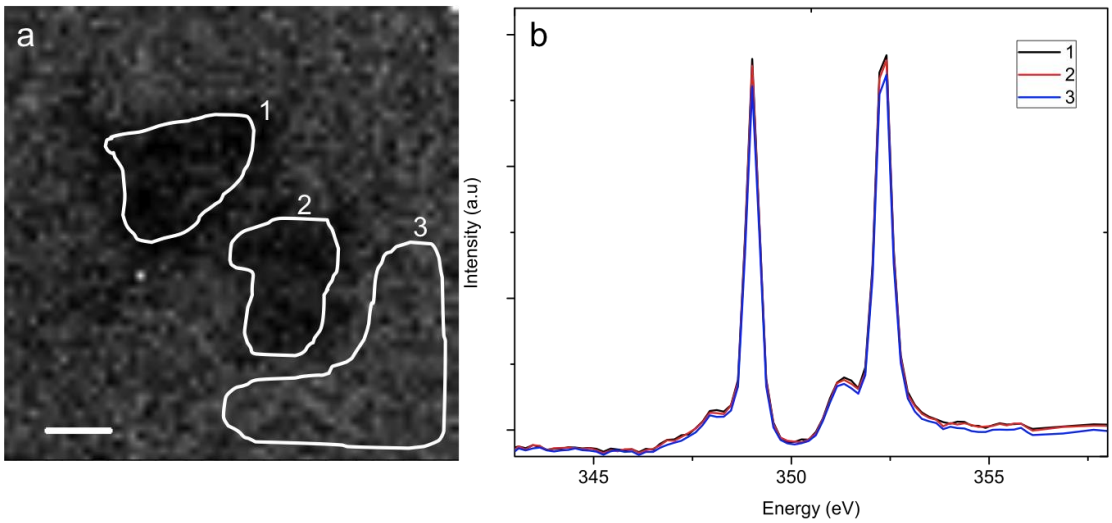

Figure 56 Calcium $L_{2,3}$-edge of a region after 327 minutes of hydration (a) Image stack around calcium edge with the areas analyzed. Scale bar=100 nm. (b) NEXAFS spectra of the locations indicated in a.

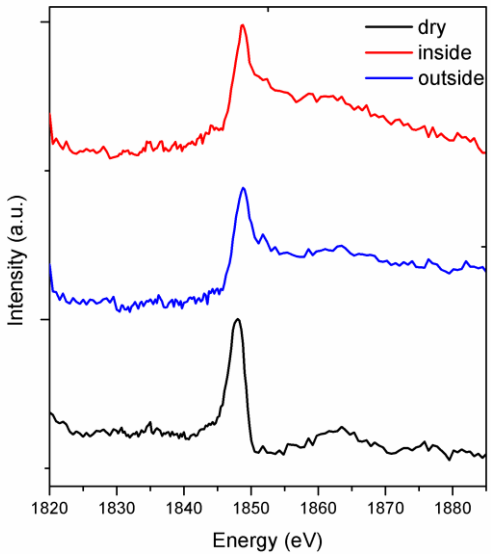

Figure 57 Comparison of dry sample and after 151 minutes of hydration: inside and outside an hydrated particle.

The Si K-edge spectra are noisier than for Ca $L_{2,3}$-edge. Line scans performed in the dry 100 nm thick C_3S sample indicate the presence of silicon in a peak at 1848 eV. However comparison among the initial, dry Si K-edge C_3S spectrum and the particle and surroundings spectra in a stack image after 151 minutes of hydration

(Figure 57) shows clearly that the Silicon peak shifts about 0.8 eV to higher energy in its absorption edge. This is a sign of silicon polymerization by the formation of C-S-H.

Figure 58 shows some particles formed after 287 minutes of hydration. An image stack was performed and five different regions were analyzed.

Differences on the intensity are related to the concentration of silicon in different regions and it is clear that brighter areas present higher intensities and higher concentration of silicon. Outside the particles the intensity of the peak decreases. This indicates that silicon is present in the entire sample but is concentrated mainly in some areas.

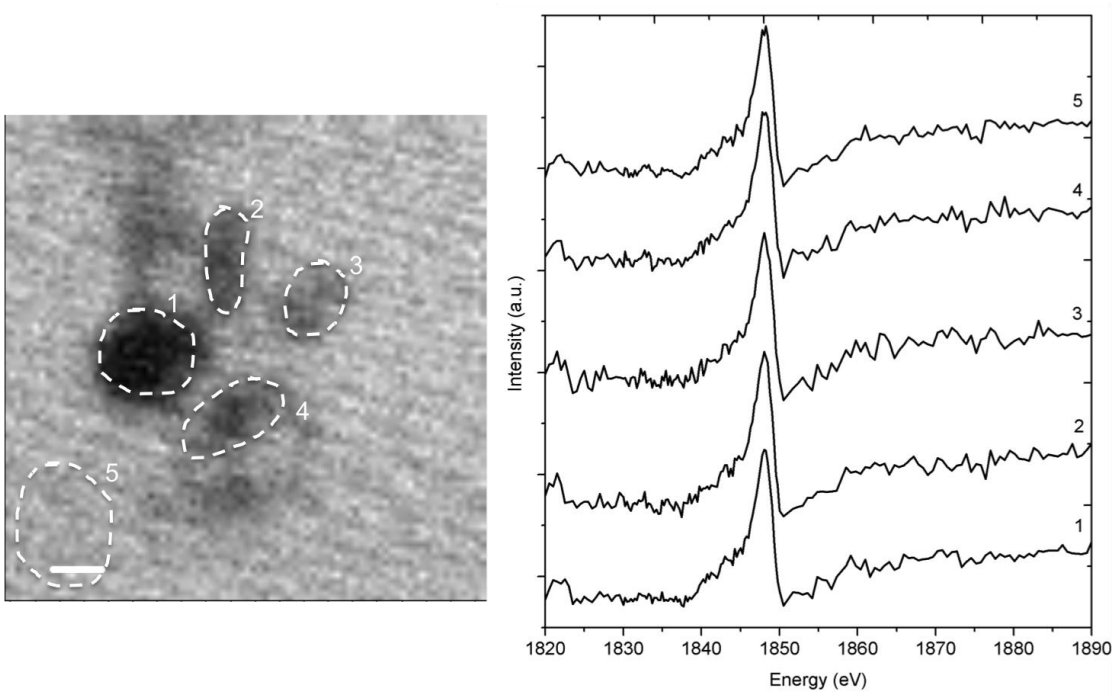

Figure 58 (a) Absorption image stack around the Silicon K-edge after 151 minutes of hydration with the areas analyzed. Scale bar=100 nm. (c) NEXAFS spectra of the locations indicated in *a*.

On the other hand line scans were performed in places of interest. Figure 59 presents line scans in some particles where it is clear that there are differences. However spectroscopy shows that there is no chemical difference in the silicon NEXAFS spectra in these particles when linescan is performed, indicating no heterogeneity in the 25-nm spatial resolution. Nevertheless a strong difference in the intensity is observed, once again related to differences in the concentration of silicon.

Even so with time it is observed the development of additional particles in the same area.

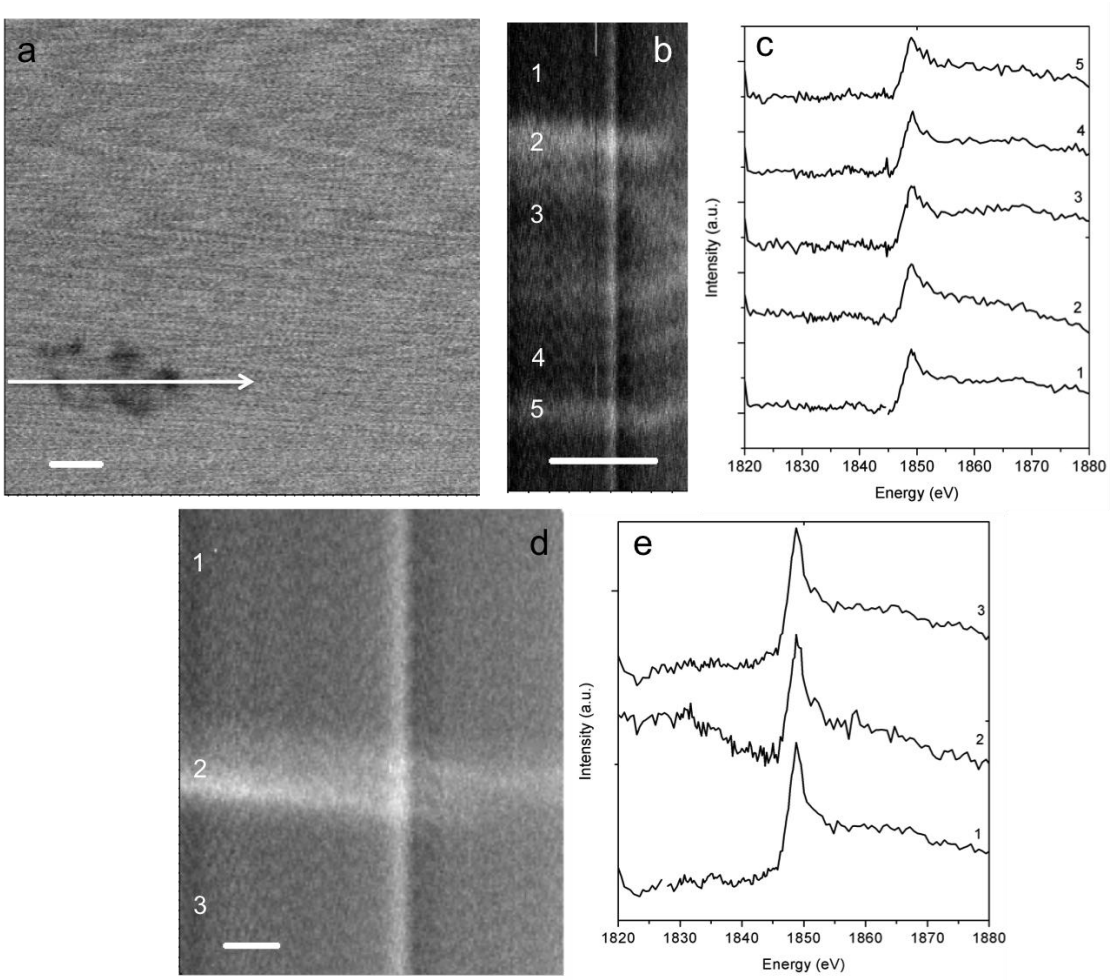

Figure 59 (a) Absorption image scan of the Silicon K-edge showing some particles formed with the hydration. Arrow indicates location of the linescans. Scale bar=500 nm. (b) Si K-edge of the linescan taken at 51 minutes of hydration showing the differences in optical density. (c) Si K-edge NEXAFS spectra of line scan in the particles after 51 minutes of hydration. (d) Si K-edge of the linescan taken at 229 minutes of hydration showing the differences in optical density. (e) Si K-edge NEXAFS spectra of line scan in the particles after 229 minutes of hydration.

Additional analysis of one-particle trough line scans over time during the hydration (Figure 60) indicates changes while the peak at 1842 eV increases with time. It is not present neither in the substrate (outside the particle) nor in the particle in the initial ages, but after 285 minutes its presence is evident. It can be related to the formation of C-S-H in this region during this time.

The same behavior is observed in another particles with stronger evidences. Figure 61 shows linescans over time of hydration where there is a clear increasing on the intensity of the silicon peak. That is an increase in the concentration of silicon in the particle. Even with no significant changes on the energy this increase can be related to the agglomeration of silicon by the formation of C-S-H particles.

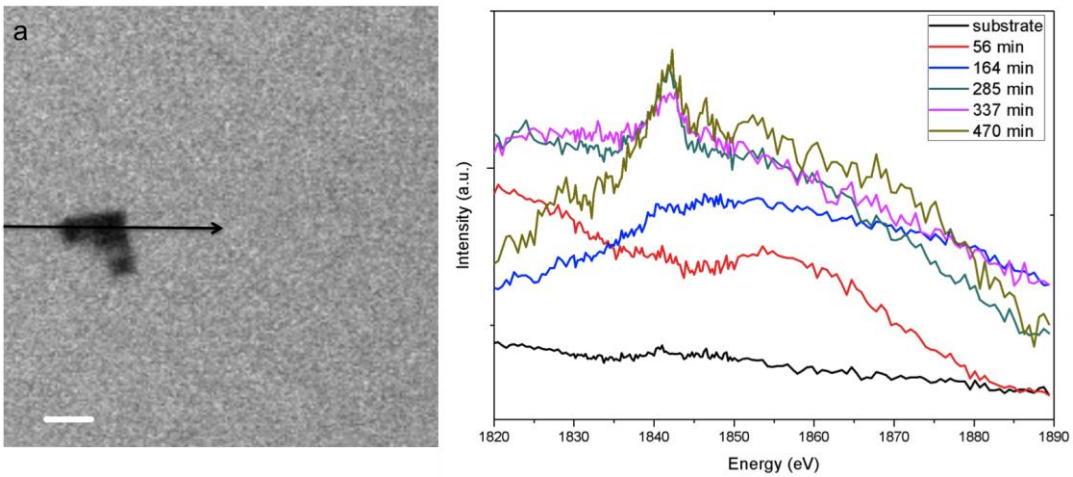

Figure 60 (a) Absorption image scan of the Silicon K-edge showing some particles formed with the hydration. Arrow indicates location of the linescans. (b) Si K-edge NEXAFS spectra of line scan in the particles after different times of hydration. Scale bar = 500 nm.

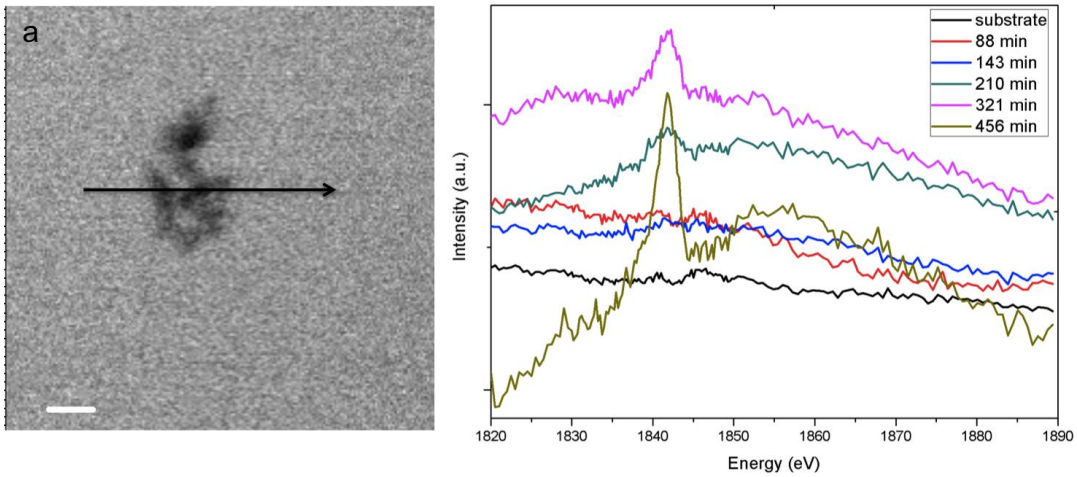

Figure 61 (a) Absorption image scan of the Silicon K-edge showing some particles formed with the hydration. Arrow indicates the location of the linescans. Scale bar = 500 nm. (b) Si K-edge NEXAFS spectra of line scan in the particles after different times of hydration.

Image stack in another particle after 550 minutes of hydration (Figure 62) indicates smaller differences, however still significant, in intensity, related to the

concentration of silicon in different regions, but also slight differences in the energy. It seems to be higher inside the particle than in the substrate, indicating that silicon is present in the entire sample but is concentrated mainly in some areas. However with the resolution obtained it is not possible to assure this behavior.

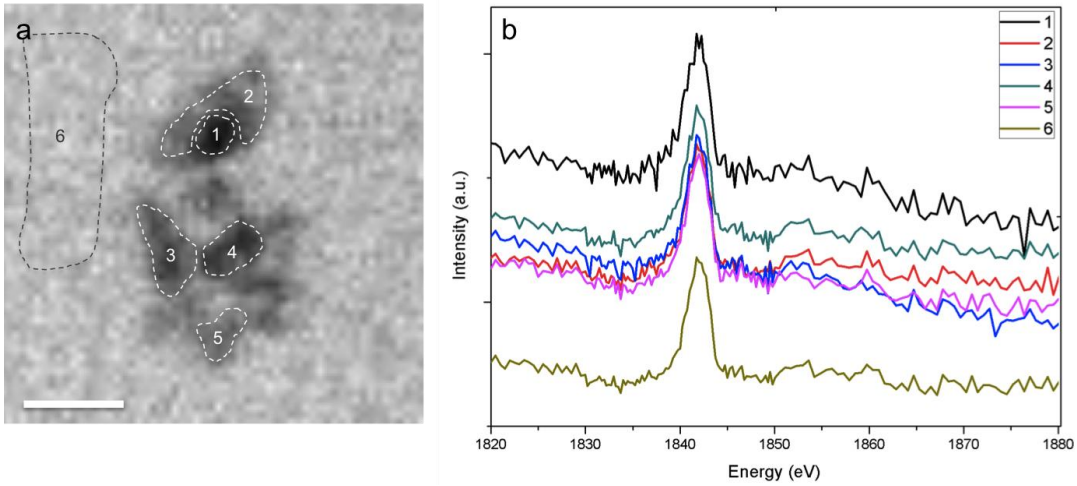

Figure 62 (a) Absorption image stack around the Silicon K-edge after 550 minutes of hydration with the areas analyzed. Scale bar=500 nm. (c) NEXAFS spectra of the locations indicated in *a*.

5.2 Chemical changes during the hydration of ß - dicalcium silicate thin films

This section presents a study of C_2S thin film during hydration with water vapor in a reaction chamber with no external contamination and monitored by the X-ray photoelectron spectroscopy in the same way as previously described for C_3S, as well as hydration in water following the Silicon K-edge with the STXM. It was possible to follow changes on the surface composition, elementally and structurally, providing elemental information on the early hydration of C_2S by the formation of C-S-H related to the silicon polymerization and variations on the Calcium/Silicon ratio.

5.2.1 Experimental

ß-dicalcium silicate (C_2S) thin films with 200 nm thickness previously described were fixed on a metallic holder with a copper tape and analyzed with XPS

in a similar way as the C_3S samples described previously. General scan was repeated three times and specific scans with high resolution were performed for elements of interest such as Calcium, Silicon, Carbon, Oxygen, and some other material that could be identified in the general scan (Table 13). Data were extracted from the spectra via peak fitting using CasaXPS software. A Shirley background was assumed in all cases and spectra were corrected for charging effects using the adventitious carbon peak at 284.8 eV. Passing energy is equal to 5 eV and number of scans is equal to 3 for all patterns.

Table 13 Details of spectral lines recorded

	XPS conditions			Composition	
Region	Start energy (eV)	End energy (eV)	Dwell time (ms)	Starting material (at.%)	Thin film (at.%)
Wide	0	1200	0.25	-	-
C 1s	275	295	1	9.7	32.9
O 1s	525	540	0.5	59.0	42.6
Ca 2p	339	359	1	20.8	15.8
Si 2p	94	114	1	10.5	8.8
Si 2s	143	163	1		
Mn 2p	40	60	1	-	-

When comparing the atomic concentration of the starting material and the thin film differences are noticed mainly due to the higher presence of carbon. This may be due to an increasing on the adventitious carbon peak, related to carbon contamination, during the production of the thin films.

On the other hand the amount of Magnesium is too small (0.5 atomic percent, from X-ray fluorescence) and its response factor is so low (0.334) that it cannot be differentiated from the noise on the spectrum considering the resolution of the technique and for this reason it does not appear in the quantification.

After running the initial pattern, a dry thin film sample was transferred to a reaction chamber in the same vacuum line as the XPS, thus avoiding any atmospheric contamination. The same vaporizer with Milli-Q water was used to insert water vapor saturated with argon at 20 mL/min. Prior to hydration system was purged for 5 minutes.

The Focused Ion Beam microscope was used for observation, selective milling and deposition on the same sample in two conditions: at the initial unreacted condition and after submitted to the hydration at the end of 632 minutes.

Finally the topography of the sample was measured with the AFM in order to identify changes in roughness and surface area variations. AFM was settled in tapping mode using a silicon nitride tip DNP-S10 with k=0.58 N/m.

Table 14 Experimental conditions for each stage of hydration of C_2S thin films.

Time of exposure (min)	Accumulated exposure time (min)	Temperature (ºC)	P (H_2O) (mbar)
2	2	26.5	34.6
5	7	26.9	35.4
5	12	26.9	35.4
5	17	27.3	36.3
10	27	25.8	33.2
15	42	26.7	35.0
20	62	26.1	33.8
60	122	27.9	36.9
60	18 2	26.6	34.8
90	272	28.1	38.0
360	632	26.7	35.0

Regarding the STXM samples, same procedure as for C_3S samples was followed. Sensibility for samples with 100 and 220 nm was tested for Ca, Si and C in order to choose the appropriated thickness for each element.

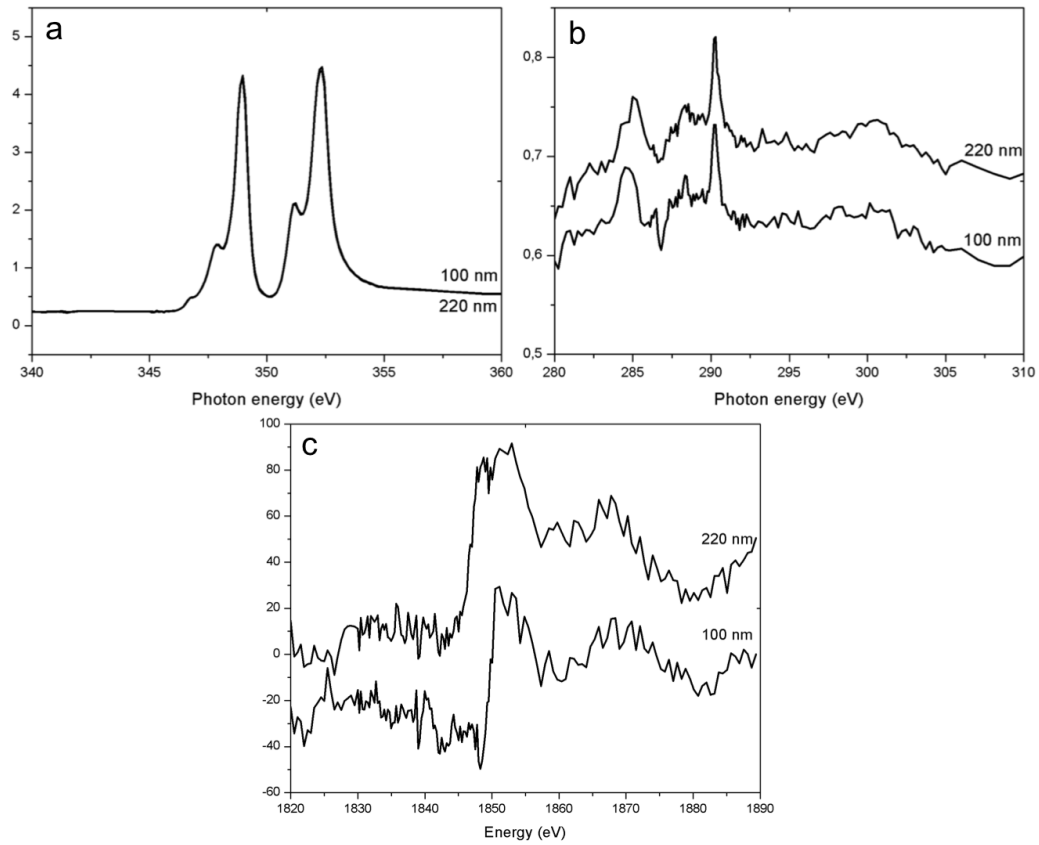

Figure 63 Comparison of C_2S samples with different thickness. (a)Calcium $L_{2,3}$-edge. (b) Carbon K-edge. (c) Silicon K-edge.

The same behavior as in C_3S samples is observed for C_2S thin films, however no thinner samples were produced and for this reason no data was taken for the calcium edge. The Calcium edge presents exact same behavior while in the Carbon edge it is possible to see that, for this element, the thinner film is preferable.

5.2.2 Results and discussion

The bulk material was pressed into pellets prior to the analysis with the XPS. The results show a Ca/Si ratio of 2.0, exactly the expected, and $\delta_{Ca\ 2p\text{-}Si\ 2p}$ is 245.8 eV, higher than the value found by Regourd [17] (245.4 eV). However his Si 2p peak width is exactly the same as observed here.

Table 15 Binding energies and peak width (FWHM) of the elements found in the bulk C_2S.

	Binding energy (eV)	Peak widths (FWHM)
Ca $2p_{3/2}$	346.8	2.3
Si 2p	101.0	2.7
Si 2s	153.1	3.4
O 1s	531.6	2.8
	530.1	2.2

Observing the evaporated thin film prior to any treatment the Ca 2p/Si 2p ratio is equal to 1.6, value lower that the found in the bulk material. This can be due to pre hydration by the contact with the atmosphere during the sample manipulation or due to preferential deposition of the silicon on the sample's surface after the evaporation. On the other hand, the peak positions are similar to the bulk material, proving that the chemical state is preserved after the evaporation (for example 346.8 eV and 347.0 eV for Ca $2p_{3/2}$; 101.0 eV and 101.2 eV for Si 2p, for bulk and evaporated material, respectively). Additionally, the $\delta_{Ca\ 2p\text{-}Si\ 2p}$ is exactly the same for both cases, supporting the theory of preferential deposition on the surface as this parameter assures the sample is not hydrated compared to the bulk material.

The overall initial binding energy of the bulk material is higher than the sample analyzed by Black et al [10] (347.0 eV *vs.* 346.87 eV for Ca 2p 3/2, 101.2 eV *vs.* 100.8 eV for Si 2p and 152.2 eV *vs.* 151.92 eV for Si 2s). Additionally, it agrees with them that the binding energies for silicon on C_2S are higher than that for C_3S presented previously (101.9 eV for Si 2p and 152.9 eV eV for Si 2s).

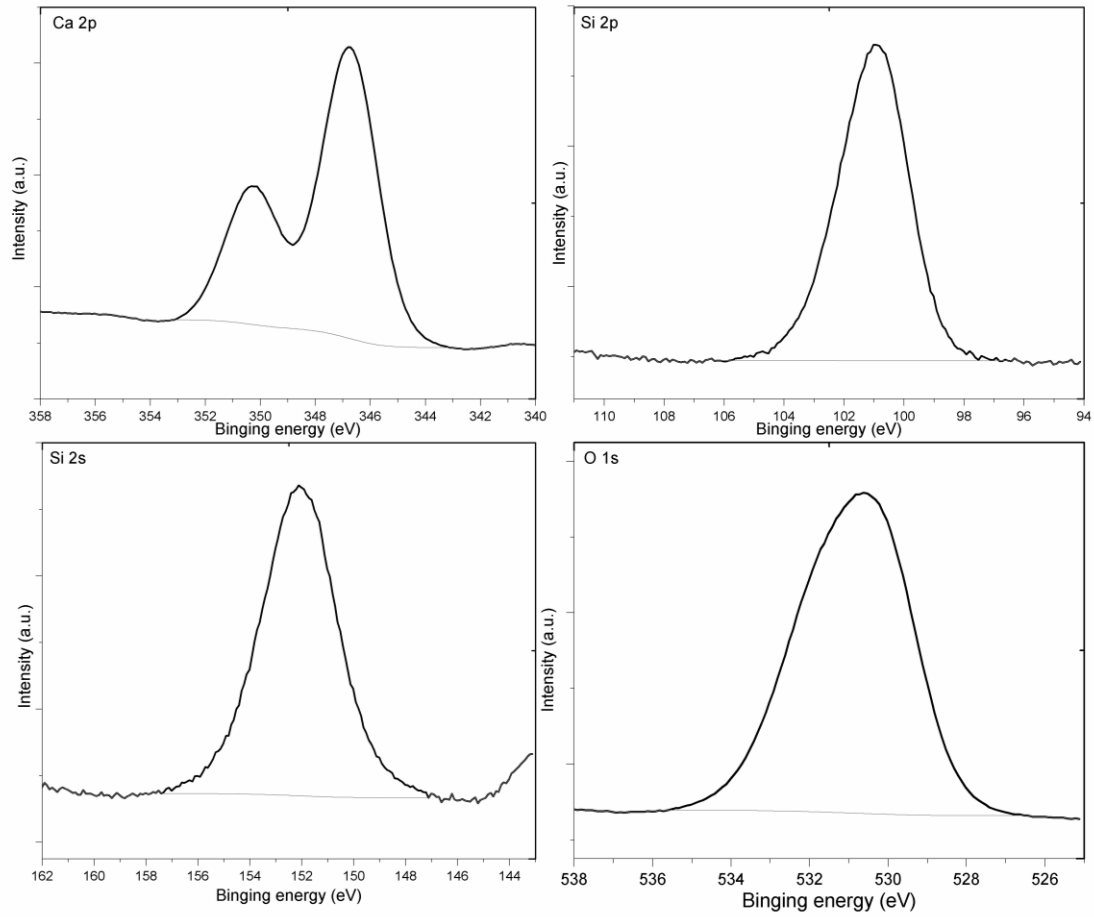

Figure 64 XPS spectra of the bulk C_2S.

With the time of exposure to water vapor the XPS analyses of the C_2S thin film show a drift of the main Si 2p (from 101.2 to 102.6 eV) and Si 2s (from 152.2 to 153.7 eV) peaks indicating the progressive disordering of the silicate structure related to C-S-H formation. Hydration progress yields a peak broadening at higher ages forming an additional peak at around 100.2 and 151.2 eV range. The same behavior is described by Black et al [10] whom found a Si $2p_{3/2}$ binding energy of 100.8 eV for the fresh C_2S and 102.44 eV with a new peak at 100.51 eV for the aged sample. The peak at lower energies is related to unaltered β-C_2S while the peak at higher binding energy is assigned to a calcium-depleted C-S-H phase.

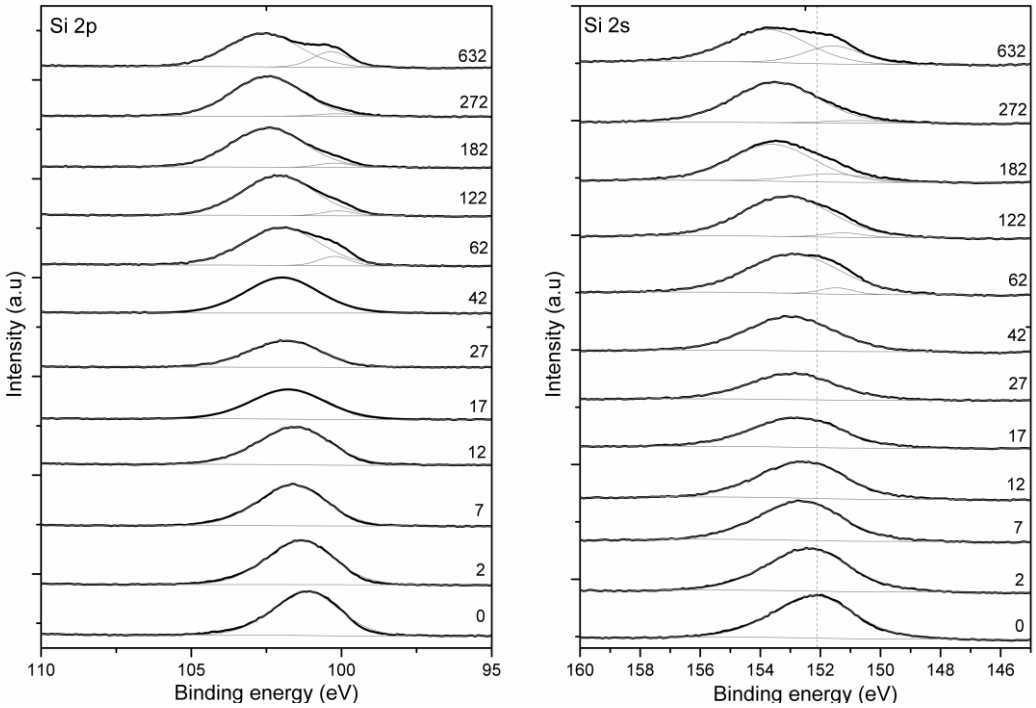

Figure 65 XPS spectra of the C_2S thin film showing the evolution of the Si 2p (left) and 2s (right) peaks during exposure to water vapor. Labels on the right indicate time of hydration in minutes.

The Ca binding energies show a somehow more erratic behavior, and a small progressive shift has been observed (0.7 eV) when hydration goes on. The Ca $2p_{3/2}$ peak is centered at around 347.0 eV (Table 3) for fresh C_2S, a value slightly lower than the one previously reported by Black et al [10] (347.23 eV).

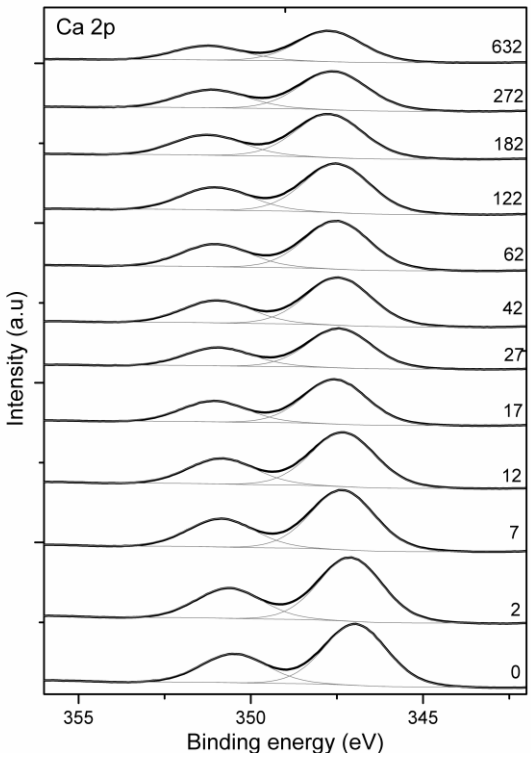

Figure 66 Calcium spectra (lower and higher energy peaks correspond, respectively, to Ca $2p_{3/2}$ and Ca $2p_{1/2}$ lines) of the C_2S thin film showing the variation of the peaks during the exposure to water vapor.

Table 16 Evolution of binding energies of Si and Ca (peak width, FWHM) and Ca-Si peak distance during vapor hydration of C_2S.

Age (min)	Binding energy (eV)			Ca-Si distance (eV)
	Si 2p	Si 2s	Ca 2p 3/2	$\delta_{Ca\ 2p\text{-}Si\ 2p}$
0	101.2 (2.6)	152.2 (3.2)	347.0 (2.1)	245.8
2	101.4 (2.6)	152.4 (3.3)	347.1 (2.1)	245.7
7	101.7 (2.7)	152.7 (3.3)	347.3 (2.6)	245.7
12	101.6 (2.8)	152.6 (3.4)	347.3 (2.2)	245.7
17	101.8 (2.9)	152.8 (3.5)	347.5 (2.1)	245.8
27	101.9 (2.8)	152.9 (3.4)	347.4 (2.1)	245.5
42	102.0 (2.9)	153.0 (3.4)	347.4 (2.2)	245.5
62	100.2 (1.2) 102.0 (2.9)	151.5 (1.3) 152.9 (3.6)	347.5 (2.2)	245.5
122	100.1 (1.2) 102.1 (2.8)	151.2 (1.5) 153.1 (3.4)	347.5 (2.2)	245.4
182	100.2 (1.3) 102.4 (2.9)	151.7 (2.9) 153.6 (3.3)	347.7 (2.3)	245.3
272	100.2 (1.7) 102.5 (2.8)	150.8 (2.5) 153.5 (3.4)	347.6 (2.3)	245.1
632	100.4 (1.4) 102.6 (2.8)	151.6 (2.2) 153.7 (3.1)	347.7 (2.2)	245.1

The calculated energy separation between Ca $2p_{3/2}$ and Si 2p peaks ($\delta_{Ca2p\text{-}Si2p}$) and their evolution with time of hydration are plotted in Figure 67. The initial values of $\delta_{Ca2p\text{-}Si2p}$ found in this work (245.8 eV) are somewhat lower than those reported by Black et al [10], (246.72 eV). This is due to the polymerization of the isolated silicate tetrahedra upon formation of C-S-H, and/or carbonation [14], although formation of calcium carbonate is not likely to occur under the experimental conditions of this work.

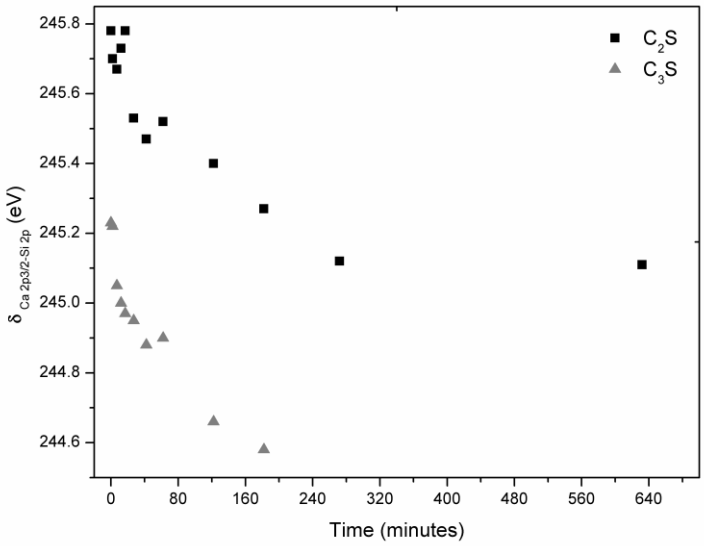

Figure 67 Evolution of the Ca-Si distance during hydration of C_2S thin films.

Comparison of these and the results for C_3S presented in Section 5.1.2.1 shows that the silicon polymerization occurs faster in that material as the $\delta_{Ca2p\text{-}Si2p}$ distance decreases faster when the same conditions are applied, indicating a faster formation of C-S-H. It is well known that C_3S reacts faster than the C_2S, which continues reacting for over a year in concrete.

XPS analyses show that the Ca/Si ratio starts with a lower value than expected from the bulk material and decreases over time, evidencing the partial hydration of the upper few nanometers of the sample during manipulation under atmospheric conditions (initial Ca/Si of about 1.6 *vs.* 2.0 of stoichiometric di-calcium silicate, Figure 68).

The same behavior and same values were observed by Regourd [17], who found a Ca/Si ratio of 1.5 after 1 minute of hydration and of 1.0 after 4 hours, same values observed here.

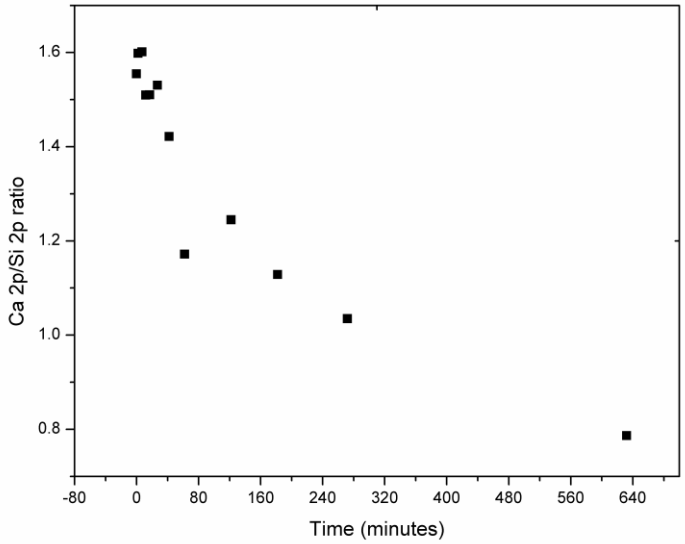

Figure 68 Evolution of the Ca/Si ratio of the sample as a function of hydration time.

Contrarily of the behavior observed and previously reported for a C_3S sample, the C_2S does not present different peaks related to the contributions from carbonates and silicates even when a deconvolution is performed. This may be due to more careful storage applied to the C_2S sample, that was kept in vacuum during all the time, being exposed to the atmosphere only during the transportation and sample preparation times.

As in the C_3S samples such low Ca/Si values clearly evidence the formation of C-S-H, even if small contributions from portandite and/or unhydrated C_2S cannot be excluded.

Finally the O 1s spectrum provides important information on the structure of minerals and glasses. An extensive study of oxygen bonding in crystalline C-S-H phases is presented by Black et al [18]. Bridging and non-bridging oxygen atoms can be differentiated by its binding energy, as the former have higher binding energies.

O 1s can be present in different components which have different binding energies: non-bridging oxygen (530-530.5 eV), brindging oxygen (351.5-532.7 eV), hydroxide species (533-533.5 eV) and bound water (~534 eV), portlandite at calcium-

rich samples (531.6 eV), while amorphous silica does not add any extra component [15].

However Black et al [11] underline that samples submitted to high vacuum conditions, as in the XPS, may suffer a loss of bound water. This situation does not influence on the extent of the silicate polymerization or the contributions of the oxygen.

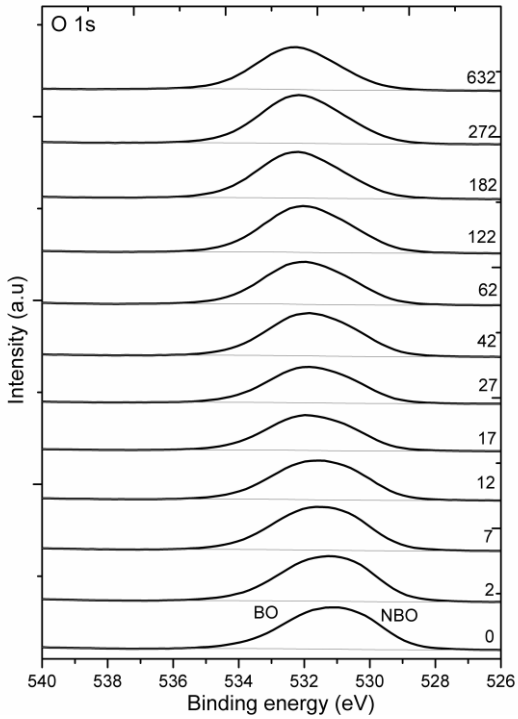

Figure 69 XPS spectra of the C_2S thin film showing the evolution of the O 1s peak during exposure to water vapor. Labels on the right indicate time of hydration in minutes.

Table 17 Evolution of binding energies and peak width (FWHM) of non-bridging (NBO) and bridging (BO) oxygen and NBO-BO peak distance during vapor hydration of C_2S.

Time (min)	Binding energy (eV) and FWHM		δ_{NBO-BO}
	NBO	BO	
0	530.1 (1.5)	531.4 (3.0)	1.3
2	530.3 (1.4)	531.5 (3.1)	1.2
7	530.4 (1.5)	531.7 (3.0)	1.3
12	530.3 (1.3)	531.7 (3.1)	1.3
17	530.3 (1.2)	531.9 (3.0)	1.5
27	530.3 (1.5)	531.9 (2.8)	1.5
42	530.2 (1.8)	531.9 (2.9)	1.7
62	530.4 (2.0)	532.1 (2.8)	1.7
122	530.2 (2.0)	532.1 (2.8)	1.8
182	530.4 (1.9)	532.2 (2.8)	1.9
272	530.2 (1.8)	532.2 (2.8)	1.9
632	530.4 (2.0)	532.3 (2.8)	1.9

The O 1s spectra are asymmetric and broad and the contribution from non-bridging oxygen decreases with the time of hydration, i.e. with the decreasing of the Ca/Si ratio. This is due to the fact that the silicate polymerization leads to a decrease on the number of Ca-O-Si units and increasing Si-O-Si units (Figure 69).

The silicon polymerization can be followed by changes on the peaks separation due to bridging and non-bridging oxygen atoms (δ_{NBO-BO}): the peak distance increases with the decreasing of the Ca/Si ratio, that is, with the time of exposure to hydration with water vapor.

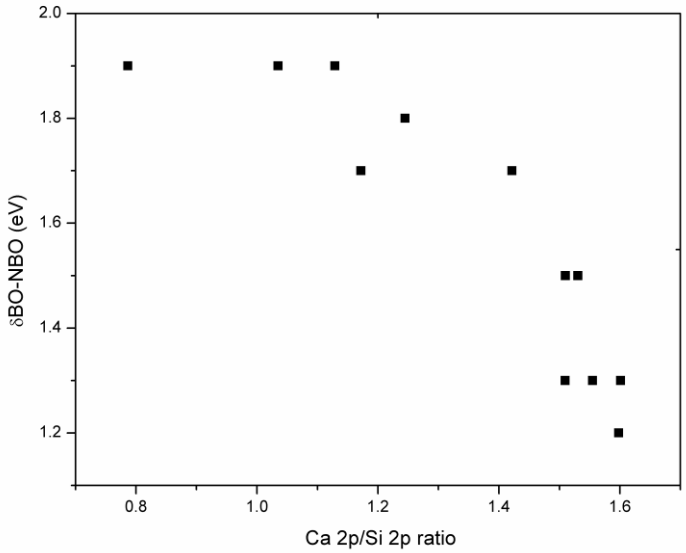

Figure 70 Variation in δ_{NBO-BO} with Ca/Si ratio.

Finally, a combined SEM-FIB study has been used to monitor the microstructural changes of the samples. Before the hydration the surface of the thin film was very flat and no surface feature can be observed (Figure 71a). At the end of the experiment it is observed that roughness increases due to the formation of hydrates with a few hundreds nanometers on the surface (Figure 71b). The cross section view of the sample shows that before exposure to water, C_2S is an uniform and flat layer (Figure 71c), while after the hydration it presents a very thin layer of hydrates (Figure 71d), rough and porous. In comparison to the previously results reported for C_3S, even with higher exposure time, the C_2S presents a thinner layer of hydrates as expected for the slower reaction.

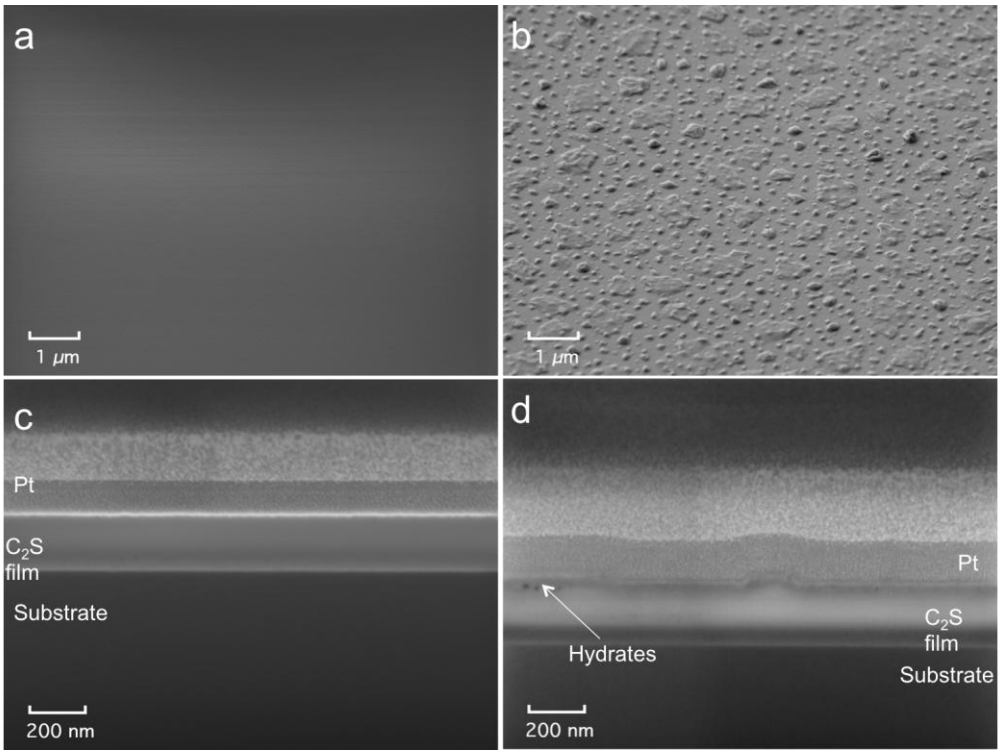

Figure 71 SEM images of C_2S thin film: (a) top view of the sample at its initial condition. (b) Top view of the sample after 632 minutes of hydration. (c) Cross section with a Platinum cover and cut with a Focused ion beam (FIB) at the initial condition and (d) after 632 minutes of hydration, where image show the presence of small hollow bubbles and increasing on the roughness, probably resulting from the formation of C-S-H. Figures show the distinction among the different layers (silicon wafer substrate, C_2S thin film and platinum cover).

Furthermore the AFM was used to verify the differences on the sample surface in the same two conditions described for the SEM/FIB experiments (Figure 72). Images show clear differences on the surface: initially it is very flat with just small roughness (relative height 10 nm). On the other hand after the 632 minutes of hydration the formation of clusters with different sizes is observed, associated to C-S-H (relative height 100 nm).

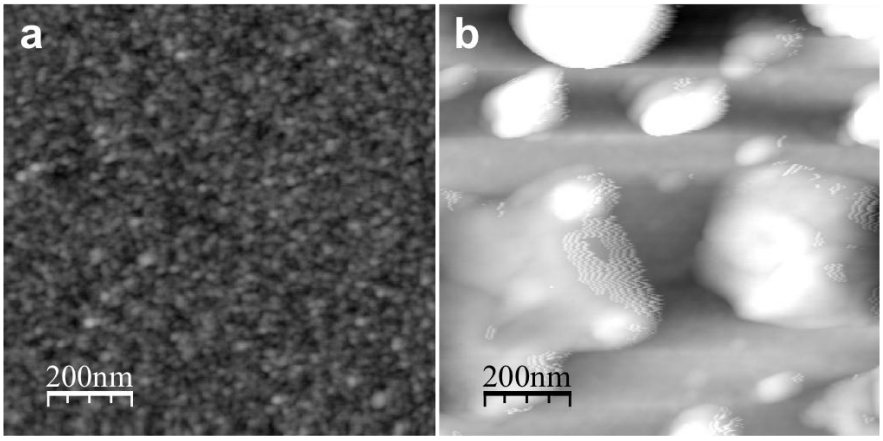

Figure 72 AFM images of C_2S thin film surface: (a) top view of the sample at its initial condition; relative height: 10 nm. (b) Top view of the sample after 632 minutes of hydration; relative height: 100 nm. Figures show the formation of C-S-H after exposure to water vapor.

5.2.2.1 STXM analysis

As mentioned previously the C_2S films, in the conditions they were produced, were not appropriated for being analyzed at the low energies related to the Calcium $L_{2,3}$-edge as the excessive thickness lead to saturation of the optical density, not allowing contrasts to be detected. For this reason 100 nm thick samples were only analyzed considering the Silicon K-edge, described below.

Figure 73a shows the STXM image of the C_2S thin film sample taken at the Silicon K-edge energy. Line scans through the cross section on the x-y plane (arrow) are taken over time of hydration, providing the NEXAFS spectra presented in Figure 73b. It can be noticed that the chemical structure gradually changes as in the early ages the silicon peak at around 1845 eV is less evident and increases over time. A slight shift to higher energies is also identified. These changes can be observed here and not so clearly in the C_3S samples probably because of the velocity of reactions that happen faster there.

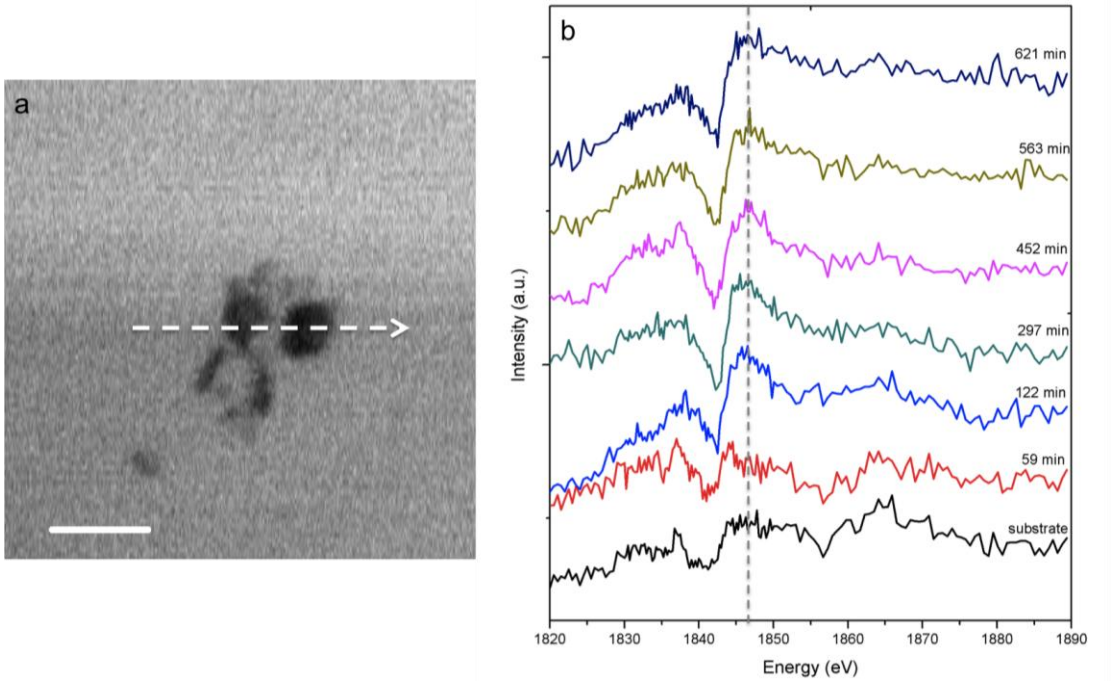

Figure 73 (a) Absorption image scan of the Silicon K-edge showing some particles formed with the hydration of C_2S thin film. Arrow indicates location of the linescans. (b) Si K-edge NEXAFS spectra of line scan in the particles after different times of hydration. Scale bar = 1 μm.

Small areas were chosen for image stack and NEXAFS spectral analysis in different times of hydration. Figure 74a shows an area with some particles where the spectra were collected. Areas numbered correspond to the NEXAFS spectra of Figure 74b. Differences are mainly in intensity: higher intensities, inside the particles, are related to higher concentration of Si. A strong relationship between the darker areas and the more intense signal is observed, indicating the agglomeration of silicon particles probably due to the formation of hydration products, that is, C-S-H. However, no significant differences on the binding energy are observed when comparing regions at the substrate and the particles.

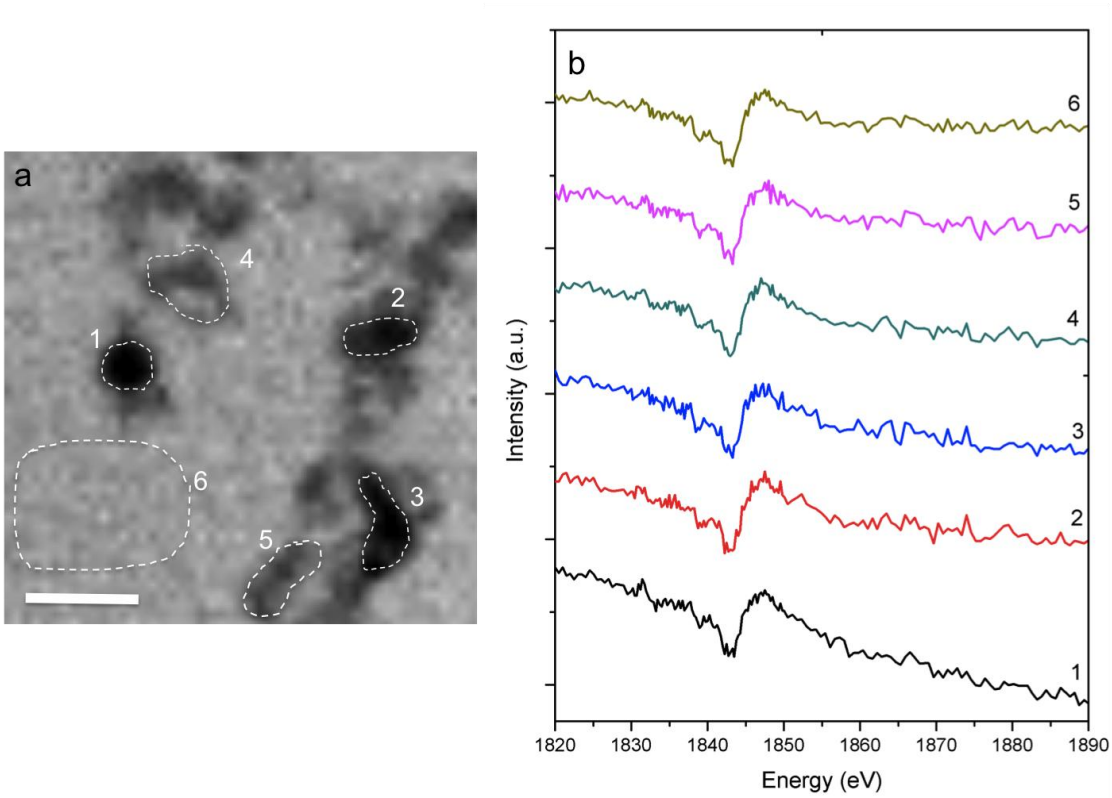

Figure 74 (a) Image stack around the Silicon K-edge after around 300 minutes of hydration with the areas analyzed. Scale bar=1 μm. (c) NEXAFS spectra of the locations indicated in *a*.

Additionally Figure 75a shows another area where different particles were formed, taken at around 10 hours of hydration. NEXAFS spectra presented in Figure 75b are related to the numbered areas and again the main differences are observed in the intensity. However here spectra seem to be saturated and it is not possible to identify any chemical characteristic. Only a difference between the area with no particles and the particles can be notice, but not qualified.

That is clear that experiments on C2S should be repeated in order to acquire more reliable results.

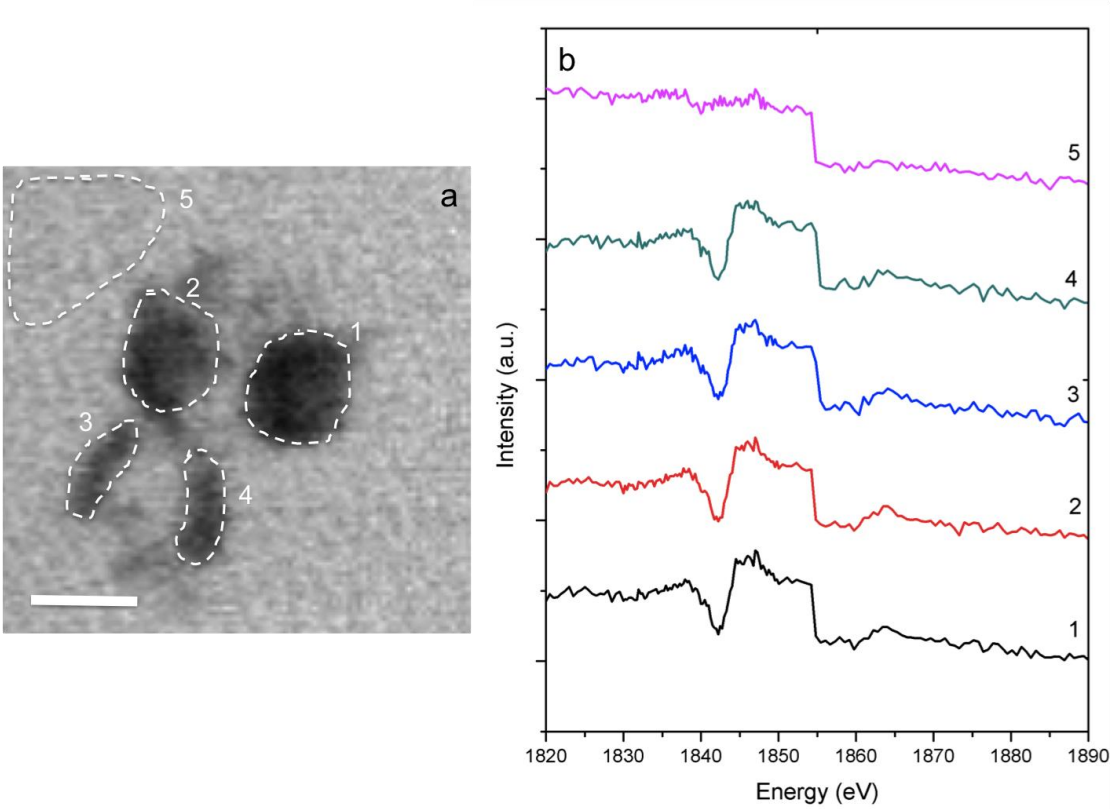

Figure 75 (a) Image stack around the Silicon K-edge after around 600 minutes of hydration with the areas analyzed. Scale bar=500 nm. (c) NEXAFS spectra of the locations indicated in *a*.

After hydration image contrast maps taken at the Si K-edge of different particles show that at energy below the Si absorption energy (1830 eV) the areas containing si become light, while at the energy above (1843.2 eV) the image becomes darker for the detection of silicon. The difference between the two images shows the areas where there is a high concentration of silicon, which is where the image is brighter. Considering that all the substrate is covered by silicon from the C_2S and the membrane, the brighter areas are the places where the C-S-H precipitates.

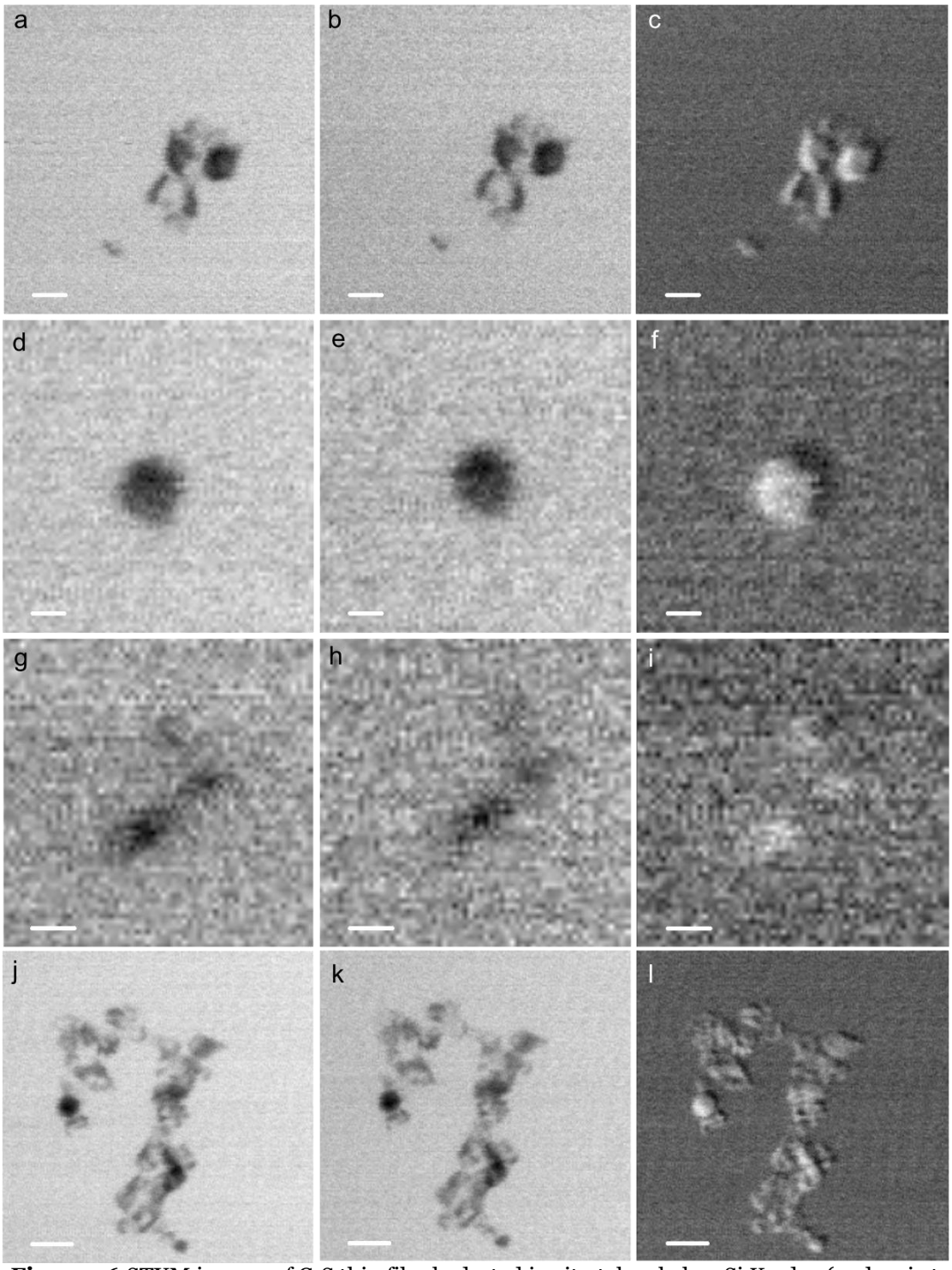

Figure 76 STXM images of C_2S thin film hydrated in situ taken below Si K-edge (*a*, d, g, j at 1830 eV) and above Si K-edge (*b*, e, h at 1844.5 eV and *k* at 1850 eV), and Si map on third row (substraction of images on the first row from images on the second row: c, f, I, l). (a, b, c): after 61 minutes. (d, e, f): after 131 minutes. (g, h, i): after 150 minutes. (j, k, l): after 524 minutes. Scale bar=500nm (a-c), 200 nm (d-i) and 1 µm (j-l).

5.3 Liquid cell AFM study of the early hydration of calcium silicate thin films

When in contact with water both C_3S and C_2S dissolves congruently producing Ca^{2+} and silicate ions. When the supersaturation is reached the C-S-H precipitates (before C_3S/C_2S solubility is attained). C-S-H particles are formed by aggregation around initial nuclei of identical particles. That happens in an anisotropic way [19].

In order to have suitable samples for AFM studies previous researches used sintered pellets of tricalcium silicate polished with alumina powder and absolute alcohol [20] or cut discs of Portland cement clinker or cement paste with a diamond saw, polishing it with sandpapers [21-24]. With the aim of analyze powder samples Lomboy et al [23] mixed it to epoxy and polished it after curing. Interestingly Yang et al [25] prepared reasonably massive flat parts through the Mica-Replication-Method by casting a paste on freshly-cleaved mica, curing and drying before removing from mica due to the stresses produced by the shrinkage of the paste. However the sample preparation has always been a big issue when using cementitious materials for AFM tests.

The problem with most of these techniques is that they may cause cracks and striations due to the mechanical action on the sample, decreasing the quality of the results. Thin films of clinker phases avoid this kind of problems since a thin film, by definition, is extremely flat.

AFM has already contributed to the study of cementitious materials by the investigation of alite alone and in contact with organic admixture [26], to provide information on the early hydration of Portland cement [22], to relate changes on the roughness of the gel surface with hydration rate [27], to observe particle shape and surface texture details of cement, silica fume, fly ashes, and hydrated mixtures [21]. In addition the interaction forces between C-S-H particle surfaces were measured as well as the growth imaging of the C-S-H particles [2, 28].

Observations on the hydration of C_3S and C_2S thin films with AFM are presented here aiming to observe the growth mode of C-S-H on their surfaces when reacting with water or saturated lime solution.

5.3.1 Experimental

For this study, C_3S films of about 280 nm in thickness were produced and kept in an inert N_2 atmosphere and C_2S films of 220 nm were kept in vacuum in order to minimize atmospheric pre-hydration and carbonation prior to the beginning of the hydration experiments.

AFM was settled in contact mode using a silicon nitride tip DNP-S10 type C with k=0.32 N/m for the C_3S sample hydrated in saturated lime solution and type B with k=0.12 N/m for the C_3S and C_2S samples hydrated in water. Samples of the thin films were fixed in a Teflon piece on a metallic holder.

5.3.2 Results and discussion

C_3S hydration in saturated $Ca(OH)_2$ solution

The dry C_3S thin film surface is flat and shows signals of pre hydration by the presence of C-S-H particles (Figure 77a).

After this first image is taken a saturated lime solution was inserted in the system using a peristaltic pump with a continuous flux in order to avoid the carbonation of the solution. The pH was kept at 12.6 during all the process.

As soon as the surface is wet its microstructure starts changing. It is difficult to image the process at the beginning due to the fluctuations on the optic conditions but after a few minutes it is possible to observe the formation of preferential dissolution sites (Figure 77b). Sample was observed always in the same place but shifts are detected.

After 381 minutes no substantial changes are observed but a slightly higher coverage of the surface by the C-S-H grains is noticed (Figure 77c). It presents fewer products than described by Garrault et al [20] for the same time and conditions of exposure. However their sample presents preferential aligned growing that may be due to the striations created during the polishing process. According to Juilland [29] preferential sites of C-S-H precipitation are defects on the substrate and this may be the reason for faster and preferential formation observed here.

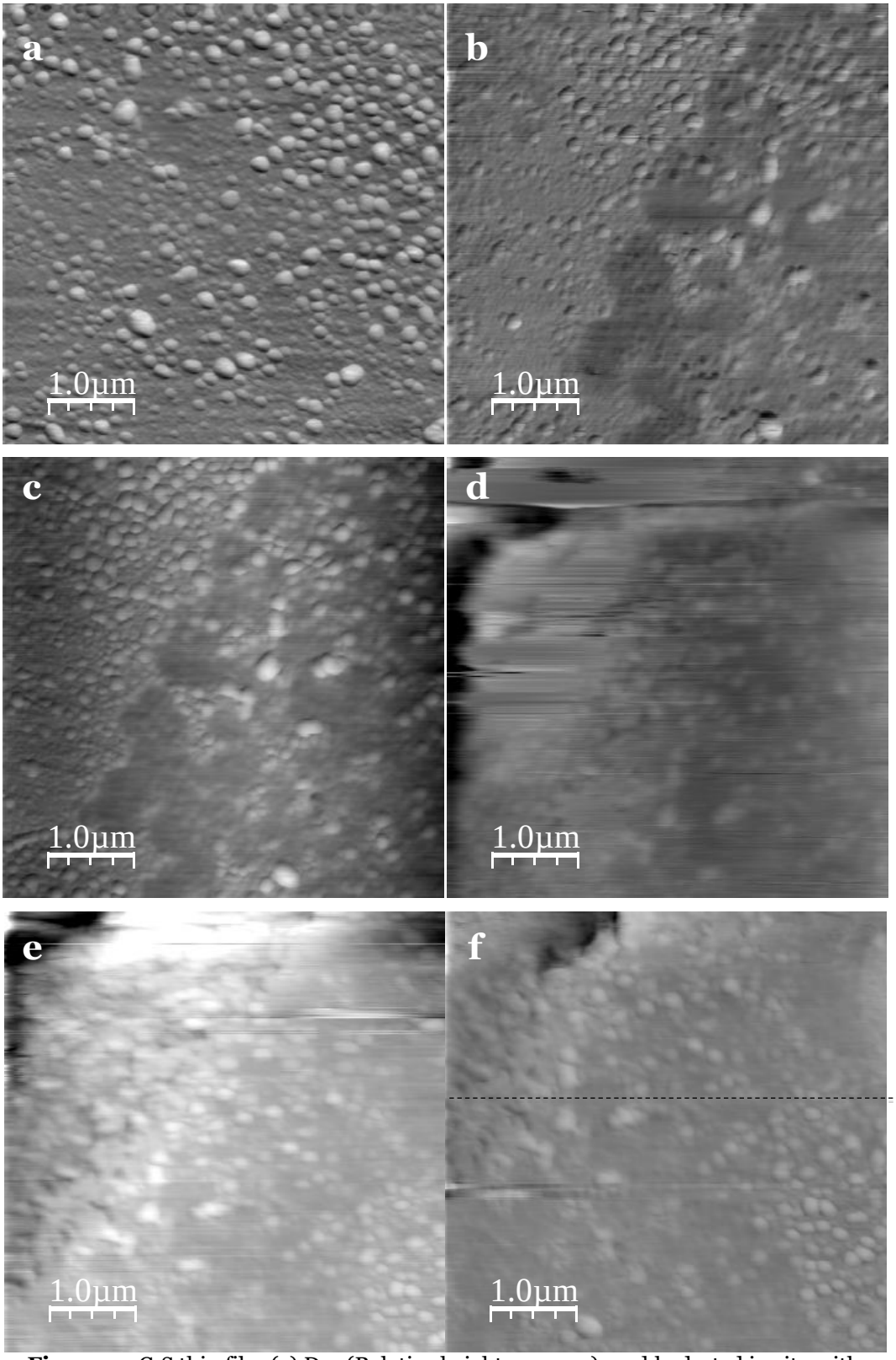

Figure 77 C_3S thin film (a) Dry (Relative height: 100 nm); and hydrated in situ with saturated lime solution: (b) 13 min (Relative height: 200 nm); (c) 381 min (Relative height: 100 nm); (d) 1140 min; (e) 1341 min; (Relative height: 400 nm) (f) 1827 min; (Relative height: 300 nm).

After 30 hours of hydration C-S-H grains cover almost all the surface and total covering may not occur due to the limited amount of material to react considering the thickness of the C_3S film.

Differences on the roughness are useful to quantify differences during the reactions. However in theses images it is not possible to report this regarding to the artifacts observed (darker parts in images d-f) that could mask the results. Quality of each image strongly influences on the results and some of them present interference from the liquid flow and thermal drifts. Besides that, when analyzing profiles from each image (Figure 78) the changes in roughness are clear, presenting initially a partial dissolution and later the formation of small particles every time more evident. Important shifts during the process are noticed.

It is relevant to take carefully the storage of the samples prior to the analysis in order to minimize the pre hydration leaving a higher amount of material to react when exposed to the experimental conditions.

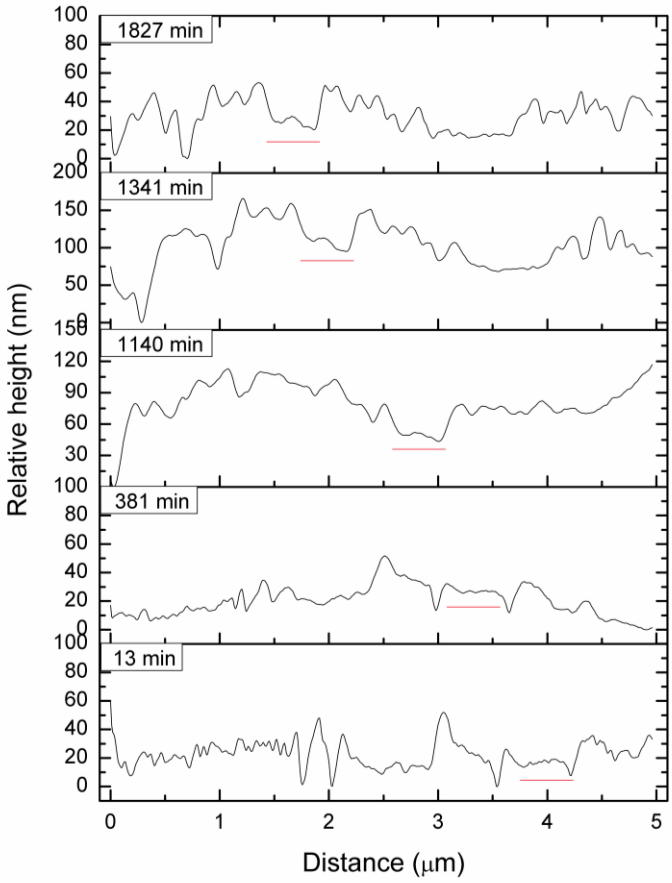

Figure 78 Profile of the black dashed line for the last five images.

C_3S hydration in water

Following the same experimental procedures described for the previous sample, the C_3S hydration in water was observed to happen faster, as expected, but still changes in the morphology and profile can be noticed.

The dry surface presents signs of pre hydration and also the presence of bigger clusters that can be crystals of calcite or portlandite (Figure 79a). They seem to be washed out with the beginning of the water flux through the fluid cell. As in the other sample preferential dissolution sites appear right in the first images taken (28 minutes, Figure 79b). With time of hydration clusters seem to be slightly growing and after 83 minutes the formation of bigger structures that appear to be below the initial structure formed (Figure 79e-h). It can be due to later dissolution of other products such as calcite. The profiles of several images confirm this formation by an increasing on the depth and decreasing on the roughness (Figure 80).

The roughness together with the images analysis shows a clear initial dissolution of the pre-hydration products by its decreasing. The fast formation of the hydration products could not be followed but the dissolution of C-S-H is clearly evidenced by the increasing in the roughness, the images and the profile taken from them.

That happens because the effects of both transport effects and chemical reactions of the liquid flowing and the hydration products, dissolving the portlandite and the C-S-H gel and destroying the cement microstructure. This effect is well known [30] but the kinetics is still being studied [31].

Table 18 Roughness average for C_3S thin films hydrated in water.

Age (minutes)	Roughness average
0	6.20
28	2.42
55	2.89
65	4.89
83	6.65
95	10.11
179	12.76
223	13.30

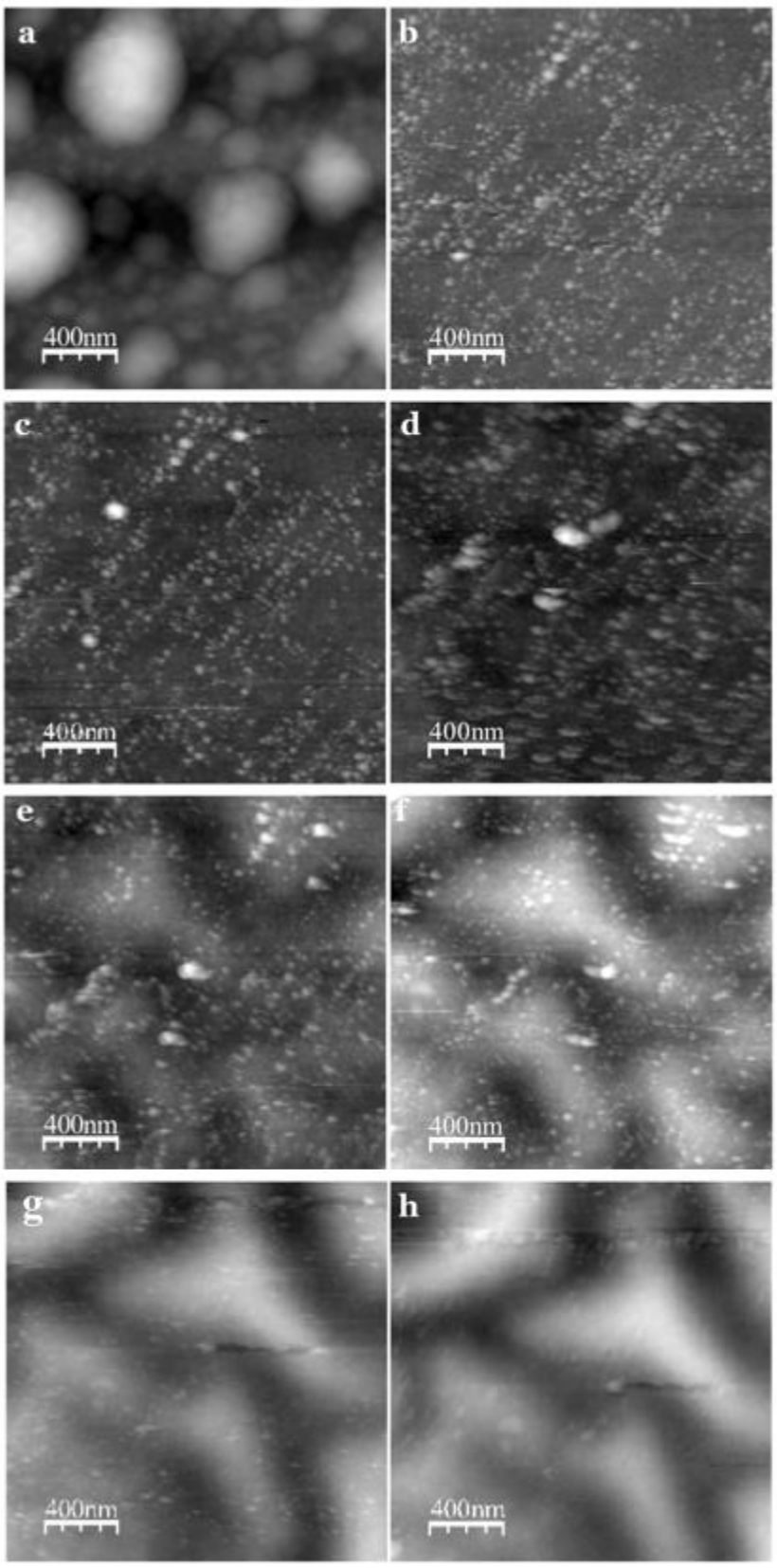

Figure 79 C_3S thin film (a) Dry; and hydrated in situ with water after: (b) 28 min; (c) 55 min; (d) 65min; (e) 83min; (f) 95min (Relative height: 50 nm); (g) 179min; (h) 223min (Relative height: 100 nm).

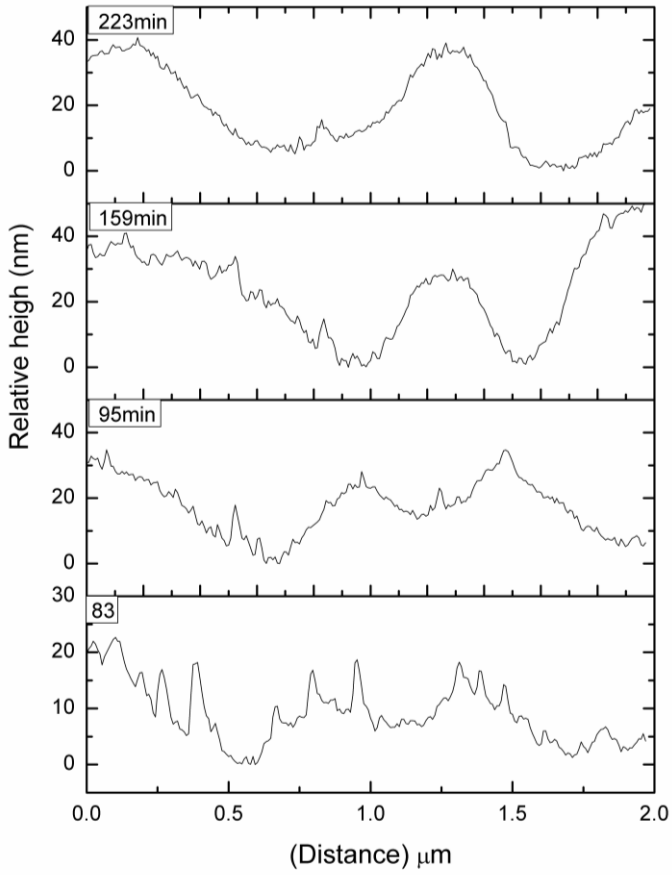

Figure 80 Profile of the last four images.

5.4 Summary and conclusions

Regarding the C_3S hydration

XPS analyses show that samples were partially pre-hydrated and carbonated (during manipulation prior to the experiments); nevertheless, this did not prevent additional hydration.

The XPS monitoring of the position of the Si 2p and Si 2s peaks revealed a shift, as vapor hydration progressed, to higher energies related to silicon polymerization. This is interpreted to evidence the formation of C-S-H. On the other hand, the Ca 2p peak remained essentially centered at the same energy level. Consequently, the distance between the Ca and the Si peaks decreased with time, indicating that the kinetics of early C-S-H formation is not significantly altered when vapor is used instead of liquid water. The bulk molar Ca/Si ratio (once corrected for

carbonate contribution) was found to decrease with hydration time, also indicating a progressive polymerization and increase in chain length of the silicate hydrates formed. Initial Ca/Si values correspond to a jennite-like material, and evolve to a tobermorite-like component after 3 hours of exposure to water.

A scanning electron microscopy study of the evolution of the microstructural changes during the vapor hydration revealed that, as hydration progressed, the exposed surface was covered with hydrates of a few hundreds of nanometers. In order to obtain a cross section view of the sample and image the progress of the hydrated layers, selective milling with an FIB was carried out. After 3 hours of hydration, a rough and porous layer related to the formation of C-S-H was observed.

Likewise the STXM analyses of C_3S thin films when dry indicate the optimum thickness of sample for each edge to be analyzed (calcium and silicon). Based on that the Ca $L_{2,3}$-edge analysis of the C_3S 25 nm film show signs of hydration by the formation of calcium spots around the sample, even so calcium seem to be all around because of the nature of the sample.

Line scan taken over time show variations on the chemical composition inside and outside the particles and also a peak related to the C-S-H formation at 346.8 eV. Differences in intensity during time are also noticed.

Image stacks around particles at different times show differences in the concentration of calcium inside, at the border and outside the particles, where the higher intensities close to the center of the particle are related to higher concentration of calcium.

Image contrast maps show the higher concentration of calcium in some regions but the the calcium NEXAFS spectra in these particles do not confirm this, probably regarding to the amount of this element or the resolution of the equipment.

The Si K-edge analysis shows a shift of the Silicon peak of around 0.8 eV to higher energy in its absorption edge after 151 minutes of hydration compared to the dry sample, related to the silicon polymerization by the formation of C-S-H.

Image stacks taken in different ages and regions relate differences on the intensity of silicon in different regions. Silicon is present in the entire sample but is concentrated mainly in some areas.

On the other hand the individual particle analysis over time during the hydration presents changes while the peak at 1842 eV increases with time related to the formation of C-S-H.

Regarding the C_2S hydration

Thin films of C_2S were prepared by electron beam evaporation and hydrated progressively with water vapor avoiding any contact with air between each stage of hydration and XPS analyses.

The starting material shows a Ca/Si ratio of 2.0, as expected, and a $\delta_{Ca\ 2p\text{-}Si\ 2p}$ of 245.8 eV. However the thin film prior to any treatment presents a Ca/Si ratio lower that the found in the bulk material (1.6). This can be due to pre hydration by the contact with the atmosphere during the sample manipulation or due to preferential deposition of the silicon on the sample's surface after the evaporation. On the other hand, the peak positions are similar to the bulk material, proving that the chemical state is preserved after the evaporation and the $\delta_{Ca\ 2p\text{-}Si\ 2p}$ is exactly the same as in the starting material.

When comparing to the C_3S hydration presented in the previous chapter, the binding energies for silicon on C_2S are higher. This behavior was also observed by Black et al [10].

The exposure to water vapor yields to a drift of the main Silicon peaks to higher energies, indicating the progressive disordering of the silicate structure related to C-S-H formation. At the same time a peak broadening at higher ages is observed with the formation of an additional peak at around 100.2 and 151.2 eV range. The peak at lower energies is related to unaltered β-C_2S while the peak at higher binding energy is assigned to a calcium-depleted C-S-H phase.

The Ca binding energies show a small progressive shift (0.7 eV) when hydration goes on but the $\delta_{Ca2p\text{-}Si2p}$ keep decreasing over time.

On the other hand the silicon polymerization occurs faster in C_3S as the $\delta_{Ca2p\text{-}Si2p}$ distance decreases faster when the same conditions are applied, indicating a faster formation of C-S-H [13].

Observations of the Ca/Si ratio evidence the partial hydration of the upper few nanometers of the sample.

No different peaks related to the contributions from carbonates and silicates are observed even when a deconvolution is performed, differently than the observed in C_3S. This may be due to more careful storage applied to the C_2S sample.

The O 1s spectra are asymmetric and broad and the contribution from non-bridging oxygen decreases with the time of hydration. The δ_{NBO-BO} peak separation increases with the silicon polymerization, describing the C-S-H formation.

Both SEM/FIB and AFM observations shows that initially the sample is very flat and homogeneous and after the exposure to water vapor the formation of clusters are observed, related to the C-S-H, and the increasing on the roughness and porosity of the layer is clearly seen when cutting the sample with the ion gun.

STXM analyses of the C_2S thin films produced were possible only for the Si K-edge because of the excessive thickness. NEXAFS spectra from linescans show that chemical structure gradually changes by an increasing on the 1845 eV peak over time, followed by slight shifts to higher energies.

On the other hand image stack NEXAFS analysis in different times of hydration describe mainly differences in intensity when observing some particles formed, related to the concentration of Si, indicating agglomeration of silicon particles. Later ages show also shifts on the binding energy of the silicon peak on darker particles compared to substrate.

Regarding the liquid cell AFM of early hydration

The atomic force microscope is a useful technique for the observation of the formation of hydration products of C_3S providing high resolution in situ in real time, in real hydration conditions. It has been observed by previous authors and is also useful for analysis of C_3S thin films.

Particles of 60x30x5 nm have been observed in the same manner as previous studies, related to the C-S-H formation.

The dry thin film surfaces are flat and show signals of pre hydration by the presence of C-S-H and CH particles, mainly in the C_3S samples because of the faster reactions and the storage used, with lower protection against the contact with the environment.

The samples' surface starts changing as soon as its contact with the liquid. Even with the difficulties for imaging the sample in the first minutes the formation of

preferential dissolution sites is observed as well as the formation of C-S-H grains. These observations are clearer in the C_2S sample regarding the velocity of the reactions.

Additionally the C_3S sample's surface seems to be dissolved after some time exposed to water flux. This observation is confirmed when verifying the cross section of the images.

5.5 References

[1] M. Regourd, J.H. Thomassin, P. Baillif, J. Touray, Study of the early hydration of Ca_3SiO_5 by X-ray photoelectron spectrometry, Cement and Concrete Research 10 (1980) 223-230.

[2] E.M. Gartner, A proposed mechanism for the growth of C-S-H during the hydration of tricalcium silicate. Cement and Concrete Research 27 (1997) 665-672.

[3] J. Thomas, H. Jennings, J. Chen, Influence of nucleation seeding on the hydration mechanism of tricalcium silicate and cement, Journal of Physical Chemistry 11 (2009) 4327-4334.

[4] J.W. Bullard, A determination of hydration mechanisms for tricalcium silicate using a kinetic cellular automaton model, Journal of the American Ceramic Society 91 (2008) 2088-2097.

[5] S. Bishnoi, K. Scrivener, Studying nucleation and growth kinetics of alite hydration using μic, Cement and Concrete Research 39 (2009) 849-860.

[6] H. Manzano, A. Van Duin, S. Yip, M. Buehler, F. Ulm, R. Pellenq, (2011). The C-S-H gel formation understood by Atomistic Simulation Methods. XIII International Congress on the Chemistry of Cement (2011) 335.

[7] J. W. Bullard, H. M. Jennings, R. A. Livingston, A. Nonat, G. W. Scherer, J. S. Schwitzer, et al. (2010). Mechanisms of cement hydration. Cement and Concrete Research 41 (2011) 1208-1223.

[8] J.J. Thomas, J.J. Biernacki, J.W. Bullard, S. Bishnoi, J.S. Dolado, G.W. Scherer, et al., Modeling and simulation of cement hydration kinetics and microstructure development. Cement and Concrete Research 41 (2011) 1257-1278.

[9] F. Bellmann, D. Damidot, B. Möser, J. Skibsted, Improved evidence for the existence of an intermediate phase during hydration of tricalcium silicate. Cement and Concrete Research 40 (2010) 875-884.

[10] L. Black, A. Stumm, K. Garbev, P. Stemmermann, K.R. Hallam, G.C. Allen, X-Ray photoelectron spectroscopy of the cement clinker phases tricalcium silicate and β-dicalcium silicate, Cement and Concrete Research 33 (2003) 1561-1565.

[11] L. Black, K. Garbev, G. Beuchle, P. Stemmermann, D. Schild, X-ray photoelectron spectroscopic investigation of nanocrystalline calcium silicate hydrates synthesised by reactive milling, Cement and Concrete Research 36 (2006) 1023-1031.

[12] S. Long, C. Liu, Y. Wu, ESCA study on the early C_3S hydration in NaOH solution and pure water, Cement and Concrete Research 28 (1998) 245-249.

[13] L. Black, K. Garbev, P. Stemmermann, K.R. Hallam, G.C. Allen, Characterisation of crystalline C-S-H phases by X-ray photoelectron spectroscopy, Cement and Concrete Research 33 (2003) 899-911.

[14] M.Y.A. Mollah, T.R. Hess, Y.-N. Tsai, D.L. Cocke, An FTIR and XPS investigation of the effects of carbonation on the solidification/stabilization of cement based systems – portland type V with zinc. Cement and Concrete Research 23 (1993) 773-784.

[15] H.F.W.Taylor, Proposed Structure for Calcium Silicate Hydrate Gel J. American Ceramic Society 69 (1986) 464-467.

[16] K.L. Scrivener, A. Nonat. Hydration of cementitious materials, present and future, Cement and Concrete Research 41 (2011) 651-665.

[17] M. Regourd, Microanalytical studies (X-ray photoelectron spectroscopy) of surface hydration reactions of cement compounds. Phil. Trans. R. Soc. Lond. A 310 (1983) 85-92.

[18] L. Black, K. Garbev, P. Stemmermann, K.R. Hallam, X-Ray photoelectron study of oxygen bonding in crystalline C-S-H phases, Phys. Chem. Minerals 31 (2004) 337-346.

[19] S. Gauffinet, E. Finot, E. Lesniewska, A. Nonat. Direct observation of the growth of calcium silicate hydrate on alite and silica surfaces by atomic force microscopy. C. R. Acad. Sci. Paris 327 (1998) 231-236.

[20] S. Garrault, E. Finot, E. Lesniewska, A. Nonat. Study of C-S-H growth on C_3S surface during its early hydration. Materials and Structures 38 (2005) 435-442.

[21] V. G. Papadakis, E. J. Pedersen, H. Lindgreen, An AFM-SEM investigation of the effect of silica fume and fly ash on cement paste microstructure. Journal of Materials Science 34 (1999) 683-690.

[22] L. D. Mitchell, M. Prica, J. D. Birchall Aspects of Porltand cement hydration studied using atomic force microscopy. Journal of Materials Science 31 (1996) 4207-4212.

[23] G. Lomboy, S. Sundararajan, K. Wang, S. Subramaniam. A test method for determining adhesion forces and Hamaker constants of cementitious materials using atomic force microscopy. Cement and Concrete Research 41 (2011) 1157-1166.

[24] P. Mondal, S. P. Shah, L. Marks. A reliable technique to determine the local mechanical properties at the nanoscale of cementitious materials. Cement and Concrete Research 37 (2007) 1440-1444.

[25] T. Yang, B. Keller, E. Magyari, K. Hametner, D. G. Unther. Direct observation of the carbonation process on the surface of calcium hydroxide crystals in hardened cement paste using an Atomic Force Microscope. Journal of Materials Science 38 (2003) 1909 – 1916.

[26] H. Uchikawa, S. Hanehara, T. Shirasaka, D. Sawaki. Effect of admixture on hydration of cement, adsorptive behavior of admixture, and fluidity and setting of fresh cement paste. Cement and Concrete Research 22 (1992) 1115-1129.

[27] G. Papavassiliou, M. Fardis, E. Laganas, A. Leventis, A. Hassanien, F. Milia, A. Papageorgiou, E. Chaniotakis. Role of the surface morphology in cement gel growth dynamics: A combined nuclear magnetic resonance and atomic force microscopy study. Journal of Applied Physics 82 (1997) 449-452.

[28] S. Gaufinet, E. Finot, A. Nonat. Experimental study and simulation of C-S-H nucleation and growth. Materials and Structures 38 (1997) 435-442.

[29] P. Juilland, E. Gallucci, R. Flatt, K. Scrivener, Dissolution theory applied to the induction period in alite hydration, Cement and Concrete Research 40 (2010) 831-844.

[30] Kulik D. A. and Kersten M. Aqueous solubility diagrams for cementitious waste stabilization systems: II, end-member stoichiometries of ideal calcium silicate hydrates solid solutions. Journal of the American Ceramic Society 84 (2001) 3017-3026.

[31] A Trapote-Barreira, J M Soler, J Cama, S Gali, B Lothenbach. C-S-H gel dissolution kinetics. First results. 13th International Congress on the Chemistry of Cement (2011)

6 Conclusions and perspectives

6.1 Regarding the synthesis of thin films

The electron beam evaporation has proven to be a useful and powerful way for synthesizing thin films of calcium silicates. The features observed with grazing angle X-ray diffraction and X-ray photoelectron spectroscopy for samples produced under different experimental conditions correlated very well with the original bulk samples as well as the reproducibility was assured. Chemical and mineralogical compositions are the same for all samples produced.

However with respect to the calcium aluminate phases, the electron beam evaporation conditions used in this work are not suitable for producing thin films. Aluminum present on these phases seems not to evaporate, or does not recondense on the surface, as the other components of the clinker phases, reacting differently when submitted to the extreme conditions on the sample preparation. Grazing angle X-ray diffraction and X-ray photoelectron spectroscopy data show clearly this behavior.

Instead, even if the electron beam evaporation does not work for the phases containing aluminum, other standard techniques for producing ceramic thin films can be applied for this. It is assumed that sputtering may allow synthesizing thin films of these elements as in this technique the sample is not heated but its atoms are ejected by the bombardment of the target material by energetic particles. It happens

due to an ion-atoms momentum exchange when the collisions happen. In this manner all elements contained in the different clinker phases can be sputtered and collected on the substrate without the disadvantage of heating the sample with differential evaporation.

The difficulty on using sputtering techniques is to have suitable targets as it demands not usual preparation and, generally, companies that manufacture those refuse to produce the targets with special specifications such as in this case. In this case additional efforts can be done in order to produce the targets that allow producing thin films of clinker phases with this technique.

On the other hand the usefulness of this kind of sample has been proven by the different ways it has been used in this research to attain information related to dissolution, hydration and carbonation in a way that was never explored before.

6.2 Regarding the suitability and limitation of the characterization techniques

Concerning the analysis techniques, GAXRD was found to be a suitable and very useful tool for the studies of thin films due to the possibility of analyzing very low volume of sample with a standardized technique for mineralogical characterization. However it presents better results when using big detector apertures and large samples, when it is possible to get more intense signal from the sample, with lower noise level and fewer signals from the substrate.

XPS analyze only the upper surface of the sample and for this reason it is appropriate for thin film samples, offering accurate chemical composition and coordination state data. When analyzing all the C_3S and β-C_2S samples the peak positions, peak distances and peak widths are all coincident when compared to the bulk material, proving that they have the same chemical composition.

Finally the use of STXM techniques for the analysis of cementitious materials is very recent and promising. The technique suits the kind of sample used here, as it requires very thin samples in order to be transparent to X-rays at established energies since they have to go through the sample. However many difficulties were found by the lack of an area to be used as reference, or background, where there was no sample mainly for not having an I_o reference for each spectrum taken. The need of taking continuously I_o spectra in other window increase the time of analysis because

of moving to the blank window, refocusing, and moving to the sample again, every time. Additionally having the I_o in the same window increase the reliability of the results.

An additional blank silicon nitride window was adopted in this case to supply the I_o information necessary for processing the data. Nevertheless the most appropriate would be to, in the time of synthesis of the sample, to have a mask covering partially the window in order to have only partial sample deposition. In this way the reference would be available at any time during the analysis, providing more accurate results.

6.3 Regarding the dissolution of C_3S thin films

A special care has to be taken with sample manipulation as changes due to pre-hydration and carbonation can easily be observed concerning the thickness of the sample and the sensibility of the techniques used for analysis.

Experiments with the dissolution of C_3S thin films have successfully shown that sample firstly hydrates, by shifts on the silicon peak to higher energies in the XPS data, while the intensity of the silicon peak related to pure silicon increases due to the dissolution of the layer and the advent of the substrate. The broadening on the calcium peak confirms the evidence of the hydration process.

At the same time the mineralogical composition changed with an increase on the C-S-H broad peak, while an increase on the calcite is also noticed on GAXRD experiments. The AFM observations confirm the changes on the surface, where the formation of aggregated nanoparticles of C-S-H are observed with time.

The dissolution is the main controlling factor of C_3S hydration prior to the acceleration period. The dissolution of C_3S thin films by the initial dissolution of calcite crystals followed by the formation of C-S-H crystals observed here put additional light on the understanding of this process and are representative of the dissolution of the bulk C_3S in the means that same behavior is observed when comparing to previous work in dissolution and hydration of calcium silicates.

6.4 Regarding the hydration of calcium silicate thin films

It has been shown that hydration of calcium silicate thin films follow the same behavior as the bulk material reported in previous works using different techniques applied here: XPS analysis of both C_3S and C_2S hydration evidence the silicon polymerization characterized by shifts on the position of the silicon peaks, as hydration progresses, to higher energies, while the formation of C-S-H and calcium carbonates is confirmed by the maintenance of the Ca 2p peak at the same energy level and its broadening related to differences on the chemical state of the element, so as the decreasing on the distance between the Ca and the Si peaks. Additionally, for both components the bulk molar Ca/Si ratio decreased with hydration time.

In this context for C_3S the initial Ca/Si values are assumed to correspond to a jennite-like material, while it evolves to a tobermorite-like component as hydration goes on.

On the other hand the formation of small particles with 60x30x5 nm during the dissolution and hydration of calcium silicate thin films is related to the C-S-H formation. The same particles were observed in bulk material in previous researches.

NEXAFS analyses of C_3S and C_2S thin films over time show variations on the chemical composition inside and outside the particles in both Si and Ca edges. Early observations lead to conclude that differences on composition are not evident in C_3S due to the fast reaction, while in C_2S thin films shifts in the silicon peak can be observed. The main conclusion taken in these analyses is the fact that particles are formed with different concentration of silicon and calcium depending on the area analyzed. That is, C-S-H particles are formed by agglomeration of the material in some parts of the sample more than forming everywhere in the surface, corroborating to the theory of formation of products in defects sites in the sample.

6.5 Perspectives

It is known that by now in cement and concrete industry many of the products are developed empirically and incrementally, based on observation and experimentation, more than in fundamental research. That is, any new material is applied in concrete and its performance tested for strength and durability. Depending

on the results obtained, besides the costs of production, it starts to be used in industrial scale.

This behavior is due to several factors such as the complexity of the reactions that take place during the cement hydration and the interaction of any material added to the system with the hydrated cement structure. That makes researches in this field difficult to be carried out. On the other hand the concrete industry and the society accept, up to now, that the concrete structures have a relatively short service life with minimum maintenance.

Instead concrete structures are widely used as a way to dispose many industrial waste as well as improving their performance with the use of these materials, such as fly ashes, limestone, slag, silica fume, etc, known as supplementary cementitious materials (SCC). However their chemical interaction with the cement itself is not fully understood. Many researches are developed in this field in order to improve the knowledge and allow the increasing on the use of these materials for concrete. That permits the optimization on the recycling of materials, however it is necessary to take into account the technical performance and availability of these materials regionally.

The use of thin films of clinker phases allows plenty of possibilities for the studies of these materials at nanoscale by incorporating some components on during the synthesis of the films, or synthesizing SCC films (such as nano or microsilica). Changing parameters at this scale allow improving performance and durability of concrete structures. On the other hand many of the elemental characteristics of these materials remain unknown and seek to be explored.

Information in this subject may allow increasing the amount of supplementary cementitious materials that are incorporated in concrete, if their interactions with the clinker phases are fully understood. Additionally, information on the durability can be taken when tests are performed at nanoscale, extrapolating the results for macro scale. In this manner the consumption of clinker can be reduced, creating low-clinker cements, or even new clinkers can be developed, with new cement chemistries. With this the costs and the environmental impact can be reduced.

At the same time important studies on the interactions between the different clinker phases and polymers can be developed using thin films as a tool. Polymers are extensively used in mortar and concrete to improve different properties:

impermeability, plasticity, water demand (porosity), toughness, elastic modulus, bond strength, etc.

This may assist the development and evaluation of new products for the chemical and cement industry and evaluate their structure-properties relationship with the cementitious materials by evaluating the organic-mineral interaction at nanoscale. The effect of different organic polymers on the nanostructure of C-S-H can be evaluated and new materials designed in an appropriated way as to benefit the cement nanostructure.

This make possible to study the effect of several agents on the polymer-modified C-S-H, such as carbonation or chloride interaction.

The measurement of the bond strength between particles can also be performed in these samples in order to characterize the material and the connection with atoms from cement hydrates.

In addition to the possibility of having little amount of material in a flat, thin form opens the possibility of studying the materials with several techniques without the damaging preparation of the samples. This allows the development of researches in non-vacuum conditions that may provide important information on the dissolution-precipitation process. That can contribute to understanding the cause of the slowdown in reaction during the hydration, as well as understanding the growth mechanisms that drives the kinetics on the acceleration period.

Based on this further studies with the techniques used in this work may provide more information on the hydration kinetics mainly changing some parameters when performing the tests of also using alternative techniques.

In this context, the use of quartz crystal microbalances can provide additional light on the mass measurements of reactions of cementitious materials with several reactants by measuring differences in mass during dissolution, hydration, incorporation of materials and so on. In this way important information can be attained on the reactions, kinetics, iteration with other components and durability. Differences in kinetics can also be detected by varying experimental parameters such as humidity, temperature, and chemical composition.

Additionally, fundamental studies in the pre-hydration of cementitious materials can be developed using thin films. This is a relevant factor related to the reactivity of the material, as a layer of hydrated material around the grains prior to the concrete production changes drastically the behavior and performance of the

cement in concrete structures. This can be explored by measuring the depth of pre-hydration for example through XPS experiments by varying the angle of incidence of X-rays and following changes on the binding energy of the constituent elements.

Other important field where thin films could be an interesting tool is to evaluate the degree of aluminate substitution in C-S-H structure. How the aluminum changes the structure and properties of the cement paste is still unknown. This characteristic changes dramatically the properties of the paste as well as the durability of the structure and samples with this nature can be examined in different ways as discussed before. This can be done by incorporating some aluminum during the synthesis of thin films and following chemically the behavior of this component during sample hydration. Another possibility is to submit calcium silicate thin films to hydration in an environment rich of aluminum and observe the incorporation in the hydrates structure.

At the same time many times concrete is used as a barrier for depositing nuclear waste or even in the structure of nuclear plants because of its isolating character. However its properties concerning to the leaching and dissolution process are still not well known and are extremely important for safety reasons. Important studies on the incorporation of metals or trace elements could be performed using clinker thin films in order to evaluate the chemical bonding of these elements with the C-S-H structure. In this way leaching and dissolution can be controlled and risks of human and environment contamination minimized. Some of these materials are found in form of nanoparticles and can be incorporated in the film structure in some way during the evaporation, and later its leaching behavior evaluated with flow-through experiments. The advantage is that, at nanoscale, it is not necessary to perform accelerated experiments as the small scale allows fast and trustful measurements.

Finally, many different techniques are used nowadays for the synthesis of thin films in different industries as discussed in this thesis. The work developed here was based in one of the available techniques, however thin films of clinker phases can be produced in distinctive ways that may be more appropriated to the aluminate phases, such as the sputtering, described previously, or even laser ablation, spin coating, cathodic arc deposition, and so on. Different techniques require different sample characteristics and allow synthesizing different materials films. The matter is to find the suitable technique for each material.

Regarding the morphological changes of the samples during the hydration, FCAFM experiments seem to be very promising when adopting this kind of samples and can be deeply explored in order to measure and quantify in situ the formation of hydration products or even evaluating dissolution or leaching behavior. The ideal conditions in this case would be to perform the tests under nitrogen atmosphere and controlled humidity to have more reliable results, avoiding carbonation and pre-hydration.

Today, the circumstances are changing: the need to reduce greenhouse gas emissions leads to an important interest for more fundamental understanding. Moreover the basic concepts of physics, chemistry and even geochemistry are well established and serve as tools for the cement research, together with the progress in modeling and analytical techniques, which give enough to the cement science to confront the upcoming challenges.

In this context it is clear that this study redirects cement science to new perspectives of understanding the nanostructure of cement products. This leads to basis for developing stronger and more durable cement-based materials.

Annex 1: Papers published

The following papers were published as the result of the studies developed in this thesis and are presented in this section:

V. Rheinheimer, N. Veglio, I. Casanova. Production and characterization of clinker thin films as a new tool for nanoscale studies of hydration mechanisms. XIII International Congress on the Chemistry of Cement (2011) 335.

V. Rheinheimer, I. Casanova. Hydration of C_3S thin films. Cement and Concrete Research 42 (2012) 593–597.

V. Rheinheimer, I. Casanova. Production and characterization of C_3S thin films: a new tool for nanoscale studies of cement. 4th International Symposium on Nanotechnology in Construction (2012).